

HARVARD UNIVERSITY  
Graduate School of Arts and Sciences



DISSERTATION ACCEPTANCE CERTIFICATE

The undersigned, appointed by the  
Department of Physics  
have examined a dissertation entitled

Chirality of light and its interaction with chiral matter

presented by

Yiqiao Tang

candidate for the degree of Doctor of Philosophy and hereby  
certify that it is worthy of acceptance.

Signature Adam E. Cohen

Typed name: Professor Adam Cohen, Chair

Signature David R. Nelson

Typed name: Professor David Nelson

Signature Ronald Walsworth

Typed name: Professor Ronald Walsworth

Date: November 8, 2012

Chirality of light and its interaction with chiral matter

A dissertation presented

by

Yiqiao Tang

to

The department of physics

in partial fulfillment of the requirements  
for the degree of  
Doctor of Philosophy  
in the subject of physics

Harvard University  
Cambridge, Massachusetts

November, 2012

© 2012 - Yiqiao Tang  
All Rights Reserved

## Chirality of light and its interaction with chiral matter

## Abstract

This thesis conducts a systematic study on the chirality of light and its interaction with chiral matter. In the theory section, we introduce a measure of local density of chirality, applying to arbitrary electromagnetic fields. This *optical chirality* suggests the existence of *superchiral* modes, which are more selective than circularly polarized light (CPL) in preferentially exciting single enantiomers in certain regions of space. Experimentally, we demonstrate an 11-fold enhancement over CPL in discriminating chiral fluorophores of single handedness in a precisely sculpted superchiral field. This result agrees to within 15% with theoretical predictions.

Any chiral configuration of point charges is beyond the scope of our theory on optical chirality. To address chiroptical excitations at nanoscale, we develop a model of twisted dipolar oscillators. We design a simple tunable chiral nanostructure and observe localized chiroptical “hot spots” with dramatically enhanced circular differential scattering. Our work on superchiral light and 3D chiral metamaterials establishes optical chirality as a fundamental and tunable property of light, with implications ranging

from plasmonic sensors, absolute asymmetric synthesis to new strategies for fabricating three-dimensional chiral metamaterials.

This thesis is organized as such: Chapter 1 provides a background on previous studies of chiroptical phenomena, and recent efforts in preparing chiral metamaterials. Chapter 2 derives theory on optical chirality, superchiral modes and coupled-dipolar oscillators at nanoscale. Chapter 3 introduces material, apparatus, and pitfalls in chiroptical experiments. Chapter 4 is an overview of the experimental procedure and results on generating and observing superchiral enhancement. Chapter 5 describes the experiments on using spectroscopic polarization microscopy to study chiral 3D chiral metamaterials. Finally in Chapter 6, I discuss quantization of optical chirality and perspectives on future directions.

Here is the list of papers that I published or am preparing relating to the thesis:

1. **Yiqiao Tang**, Adam E. Cohen. “On the Proper Definitions of Spin Density and Spin Current of Photons.” in preparation, 2012.
2. **Yiqiao Tang**, Li Sun, Adam E. Cohen. “Emergence of Chiroptical Response in A Pair of Twisted Dipolar Oscillators.” in preparation, 2012.
3. **Yiqiao Tang**, Adam E. Cohen. “Enhanced Enantioselectivity in Excitation of Chiral Molecules by Superchiral Light.” *Science* 332, 333, 2011.
4. **Yiqiao Tang**, Adam E. Cohen. “Optical Chirality and Its Interaction with Matter.” *Physical Review Letters* 104,163901, 2010 (featured as cover story).

5. **Yiqiao Tang**, T. Cook, Adam E. Cohen. “Limits on Fluorescence Detected Circular Dichroism of Single Helicene Molecules.” *Journal of Physical Chemistry A*, 113, 6213, 2009.
6. N. Yang, **Yiqiao Tang**, Adam E. Cohen. “Spectroscopy in Sculpted Fields.” *Nano Today* 4, 269, 2009.

# Contents

<b>Abstract</b>	<b>iii</b>
<b>Acknowledgement</b>	<b>x</b>
<b>1 Background</b>	<b>1</b>
1.1 Overview of the PhD project	1
1.2 Chirality as a lack of a plane of symmetry	7
1.3 Transformation properties of physical quantities	9
1.3.1 Rotations	11
1.3.2 Spatial reflection	12
1.3.3 Time reversal	12
1.4 Chirality of light: circular dichroism and optical rotatory dispersion	13
1.5 Theory of optical activity: general considerations	18
1.6 Molecular dark state and nano-enhanced optical transition	20
1.7 Natural and artificial structured material	25
1.8 Photonic metamaterial	28
<b>2 Theory on chirality of light</b>	<b>31</b>
2.1 Optical chirality: a measure of EM handedness	31
2.2 Optical chirality interacting with material	33
2.2.1 Response function-based description	34
2.2.2 Time-dependent perturbation calculation in a two-level system	35

2.3	Continuity equation	37
2.4	Superchiral solution to Maxwell's Equations	39
2.5	Pictorial understanding of the superchiral light	42
2.6	Difference between polarization and chirality	43
2.6.1	$ H;V\rangle$ field configuration	45
2.6.2	$ \sigma^+; \sigma^+\rangle$ field configuration	46
2.6.3	$ \sigma^+; \sigma^-\rangle$ field configuration	46
2.7	Nano regime: Coupled-oscillator geometry	47
<b>3</b>	<b>Experimental material and apparatus</b>	<b>52</b>
3.1	Imaging of fluorescence-detected circular dichroism (FDCCD)	52
3.1.1	Polarization optics	53
3.1.1.1	Mechanically driven polarization optics	54
3.1.1.2	Electrically driven polarization optics	57
3.1.1.3	On the choice of polarization optics	58
3.1.2	Imperfection of light source	59
3.1.3	Linear dichroism and linear birefringence of optical element	62
3.2	Chiral fluorophores	64
3.2.1	Diaminocyclohexane-based fluorophores	65
3.2.2	Bridged triarylamine helicenes	67
3.2.3	Binaphthyl perylene derivatives	68
3.3	Pitfalls in chiroptical measurement	71

3.3.1	Single-molecule measurements on assessing molecular chirality	71
3.3.2	Previous measurement and possible pitfalls	73
3.3.3	Methods	74
3.3.4	Experiment results and discussion	77
<b>4</b>	<b>On generating and observing superchiral light</b>	<b>81</b>
4.1	Overview of FDCD measurement	81
4.1.1	Sideways FDCD in liquid state	84
4.1.2	Facial FDCD in solid thin film	86
4.2	Preparing samples for generating superchiral light	87
4.2.1	Generation I: nano-staircases	89
4.2.2	Generation II: micro-printing	91
4.2.3	Generation III: nanometer-scale sandwich geometry.	93
4.3	Results and discussion	95
<b>5</b>	<b>On the chiroptical response of twisted nanowire plasmonic oscillators</b>	<b>103</b>
5.1	Introduction	104
5.2	Experimental procedure	108
5.3	Experimental results and data fitting	112
5.4	Tunable metamaterials	117
5.5	Appendix: Fabrication of gold nanowire arrays	118
<b>6</b>	<b>Conclusion and future perspectives</b>	<b>120</b>
6.1	On quantizing optical chirality and spin angular momentum of photons	120

6.2	Innovation in imaging apparatus	130
6.3	The CLIC concept: beyond chirality	136
	<b>Bibliography</b>	<b>140</b>

# Acknowledgement

Pursuing a PhD degree in physics is a wild ride in the unknown. It's a constant ebb and flow in the emotional, physical, and intellectual endeavors. Fortunately I am not alone. Many people collectively have made the odyssey possible and memorable.

My eternal thankfulness goes to my advisor Professor Adam E. Cohen, who has been showing me the qualities of a scientist. I'm indebted to Adam for taking me into the research lab, and for the countless days and nights of interactions ever since. His ingenious and strenuous attempts to tackle the most difficult problems, exacting attitude in conducting and presenting the work, capability of managing serendipity and the kindness in treating peers and students have profoundly shaped my perspectives on scientific research. For many years to come the impacts and inspirations he has rendered to me will last.

Cohen Lab is a stimulating and fun place to work in. I have enjoyed collaborating and discussing with many talent, among whom particularly Alex Fields, Jennifer Hou, Nan Yang, Min Ju Shon, Prashant Jain, Hohjai Lee, Sabrina Leslie, Dougal Maclaurin and Joel Kralj. I thank Jonathan Fan in the lab of Professor Federico Capasso for co-initiating the chiral nano-junction project, and Nan Niu in the lab of Professor Evelyn Hu for helping with nanofabrication.

I thank staff in the Center for Nanoscale System at Harvard University for their relentless efforts in maintaining the facilities and offering guidance and help, even late in

the night or during vacations. There I am particularly grateful to Jiangdong Deng, Yuan Lu, Ling Xie, Ed Macomber and David Lange. I thank Professor Bertrand Halperin for his thoughtful comments on our theory on optical chirality. I thank Timothy Cook and Professor Heinz Langhals for kindly preparing materials for my experiments, so that I may stay on the physics side and not worry about jeopardizing my life in the fume hood. I thank Professor Laurence D. Barron and Bart Kahr for their generous sharing of knowledge. And I thank Lu Men and Gonglue Jiang for making the fine illustrations for my research.

I worked as a summer intern at Schlumberger-Doll Research, and as a research associate at Harvard Kennedy School of Government. I thank people in the two working places that helped me acquire knowledge in the oil & gas industry from the angle of technology and policy, respectively, where I see my future career lying. They are Yi-Qiao Song, Martin Hürlimann, Martin Poitzsch, Jeffery Paulsen, Soumyajit Mandal, Marcus Donaldson, Yesu Feng, Yi Zeng, Qing Gu, Meagan Mauter, and Vanessa Palmer.

My thankfulness extends to many dear friends I encountered during the course of my PhD study, who constitute a sizeable proportion of my life in graduate school. Meng Su, Qimin Quan, Peng Zou, Yan Zhou, Xiaochen Fu, Kecheng Li, Billy Au, John Wu, Xiaole Wu, Yuqi Qin, Kui Han, Zhiping Chen and Maoxin Liu are the people I always turned to for comfort and amusement. I thank Olivia Yin for propelling my self-awareness. I thank Nikita Bernstein for introducing me into the entrepreneurial community, with

whom I started a talent management company that is running smoothly. I thank Cecilia Chen and Joshua Whitson for leading the volunteer teaching program to Dandelion School for migrant worker's children, exhibiting the compassion, caring and merriness for the well-being of others. I thank Jennifer Wang for her encouragement and for lifting me up from time to time.

I thank my thesis committee for many constructive comments on both my research and the thesis. They are Adam E. Cohen, Ronald Walsworth, and David Nelson.

My parents and grandparents' moral supports have been of absolute essentialness. They are the easiest to neglect and for the exact reason, I could not express more gratitude to. They hold up their opinions and expectations, and allow me to stumble and to pursue my beloved 12,257 miles (according to Google Maps) away from home. Anyone who has taken a venture like mine will recognize what it has cost them.

The thesis is dedicated to Werner Kuhn (1899 - 1963). I came across his pioneering work on the study of optical activity in theory and experiment, while had a hard time tracking down the full list of his contributions. To my amazement, I finally was able to relate his name to many well-known discoveries, such as Kuhn length, Mössbauer effect, and countercurrent multiplication that are in seemingly unrelated research fields. The creativity, diversity and thoroughness in his endeavors shall be remembered.

For Werner Kuhn (1899–1963)

Life can only be understood backwards; but it must be lived forwards.

- Søren Aabye Kierkegaard

# List of tables

1.1 Transformation properties of various physical quantities.	11
1.2 Nano-enhanced optical transitions.	23
2.1 Symmetry table of basic EM descriptors.	33
2.2 Chirality in optical standing waves.	45
3.1 Pros and cons of selected polarization optics.	54
3.2 Elimination of laser pointing instability by using a single mode fiber.	61
5.1 Fitting parameters in the chiroptical response of “twisted H”.	116
6.1 List of modulation frequencies that are useful in various systems.	132

# List of figures

1.1 The field configuration in circularly polarized light and superchiral light.	3
1.2 A schematic of experimental setup for generating superchiral light.	4
1.3 Molecular excitation in a spatially sculpted EM field.	6
1.4 The definition of chirality.	7
1.5 Photograph and molecular structure of tartaric acid.	9
1.6 Working principles of circular dichroism and optical rotation dispersion.	15
1.7 Simple model to illustrate the origin of chiroptical excitation.	19
1.8 Optical properties of structural materials in nature.	26
1.9 3D photonic metamaterials.	30
2.1 Enhanced chiral asymmetry in the superchiral light.	40
2.2 The twisted H configuration.	49
3.1 Working principles of linear polarizers and wave plates.	56
3.2 Working principle of liquid crystal variable retarder.	58
3.3 Defects in wave plates.	59
3.4 Calculated spurious $g$ -value incurred by pointing instability.	60
3.5 Experimental apparatus for calibrating polarization properties of optics.	63
3.6 Exciton-spectra of CD spectra.	65
3.7 Diaminocyclohexane-based chiral fluorophores.	66
3.8 Key steps in synthesizing bridged triarylamine helicenes.	68
3.9 CD spectra of <i>p</i> - and <i>m</i> -triarylamine helicenes.	69
3.10 Binaphthyl perylene derivatives and achiral compound.	70
3.11 Schematic of optical setup for single-molecular chiroptical measurement.	75
3.12 Fluorescence of single helicene molecules in CPL.	80
4.1 Experimental setup for PEM-based FDCD measurement.	83
4.2 Experimental setup for sidewise FDCD measurement.	85
4.3 Results of sideways FDCD measurement on binaphthyl perylene dimers.	87
4.4 Experimental setup for facial FDCD measurement.	88
4.5 Results of facial FDCD on chiral molecules in thin polymer films.	89
4.6 Staircase nanostructures for probing superchiral light.	90
4.7 Microfabrication of alternating stripes of chiral and achiral fluorophores.	92
4.8 Scheme for detecting superchirality in the micro-patterned sample.	93
4.9 Procedure for preparing the nanometer-scale sandwich geometry.	94
4.10 Measurement apparatus for observing superchiral enhancement.	96
4.11 Observation of enhanced optical dissymmetry in superchiral light.	101
5.1 Planar and three-dimensional chiral metamaterials.	104
5.2 Illustration of twisted dipole configuration.	106
5.3 chiroptical hot spots of the nano-junctions at 630 nm excitation.	107
5.4 Schematic of CLIC apparatus.	109

5.5 Dissymmetry factor for nanowire arrays under CPLs of different ellipticity.	110
5.6 Schematic and data for linear dichroism of single nanowires.	111
5.7 Schematic and data for linear birefringence of single nanowires.	112
5.8 Linear dichroism of a single nanowire as a function of excitation wavelength.	114
5.9 Data and theoretical fittings on the chiroptical hot spots.	115
5.10 Nanofabrication of gold nanowire arrays.	119
6.1 Electric and magnetic field in the “polarization gradient” configuration.	120
6.2 Structure of the scientific lock-in imaging module.	131
6.3 Lock-in imaging on a thin plastic sheet.	134
6.4 Schematic of surface plasmon resonance in the application of biosensing.	138

# Chapter 1

## Background

One long-standing goal of spectroscopy is to control the spatial and temporal dynamics of electromagnetic (EM) fields in a precise manner for certain functional purposes. Two crucial pillars complimentary to achieve the goal are: a set of theoretical underpinnings that illustrates a particular type of interaction between light and matter, and predicts certain phenomena and measurables; and the experimental methods for preparing desired structures and on which to fulfill the predicted functions. In this thesis, we examine the chirality of light and its interaction with chiral matter from the two angles.

This chapter is a summary of background knowledge that I learnt in pursuing the study. An overview of the thesis topic is followed by an introduction of chirality, transformation properties of physical quantities, and chirality of light in particular. The rest of the chapter is dedicated to describing natural and artificial structured materials that exhibit unusual features upon interacting with light.

### 1.1 Overview of the PhD project

Light may be chiral with circularly polarized light (CPL) as a paradigmatic example,<sup>1</sup> yet quantification of the chirality of light has not been satisfyingly addressed: since the time of James Clerk Maxwell, well-known attributes in EM theory include energy, momentum and angular momentum; yet no such quantity existed for EM handedness.<sup>2</sup>

In practice, CPL has been routinely employed to characterize the structures of chiral species.<sup>3</sup> This “circular dichroism spectroscopy” (CD) assesses differential molecular absorption of left- and right-CPL. Due to a mismatch between molecular size and the wavelength of excitation light, CD signal is notoriously small.<sup>1</sup>

Accordingly, the four questions we asked that motivate my PhD research are:

- I. How does one quantify, if possible, the chirality of an electromagnetic field?
- II. Do there exist EM modes that distinguish chiral species of opposite handedness with greater efficacy than CPL?
- III. Experimentally, is it feasible to tune chiroptical interaction by spatially engineering EM fields?
- IV. What are the limits of the theoretical framework? If necessary, we shall iterate the process by asking the questions I – III.

To answer the first question, we sought a quantity that provides the appropriate mathematical picture and symmetry properties. The *optical chirality* appears as a promising candidate:<sup>4</sup>

$$C \equiv \frac{1}{2} \left\{ \epsilon_0 \mathbf{E} \cdot (\nabla \times \mathbf{E}) + \frac{1}{\mu_0} \mathbf{B} \cdot (\nabla \times \mathbf{B}) \right\}, \quad (1.1)$$

where  $\epsilon_0$  and  $\mu_0$  are the permittivity and permeability of free space, respectively, and  $\mathbf{E}$  and  $\mathbf{B}$  are the time-dependent electric and magnetic fields. This chirality density  $C$  transforms as a time-even pseudo-scalar.<sup>2</sup>

Based on the *optical chirality*, we proposed a solution to Maxwell’s Equations that are

more effective at distinguishing chiral enantiomers than CPL. We deduced this superchiral light solution as such: First, we drew a configuration of electric fields that appears highly chiral (Figure 1.1, bottom).

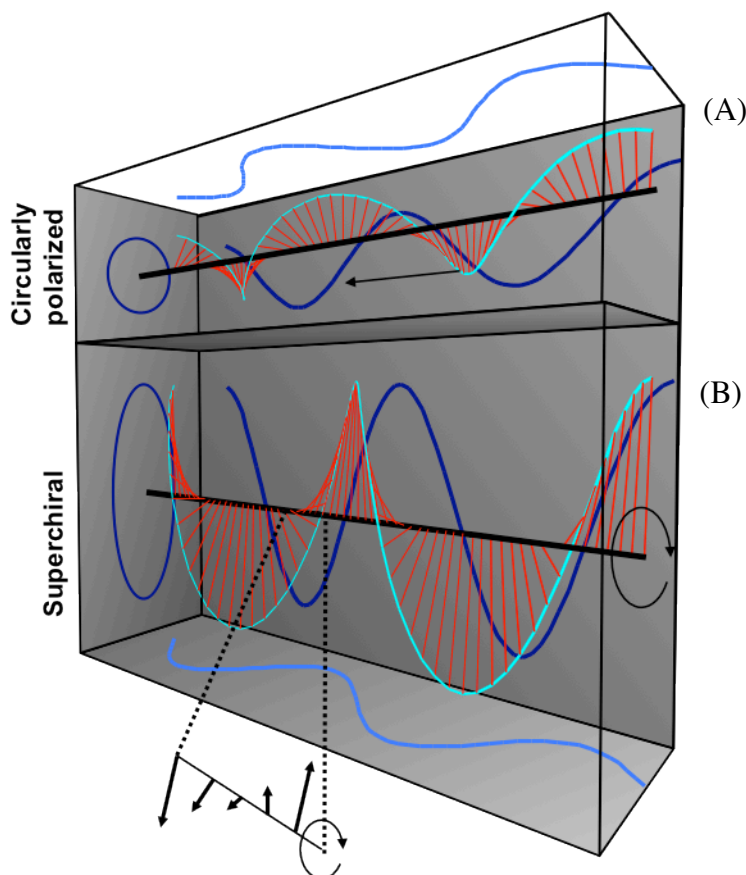


Figure 1.1: (A) Electric field in left-circularly polarized light. The field has uniform optical chirality and energy density throughout space. Also plotted are projections of the field onto the  $xy$ ,  $xz$  and  $yz$  planes, at a single point in time. The arrow indicates direction of propagation of the field. (B) Electric field in superchiral light, calculated from the analytical expression at a single point in time. The superchiral field rotates about its axis, but does not propagate. At any instant, the projection of the field along the propagation axis is an ellipse, but over time the field at each point traces out a circle. Near the superchiral nodes the ratio of optical chirality to electric energy density is larger than in circularly polarized light. In this plot, the ratio of the left- and right field amplitudes is 2:1. In the experiment, the ratio was 1.17:1. Bottom: field configuration near a superchiral node.

The field vectors rotate through nearly  $180^\circ$  in a distance much shorter than half the free-space wavelength. Then we sought solutions to Maxwell's equations that generated these fields in at least one point in space. An optical standing wave was a promising candidate because near the nodes energy density is small, yet the field appears to have a strong twist. The existence of such a solution addresses the question II.<sup>5</sup>

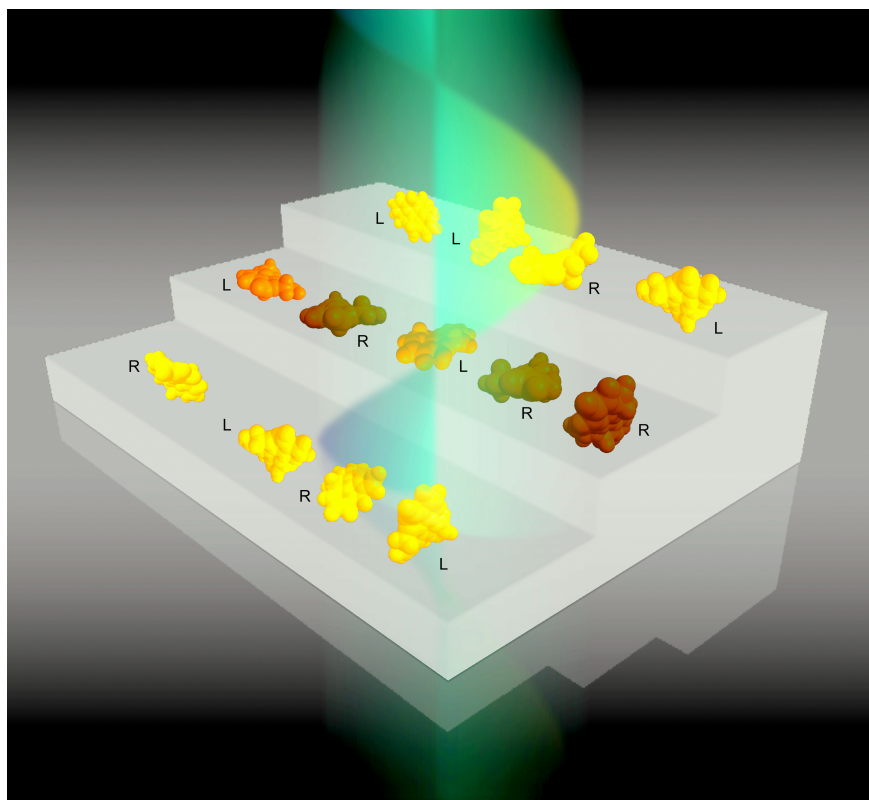


Figure 1.2 Confined to thin films at different heights above a reflective surface, molecules are predicted to show enhanced chiral asymmetry when illuminated with circularly polarized light.

The *superchiral standing wave* may be generated by bouncing a CPL beam off a mirror with reflectivity  $R < 1$ . Figure 1.2 shows one of the proposed experimental schematics. The daunting challenges in the measurement include: confining molecules at the nodes of

superchiral light where enhancement in enantiomeric selectivity may take place; preparing the fluorescent chiral molecules with an appreciable electronic chiral band at a desired excitation wavelength; and ensuring a drift of apparatus within  $\lambda/10^4 \sim 0.5 \text{ \AA}$  over the course of the experiment; and compensating the pointing instability and power fluctuation of the light source. Large part of the thesis is dedicated to describing the experimental challenges and approaches we take to circumvent the problems in observing the predicted enhancement.

The theory on the optical chirality is only applicable to linear, isotropic chiral media where the dominant chiral signature is determined by the 2<sup>nd</sup> order multipole expansion of the molecular Hamiltonian. A further constraint is that the size of the chiral molecules under study needs to be much smaller than the excitation wavelength. Systems that beyond the scope of the theory include: three-dimensional chiral nanostructures;<sup>6</sup> anisotropic chiral media where the quadrupole contribution becomes significant;<sup>7</sup> liquid crystal molecules with molecular size up to a few hundred nanometers;<sup>8</sup> nonlinear chiral effects such as second-harmonic generation,<sup>9</sup> and coherent control schemes to boost originally weak chiral transitions.<sup>10</sup>

Given our field of expertise and the active research on the metallic stereometamaterials,<sup>6, 11</sup> we decided to examine chiral properties of the nanostructures. We employed the CLIC (Convex lens induced confinement)<sup>12, 13</sup> geometry to devise a tunable three-dimensional plasmonic nanostructure, and mapped the spatial distribution of chiroptical excitation using a wide-field polarization microscope. Nontrivial spatial and

spectral features are revealed. The features relate to the polarization properties of individual achiral component and their spatial arrangements in a coupled-oscillator model.<sup>14</sup>

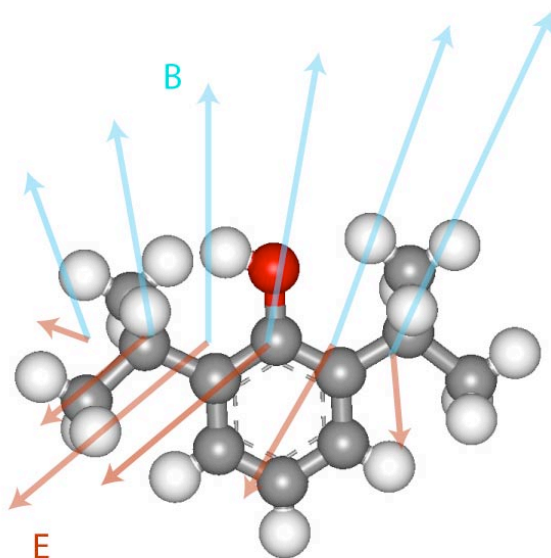


Figure 1.3: Molecular excitation in a spatially sculpted EM field

As noted in the beginning, one grand goal of spectroscopy is to control the electromagnetic field throughout a complex molecule, atom-by-atom and femtosecond-by-femtosecond.<sup>15, 16</sup> The goal of ultrafast spectroscopy is to change the field on timescales comparable to the internal dynamics of a molecule, and thereby to learn about these dynamics.<sup>17</sup> While there is much work on pushing spectroscopy to femtoseconds and below, there is currently less emphasis on creating fields that vary significantly over distances comparable to the size of a molecule. Spatially engineered fields allow one to probe the physical structure of a molecule and its excitations in a manner that is inaccessible to far-field techniques working on any timescale, even ultrafast.

In the thesis I illustrate the spectroscopic importance of sculpted EM fields, with optical phenomena that are beyond the point-dipole approximation (PDA) as an example. Eventually, spatial and temporal sculpting of electromagnetic fields may be combined to achieve the ultimate goal of full spatiotemporal control. (Figure 1.3)

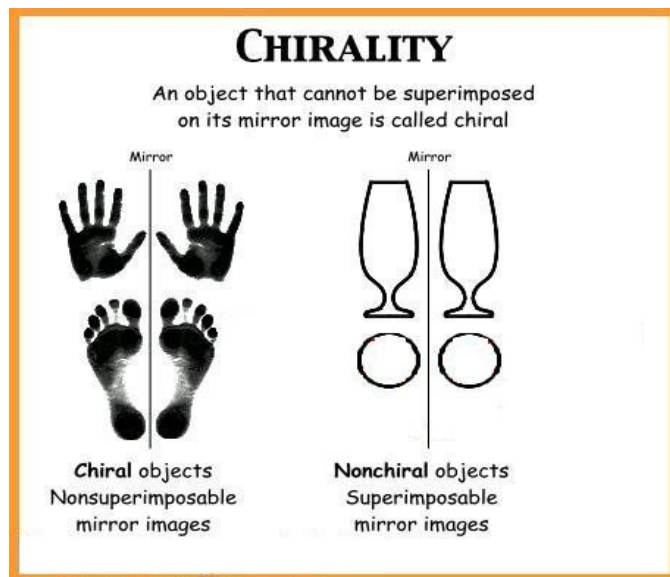


Figure 1.4 The definition of chirality

## 1.2 Chirality as a lack of a plane of symmetry

Chiral objects are bodies, such as a human hand, whose mirror image may not be superimposed on the original (Figure 1.4). In 1848, Louis Pasteur<sup>18</sup> discovered molecular chirality when investigating rotation of the plane of linearly polarized light traveling through a solution of natural sodium ammonium tartrate. In the ingenious experiment, Pasteur crystalized a solution of sodium ammonium tartrate, later known as racemic mixture, and mechanically sorted the two chiral crystals of opposite handedness under magnification (Figure 1.5). He further inferred, correctly, that the spontaneous

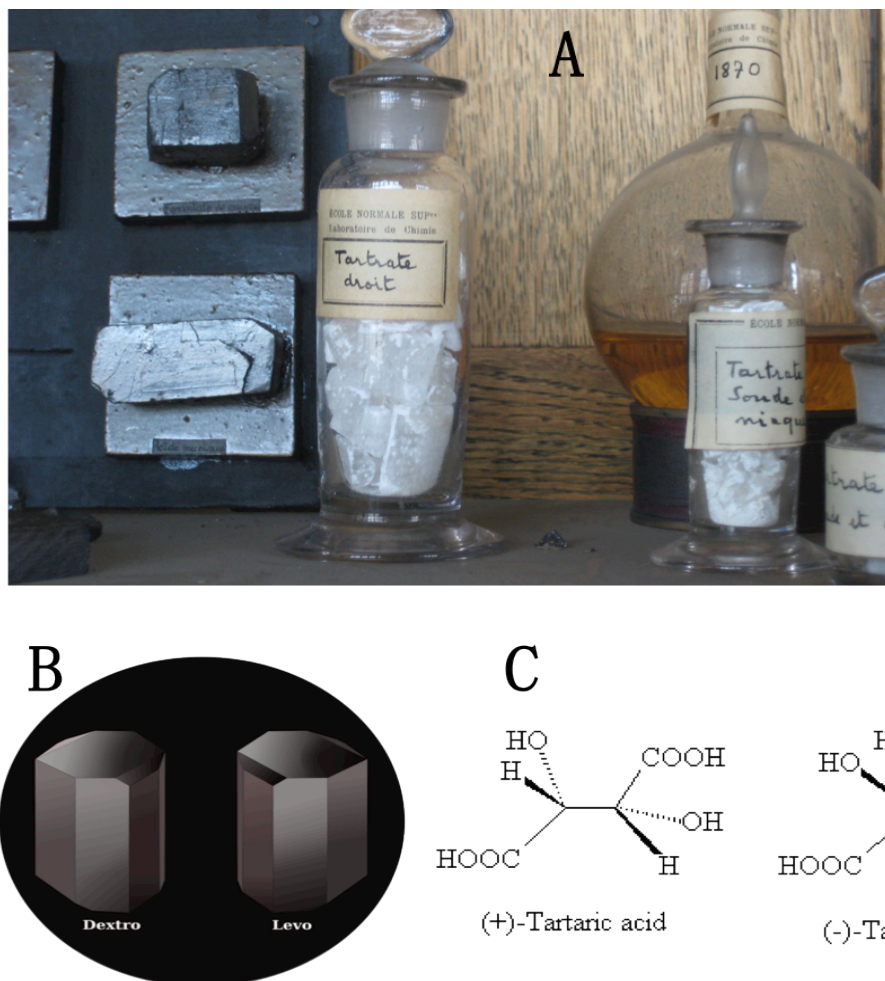
resolution was due to chirality at the molecular level. i.e. the molecules of sodium ammonium tartrate consist of two species of opposite handedness.

As the case for Louis Pasteur, a challenge in ventures involving the study of molecular chirality remains the identification and separation of enantiomers (i.e. molecules with opposite chirality). Opposite enantiomers are indistinguishable in most regards: all scalar physical properties (e.g. density, molecular weight, enthalpy of formation, electronic and vibrational frequencies) are identical. Reactivity with achiral compounds is also the same for both enantiomers. Only in their interactions with other chiral objects do enantiomers become distinguishable.

The asymmetric interaction of chiral objects is essential in comprehending most problems relating to chirality and of particular importance in distinguishing chiral compounds. One simple example to help understand the dissymmetry is the “hand-and-glove proposition”: To select the glove of certain handedness in a pair, the most efficient approach is to attempt to wear both by the corresponding hand. While one glove may not cooperate, the other should fit onto the hand smoothly and is the one of choice. While probably the crudest experiment in separating chiral enantiomers (i.e. the glove pair), the hand-glove demo finely illustrates the principal of many physical and/or chemical processes in chiral resolution.

Chirality is a lack of a plane of symmetry. It is a generic concept and may find applications across a variety of subjects. As is fundamental to life, most biologically active molecules, such as amino acids, sugar, DNA and peptide, occur in only one chirality

in nature: amino acids are largely L, sugars are D, and DNA molecules are mostly right-handed.<sup>19</sup> Drugs interact with biomolecules in complex physiological pathways, and so chirality is also fundamental to medicine, as the desired product and its mirror image



[http://en.wikipedia.org/wiki/Optical\\_rotation](http://en.wikipedia.org/wiki/Optical_rotation)

Figure 1.5 (A) The original crystals of sodium ammonium tartrate that Louis Pasteur separated, photo by Adam Cohen in the chemistry library at École Normale Supérieure in Paris; (B) Tartaric acid crystal of opposite handedness, as if seen under microscope; (C) The molecular structures of the tartaric acid enantiomeric pair

may have drastically different pharmacological properties.<sup>20</sup> In fact, more than 50% of drugs consist of compounds of single enantiomers.

A longstanding dream of synthetic chemists is to create chirality *de novo*.<sup>21, 22</sup> In every chiral synthesis performed today, chirality is imparted to the product either from chiral starting materials, a chiral catalyst, or a chiral separation. These chiral building blocks all ultimately trace their origin to biogenic sources. Chirality begets chirality, but nobody knows whether the homochirality of life on Earth arose randomly or as a consequence of some subtle physical influence.<sup>23-25</sup> A variety of physical influences have been proposed, ranging from magnetochiral anisotropy<sup>25</sup> to parity-violating weak interactions,<sup>26, 27</sup> but all of these effects are very small. Thus there are both practical and fundamental reasons to be curious about chirality and how to create it.<sup>28-30</sup>

### **1.3 Transformation properties of physical quantities**

Before continuing the discussion on the chirality of light, in the section we will introduce transformation properties of physical quantities. Transformation properties tie closely to symmetry. By definition, a symmetry of a physical system is a physical or mathematical feature of the system (observed or intrinsic) that is preserved under certain changes. Compatible transformation properties of related physical quantities under certain types of coordinate transformation oftentimes reveal intrinsic properties of the system and thereby place limitations on the form of the relations. Therefore, quantities employed to describe chirality of a physical system are to conform to certain transformation requirements.

We will quickly summarize the idea of space and time coordinate transformations. A more in-depth discussion on the topic may be found in books by Goldstein<sup>31</sup> and JD

Jackson.<sup>2</sup>

### 1.3.1 Rotations

A Rotation is a linear transformation of the coordinates in three dimensions. The invariant in such a transformation is the sum of the squares of the coordinates.

Let  $\{x_\alpha\}$  and  $\{x'_\alpha\}$  represent coordinates before and after the rotation transformation, respectively. The two sets of coordinates are related by:

$$x'_\alpha = \sum_\beta a_{\alpha\beta} x_\beta \quad (1.2)$$

Physical quantity		Rotation	Spatial reflection	Time reversal
Coordinate	$\mathbf{r}$	1	odd	even
velocity	$\mathbf{v}$	1	odd	odd
momentum	$\mathbf{p}$	1	odd	odd
Kinetic energy	$p^2/2m$	0	even	even
Charge density	$\rho$	0	even	even
Electric field	$\mathbf{E}$	1	odd	even
Magnetic field	$\mathbf{H}$	1	even	odd
Energy density	$U = \frac{1}{2}(\epsilon_0 E^2 + \frac{B^2}{\mu_0})$	0	even	even
Poynting vector	$\mathbf{S} = \mathbf{E} \times \mathbf{H}$	1	odd	odd
Angular momentum	$\mathbf{J} = \mathbf{r} \times (\mathbf{E} \times \mathbf{H})$	1	even	odd

Table 1.1 Transformation properties of selected physical quantities

And the inverse transformation has the coefficient  $(a^{-1})_{\alpha\beta} = a_{\beta\alpha}$ . Physical quantities are ranked as rotational tensors depending on the transformation properties under rotations. Quantities such as electric field  $\mathbf{E}$ , magnetic field  $\mathbf{B}$ , coordinates  $\mathbf{x}$  that transform per the law of equation (1.2) are tensors of rank one, or *vectors*. Scalar products of vectors such as  $\mathbf{E} \cdot \mathbf{B}$  are invariant under rotation and so are tensors of rank zero, or *scalars*. Higher-rank tensors follow the transformation law of equation (1.2) with more than one transformation coefficient.

### 1.3.2. Spatial reflection

Spatial reflection is a spatial transformation involving a reflection in a plane, where normal components of the coordinate vectors change sign and parallel components to the plane remain unchanged. Mathematically, for reflection in the x-y plane, spatial reflection corresponds to a transformation of  $\mathbf{r} = (x_i, y_i, z_i)$  to  $\mathbf{r} = (x_i, y_i, -z_i)$ .

Physical quantities are classified into two groups by the transformation properties under spatial reflection: *Polar vectors*, such as electric field  $\mathbf{E}$ , change sign under spatial reflection, while *axial vectors*, such as magnetic induction  $\mathbf{B}$ , are invariant under the transformation.

Similar distinctions are made for scalars. We distinguish scalars and pseudoscalars, depending on whether the quantities do not or do change sign under spatial reflection.

### 1.3.3. Time reversal

Transformation of physical quantities under time reversal is not to be confused with transformation of basic laws of physics, which are mostly insensitive to the direction of

time. Physical quantities transform under time reversal  $t \rightarrow t' = -t$  in a consistent fashion so that the form of the equation is the same as before. For example, Newton's equation of motion is:

$$\frac{d\mathbf{p}}{dt} = -\nabla U(\mathbf{x}) \quad (1.3)$$

where  $\mathbf{p}$  is the momentum,  $\mathbf{x}$  is the position, and  $U(\mathbf{x})$  is the potential energy. From the relation, we conclude that  $\mathbf{p}$  is odd while  $\mathbf{x}$  is even under time reversal.

We summarize the transformation properties of various physical quantities in Table 1.1.<sup>2</sup> Chiral descriptors to any system are required to be even in time reversal (a movie of a right-handed screw shows a right-handed screw whether the movie is played forward or backward) and odd in spatial reflection (a mirror-image of a right-handed screw is a left-handed screw).

#### **1.4 Chirality of light: circular dichroism and optical rotatory dispersion**

Circularly polarized light (CPL) is a chiral object, so its interactions with matter are sensitive to molecular chirality. Two types of optical spectroscopy are frequently used in probing molecular chirality, as shown in Figure 1.6. The first is circular dichroism (CD),<sup>1</sup> where the extinction coefficients of molecules are slightly different for propagating CPL through solutions of opposite enantiomers. The second is optical rotation dispersion (ORD),<sup>1</sup> where the refractive index of chiral media differs between left- and right-CPL. Linear polarized light may be treated as a coherent superposition of left- and right-CPL of equal amplitude and fixed phase. Let refractive index of left- and right-CPL be  $n_L$  and  $n_R$  in a chiral medium. A linear polarized beam that travels through the medium may

experience a rotation of the plane of polarization by an angle  $2\pi l(n_L - n_R)/\lambda$ , where  $l$  is the propagation length and  $\lambda$  is the wavelength. In practice, structural elements are more clearly distinguished in CD since their recorded bands do not overlap extensively at particular wavelengths as they do in ORD. In principle, CD and ORD may be interconverted through integral transformations (Kramers–Kronig relations).

In CD, The strength of chiral asymmetry is measured by the dissymmetry factor:

$$g \equiv \frac{2(A^+ - A^-)}{A^+ + A^-} \quad (1.4)$$

where  $A^{+/-}$  are the rates of excitation of a single enantiomer in right- and left-CPL respectively (or equivalently, opposite enantiomers in light of a single handedness). Over the nearly two centuries since the discovery of chiroptical phenomena, much effort has gone into predicting CD spectra from molecular models, and into inferring molecular structure from CD spectra.

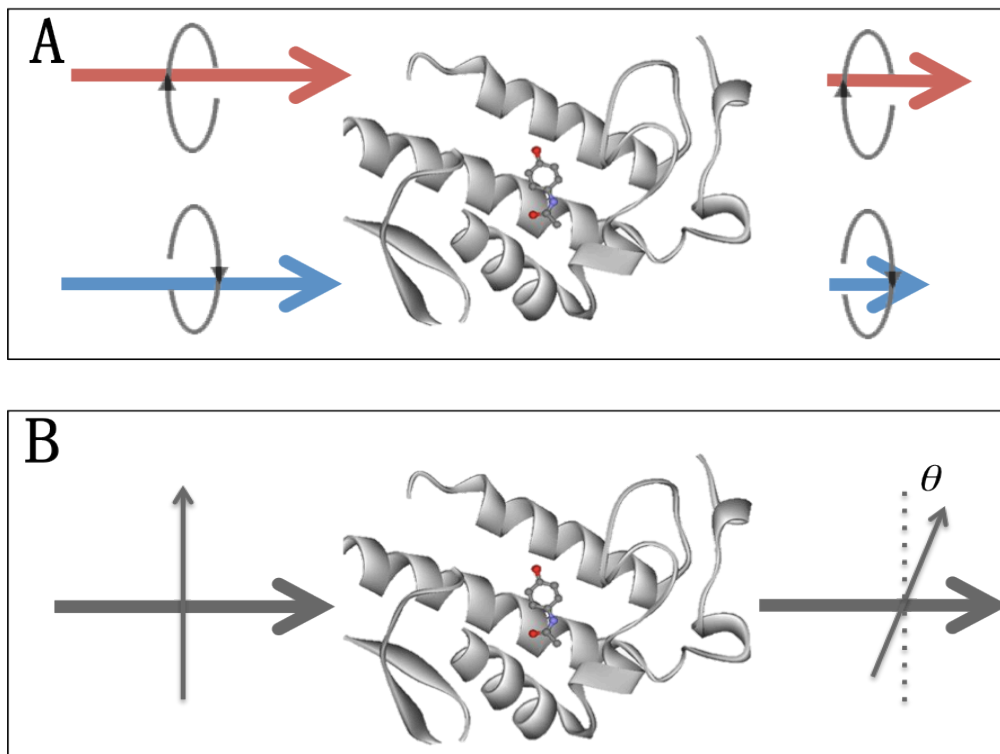


Figure 1.6 Working principles of (A) Circular dichroism that intensity of the left- and right - CPL attenuates differently when travelling through a chiral medium; (B) Optical rotation dispersion that the plane of linear polarization rotates when light travels through a chiral medium

CD spectroscopy is usually used to study biomolecules in liquid state, which is complimentary to other methods on solid state (such as NMR, mass spectrometry). The far - UV (Ultraviolet) CD spectrum may reveal important characteristics of protein's secondary structure,<sup>32</sup> as certain CD peaks correspond to particular secondary conformations that the protein may be in. However, CD spectroscopy could not locate the structures relative to other functional groups in space. Despite this, CD is a valuable tool for showing changes in molecular conformation, as a function of physical conditions, such as temperature denatures agents, salinity, etc.

The near - UV CD spectrum (>250 nm) of proteins provides information on the tertiary structure.<sup>33</sup> Unlike in the far - UV, the near – UV CD is not specific to any particular 3D structure. Rather, it provides structural information on the nature of the prosthetic groups in proteins, e.g., the heme groups in hemoglobin. CD spectroscopy in the visible is routinely deployed to study metal–protein interactions and can resolve individual d-d electronic transitions as separate bands.<sup>34</sup> Since CD spectra emerge only when the metallic compounds are located in chiral surroundings, visible CD is useful in identifying metal-organic groups in solution.

Besides probing the electronic structures of chiral molecules, the vibrational modes are also under close scrutiny, owing to an improved measurement precision and computational power.<sup>35</sup> Measurements on vibrational optical activity (VOA) often operate in infrared and near infrared ranges, where the molecules under study may stay in the ground electronic states and are only excited through vibrational transitions. The three main classes of VOA are: (1) Vibrational circular dichroism (VCD); (2) Vibrational circular birefringence (VCB); (3) Raman optical activity (ROA), where the strength of Raman scattering differs between right- and left-EM illumination.<sup>36</sup> VOA is a valuable tool in determining the absolute configuration of chiral molecules with up to ~200 atoms, by means of ab initio quantum-chemical simulations of the VCD and ROA spectra. The recent breakthrough in ultrafast VCD spectroscopy further extends its capability of studying protein dynamics in solution that is too fast to be examined otherwise.<sup>37</sup>

In general, CD gives less specific structural information than X-ray crystallography and protein NMR spectroscopy, which both give atomic resolution data. However, CD spectroscopy is a quick method that does not require large amounts of proteins or extensive data processing. Thus CD can be used to survey a large number of solvent conditions, varying temperature, pH, salinity, and the presence of various cofactors.

CD in most molecules is a very small effect (typical  $g$ -values of order  $10^{-3}$ ). The reason lies in the mismatch between the wavelength of light and the molecular size.<sup>1</sup> Typical wavelengths are hundreds of times larger than molecular diameters, so the pitch of the electromagnetic helix in CPL is hardly discernable to the molecule sitting in the field. For most molecules, the chirally sensitive transitions are smaller than regular absorptions by a factor of order  $R_{\text{mol}}/\lambda$ .

Another consequence of the relation  $R_{\text{mol}}/\lambda \ll 1$  is that the dissymmetry factors decrease with increasing wavelength of excitation. Although the exact amplitude depends on the electronic/vibrational structure of chiral species, the general trend holds true: typical values of  $g$ -values are  $10^{-3}$  in the UV/visible, and are  $10^{-4}$  -  $10^{-6}$  in the IR.<sup>35</sup>

In spite of the smallness of typical  $g$ -values, CPL may impart a slight chiral bias to a photochemical reaction, an effect first demonstrated in 1929 by Kuhn and coworkers.<sup>38</sup> While CPL-driven chiral photochemistry has subsequently been observed many times,<sup>39</sup> it has yet to become a practical tool because the effect is so weak.

In recent years interest has shifted toward using nonlinear spectroscopy and ideas from

coherent control to induce chiral transitions using light.<sup>10</sup> Theoretical proposals have suggested that large enantiomeric excesses could be attained,<sup>40, 41</sup> but the experimental work has mostly been limited to simple model systems.<sup>41</sup> The design of pulses for coherent control of molecular chirality is still a daunting theoretical challenge, and any solution to this challenge is specific to a single type of molecule.

Even if one restricts consideration to continuous wave (CW) solutions to Maxwell's equations (i.e. solutions sinusoidally varying in time), CPL is just one of an infinite number of such solutions. Could there be CW solutions to Maxwell's equations that show greater enantioselectivity than do circularly polarized plane waves? One could imagine an electromagnetic field with a particularly large twist, which couples strongly to molecular chirality. Any such field is likely to require nanostructures to set the appropriate boundary conditions.

### **1.5 Theory of optical activity: general considerations**

Wavelength of light is normally orders of magnitude larger than the size of molecules. Conveniently, textbooks of spectroscopy typically take advantage of this size mismatch to make what is called the "point-dipole approximation" (PDA), in which we assume that the electromagnetic field is perfectly uniform over the extent of the molecule. The PDA implies selection rules that govern which states can be reached via linear or nonlinear optical excitation. Dipole-forbidden transitions occur with probabilities smaller by powers of  $R_{\text{mol}}/\lambda \sim 1/200$  than dipole-allowed transitions. The small probabilities associated with these dipole-forbidden transitions means that under most conditions they

may be neglected. Natural optical activity, however, is one of the exceptions.

To understand the difference in response of molecules to right- and left-CPL, one needs to go beyond the PDA, and to include contributions that depend on  $R_{\text{mol}}/\lambda$ . This means that one needs to incorporate the interference between electric dipole moments and higher order multipolar moments (i.e. magnetic dipole and electric quadrupole moments).

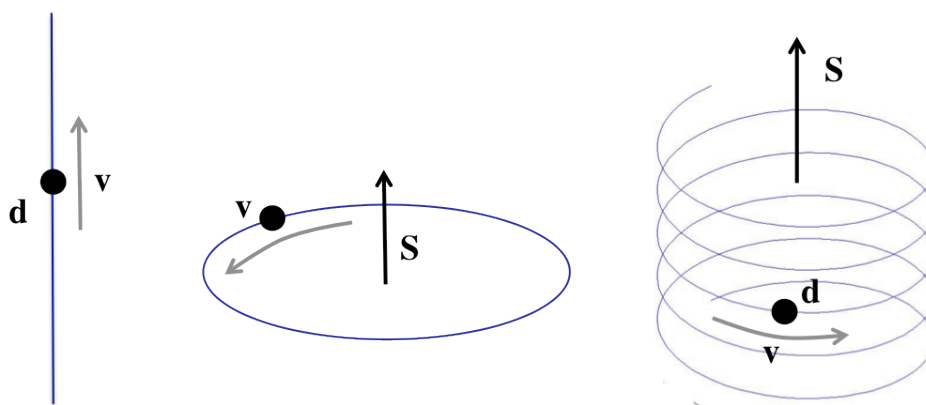


Figure 1.7 Simple model that exhibits the interference of magnetic and electric dipole moments in chiral molecules. Left: the particle confined to move along a straight line exhibits electric dipole excitation; Middle: the particle confined to circular exhibits magnetic dipole excitation; Right: the particle confined to in a helical configuration simultaneously exhibits electric and magnetic dipole moments.

The interference of different orders of multipolar moments in a chiral molecule may be manifested in a simple model, as shown in Figure 1.7: Let's consider one charged particle driven by an oscillating EM field. If the particle is confined to circulate in a planar loop at a velocity  $\mathbf{v}$ , the induced magnetic dipole moment may be derived as  $\mathbf{m} = I\mathbf{S} = q\mathbf{v}\mathbf{S}$ , where  $I$  is the current incurred by the moving charge and  $\mathbf{S}$  is the vector area of the loop.

In another scenario, the particle is limited to move along a straight line with a velocity

v. The geometry allows an electric dipole excitation, with the induced dipole moment  $\mathbf{p} = q\mathbf{d}(t_0) = q \int_0^{t_0} \mathbf{v}(t) dt$ , where  $\mathbf{d}(t_0)$  is the position of the particle at time  $t_0$ .

Now let's consider a helix-shaped trajectory, in which the particle,  $q$ , is allowed to reside. As the particle oscillates by the driving EM field, it simultaneously incurs a magnetic dipole moment,  $\mathbf{m}$ , due to the transverse component of circulation; and an electric dipole moment,  $\mathbf{p}$ , due to the longitudinal movement along the central axis. Therefore, the electric and magnetic dipole polarizability are intrinsically intertwined in the helical configuration, a paradigmatic example of chiral conformations.

In general, amplitudes of optical activity are proportional to the usual electric dipole polarizability tensor  $\tilde{\alpha}$  and the higher polarizability tensors  $\tilde{G}$  and  $\tilde{A}$  (a tilde denotes complex quantities, where the real and imaginary part may represent scattering and absorption, respectively). The tensor  $\tilde{\alpha}$  contains two electric dipole transition moments,  $\tilde{G}$  contains an electric dipole and a magnetic dipole transition moment, and  $\tilde{A}$  contains an electric dipole and an electric quadrupole transition moment. The contribution to the absorption/scattering strength from  $\tilde{\alpha}^2$  may be about  $10^3$  times that from the interference terms  $\tilde{\alpha}\tilde{G}$  and  $\tilde{\alpha}\tilde{A}$ , and about  $10^6$  times that from  $\tilde{G}^2$  and  $\tilde{A}^2$ . Furthermore, the  $\tilde{\alpha}\tilde{G}$  and  $\tilde{\alpha}\tilde{A}$  contributions have a circular polarization dependence, which enables them to be distinguished from the  $\tilde{\alpha}^2$ ,  $\tilde{G}^2$ , and  $\tilde{A}^2$  contributions.<sup>35</sup>

A rigorous treatment on quantifying chiroptical effects, with the aid of the optical chirality  $C$  in equation (1.1), may be found in section 2.2.

## 1.6 Molecular dark states and nano-enhanced optical transition

Molecules have a host of states that are only weakly coupled to, or simply invisible to, far-field radiation. This situation arises because the wavelength of plane waves of visible light ( $\lambda \sim 400 - 700$  nm) is vastly larger than the size of a typical molecule ( $R_{\text{mol}} \sim 0.5 - 2$  nm). Optical activity as we discussed in the section 1.5 is one exemplary transition between the so called “molecular dark states”.

In intermolecular processes the electromagnetic field due to one molecule may be highly nonuniform over the extent of a neighboring molecule, and thus “forbidden” transitions can play an important role. This statement is encapsulated within the multipole expansion of the intermolecular interaction. An arbitrary bounded distribution of charges and currents (e.g. a molecule) may be expanded as a series of multipoles, where the electric (or magnetic) field of the  $n^{\text{th}}$  multipole falls off as  $1/r^{n+2}$ . A point charge corresponds to a multipole of order  $n = 0$ , a dipole to  $n = 1$ , a quadrupole to  $n = 2$ , and so on. Coupling of the  $n^{\text{th}}$  multipole of molecule  $A$  to the  $m^{\text{th}}$  multipole of molecule  $B$  yields an interaction energy that falls off as  $(1/R_{AB})^{m+n+1}$ . For neutral molecules at large separation, only the dipole-dipole term remains, and the usual selection rules apply. But when the intermolecular spacing becomes comparable to the molecular size - as often happens in condensed matter—higher multipole moments contribute significantly and the cherished selection rules of far-field spectroscopy are relaxed.

Surface-enhancement effects are well known for molecules near metal surfaces, <sup>42, 43</sup> and such effects can lead to dramatic enhancements in fluorescence, <sup>44</sup> Raman signal <sup>45</sup>

and nuclear magnetic resonance spectroscopy.<sup>46</sup> Plasmon enhancement effects have also been used to polymerize photoresist<sup>47</sup> and to induce nonlinear processes such as two-photon excitation.<sup>48</sup> These phenomena are typically interpreted in terms of enhancement of the field strength alone; one remaining question is if spatially sculpted electric and magnetic fields may bring molecular dark states to light.

Table 1.2 provides a classification of the nano-enhanced optical transitions that have been either observed or predicted. Interesting and subtle effects arise from the enhancement of quantities other than the electric field strength. For instance, circular dichroism signals are enhanced for chiral molecules adsorbed near plasmonic nanoparticles.<sup>49, 50</sup> Enhanced Faraday rotation has also been predicted<sup>51</sup> and observed in magnetic nanoparticles<sup>52</sup> and nanohole arrays.<sup>53</sup> Here the effect arises from an increase in the effective wavevector of the radiation in the magneto-optically active medium.

Surface enhanced Raman scattering (SERS) is the most famous nano-enhanced spectroscopic effect.<sup>54</sup> The Raman signal from molecules adsorbed on “hot spots” of gold or silver nanoparticles is enhanced by up to *12 orders of magnitude* relative to the signal from the same molecules in bulk.<sup>55</sup> Much theoretical effort has been devoted to explaining this phenomenon. The current consensus is that the effect arises through three mechanisms:<sup>56</sup> 1) enhanced strength of the input field at the location of the molecule; 2) enhanced coupling of the molecular transitions to the scattered field; and 3) a “chemical interaction” involving charge transfer between the molecule and the nanoparticle. The

combination of the first two effects leads to a dependence on  $|E|^4$ , where  $E$  is the electric field strength at the location of the molecule.

Type of Transition	Electromagnetic quantity enhanced	Spectroscopic quantity enhanced
Electric dipole	$\langle  E ^2 \rangle$	Excitation, fluorescence, and photochemistry (same spectrum as far-field)
Magnetic dipole	$\langle  B ^2 \rangle$	Excitation and emission from “dark” states
Electric dipole-magnetic dipole interference	$\frac{1}{2} \left\{ \epsilon_0 \mathbf{E} \cdot (\nabla \times \mathbf{E}) + \frac{1}{\mu_0} \mathbf{B} \cdot (\nabla \times \mathbf{B}) \right\}$	Chiral asymmetry in excitation
Magnetic quadrupole	$\langle  \nabla B ^2 \rangle$	Intersystem crossing, leading to magneto-optic, magnetochemical, and magnetoelectronic effects
Raman	Unknown	Surface-Enhanced Raman Scattering

Table 1.2 Nano-enhanced optical transitions: Enhancement of different electromagnetic quantities leads to enhancement of different types of molecular transitions. The references and examples given are intended to be illustrative rather than exhaustive.

Several authors have pointed out that part of the SERS enhancement may also arise from increased electric field gradients near a nanostructure. These gradients can lead to SERS through two distinct mechanisms: 1) quadrupolar contributions to virtual transitions between ground and electronically excited states;<sup>57</sup> and 2) a “gradient field Raman” effect in which the electric gradient generates internal stresses in a molecule that lead to vibrational excitation.<sup>58</sup> SERS spectra often show different selection rules than bulk Raman spectra. Both of the gradient-enhanced mechanisms can account for these differences. Thus far there has been no unambiguous apportionment of SERS enhancements among the multiple possible contributing factors.

Another research interest of SERS lies in enhancing Raman optical activity signal. As with conventional circular dichroism, ROA signals are smaller than their achiral counterpart by a factor of  $\sim 10^3$ , due to the small size of a molecule relative to the wavelength of light. Metallic nanostructures can, in principle, enhance the ROA signal to an even greater degree than they enhance conventional Raman. This additional enhancement in surface-enhanced Raman optical activity (SEROA) arises through an interference between electric dipole and electric quadrupole contributions to the Raman scattering. While quadrupole transitions are only weakly excited by far-field radiation, they can be strongly excited in oriented molecules near a metallic nanostructure. This effect was first predicted by Efrima in the 1980s,<sup>59</sup> but in spite of continued theoretical work,<sup>60</sup> has lacked experimental verification until recently.<sup>61</sup>

Besides enhanced optical excitation in sculpted fields, a related topic is the enhanced spontaneous *emission* of molecules near nanostructures. The presence of a nanostructure may modulate the density of states into which a molecule may deposit its excitation energy, and thereby modulate the rate of spontaneous decay. Monolayers of dyes,<sup>62</sup> and single molecules<sup>63</sup> have been sandwiched in optical cavities, placed near metal tips,<sup>64</sup> or on metallic nanoparticles,<sup>65</sup> leading to dramatic changes in excited state lifetime. The direction of emission of a single molecule can also be influenced by a proximal metallic “nano antenna”.<sup>66</sup> Novotny’s book on Nano-Optics provides a nice discussion of such effects.<sup>67</sup> Also worth mentioning are experiments on fluorophores in liquid

micro-droplets.<sup>68, 69</sup> Here the liquid droplet forms a high  $Q$  resonant cavity and can dramatically enhance the rate of spontaneous emission of molecules contained within the cavity.

## 1.7 Natural and artificial structured materials

Structured materials, both natural and manmade, are known to exhibit striking optical properties and are able to facilitate optical transitions that are in absence or vanishingly weak in free space. In nature, micro- and nanometer-scaled patterns may cause diffraction and interference of incident light, and further result in characteristic iridescence of species. A simple example is opal, the national gemstone of Australia. Opal consists of silica spheres a few 100 nm in diameter self-assembled into regular lattices.<sup>70</sup> Opal's many colors derive from diffraction of the incident light on the self-assembled structures.

More complex patterns emerge in living creatures, such as butterflies, moths, birds, fish and plant, which are maintained and evolved for certain functional roles by means of natural selection. A well-known example are butterfly wings that are iridescent due to interference in tree-like nanostructures (Figure 1.8).<sup>71</sup> Moth eyes have anti-reflective microstructures, reducing eye glare and making them less visible to predators.<sup>72</sup> Stomatopod crustaceans are equipped with natural full-visible-range achromatic quarter-wave retarders in the eyes, consisting of uniaxial microvillar assembly of lipid Tubule.<sup>73</sup> And intriguingly the exoskeleton of some beetles has a chiral structure, making them appear differently under left- and right-CPL illumination.<sup>74</sup> Counterparts in nature

often surpass man-made devices in both sophistication and efficiency, and are a constant source of inspirations for scientists and engineers.

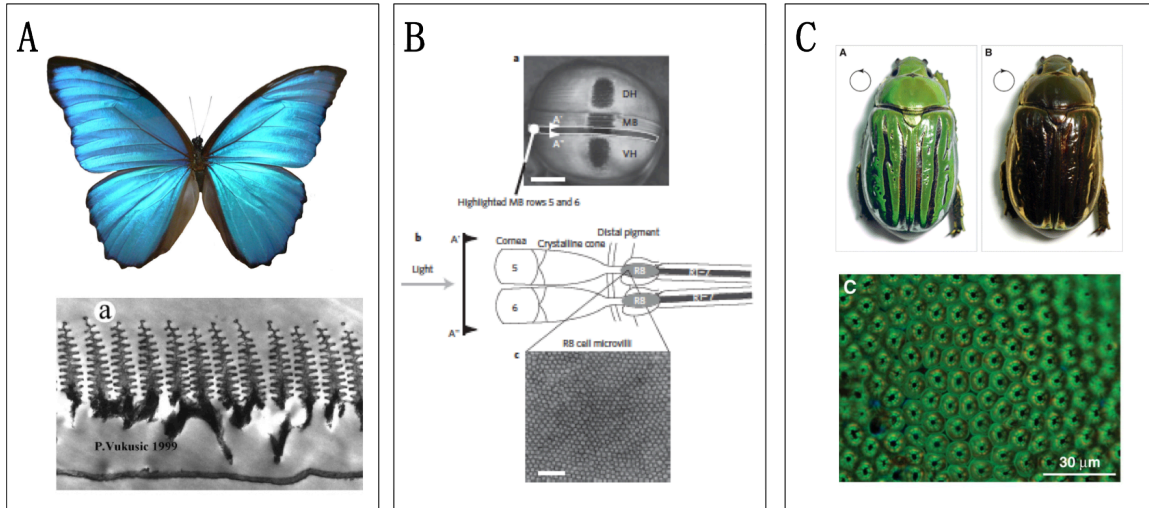


Figure 1.8 optical properties of selected structured materials in nature (A) butterfly wings; (B) Stomatopod crustaceans's eyes; (C) Beetle exoskeletons. The figures are adapted from references 71, 73 and 74.

The making of structured optical devices may date back to Roman Empire. During the period people started embedding gold and silver nanoparticles in glass, and achieved its color switch upon the choice of illumination schemes. A spectacular example is the Lycurgus Cup, which appears red or green, depending on whether or not the illumination passes through the glass.<sup>75</sup> The red color of medieval stained glass windows also derives from the surface plasmonic response of gold nanoparticles.

The color switch in the nanoparticle-embedded cup remained a mystery for long time. Understanding of the connection between structural arrangements and optical properties of material became possible through the invention of diffraction grating by Joseph von

Fraunhofer and the theoretical foundations of electromagnetism by James Clerk Maxwell, followed by the pioneering works of Lord Rayleigh. By studying the stacks of dielectric layers, today known as Bragg mirrors, Rayleigh understood how periodic structuring might cause total reflection of a particular wavelength at a certain incident angle. Since then, the vast advancement in both analytical (such as Mie solution to Maxwell's Equations) and numerical (such as Finite-difference time-domain method) toolkits enables the rational design of structured devices with desired functionality.

In parallel to the theoretical progression, rapid development has been made in experimental methods for preparing structures of minute physical scale and unprecedented sophistication. The mainstream of the so-called “nanofabrication techniques” uses energetic beams of electrons, ions and photons to etch or deposit patterns for certain functional aims, with a sub-nanometer resolution. Another class of techniques, instead, uses elastomeric stamps, molds, and conformable photomasks to fabricate and replicate structures. This “soft lithography” is named for its frequent use of elastomeric materials, most notably polydimethylsiloxane (PDMS). The two approaches are complimentary. For example, masks in “soft lithography” are often prepared by photolithography and/or electron-beam lithography, which both belong to the first class. Yet the etching and depositing tend to work well only with narrow classes of materials, and they can be prohibitively slow for use over large areas. A large-scale transfer of patterns by elastomeric masks, instead, is oftentimes preferred. During my PhD research, I employed both methods in sample preparation. The relevant details are presented in chapter 3 and 5.

## 1.8 Photonic metamaterials

Metamaterials are artificial structures of periodic arrays with the unit cell smaller than the excitation wavelength. They deform and/or redirect the incident light, owing to the subwavelength details of the structure rather than to their chemical composition.<sup>76</sup> Metamaterials as a research area was born in 1999, when John Pendry et al. suggested the use of split ring resonators to create artificial media with a negative permittivity.<sup>77</sup> In the same paper, he further proposed using a combination of split rings and wires to achieve negative refractive index, a seemingly unphysical phenomenon originally predicted by Victor Veselago in 1967.<sup>78</sup> Just half a year later, David Smith et al. demonstrated that the composite material exhibited simultaneous negative permittivity (wires) and negative permeability (split rings).<sup>79</sup>

The physical realization of negative refractive index attracted immense attentions, both for its fundamental novelty and many appealing potential applications (such as superlensing<sup>80</sup> as a famous example). The research on metamaterials gained additional momentum in 2006,<sup>81</sup> when Pendry *et al.* claimed the capability of the manmade structures for controlling light *at will*, with invisibility cloaking a direct consequence of the level of exacting manipulation.<sup>82</sup>

Photonic metamaterials are a subgroup of metamaterials that operate in terahertz, infrared, or even visible regimes. Physical dimensions of the subclass are often down to tens of nanometers.<sup>83</sup> To fulfill the desired functionality, multilayers of planar nanostructures and/or three-dimensional unit cells may be required (Figure 1.9). The two

primary techniques for fabricating a 3D periodic array are: (1) *Stacked electron-beam lithography* (Stacked - EBL).<sup>83,84</sup> In this technique, a layer of unit cells is fabricated by electron-beam lithography and subsequent planarization. The next layer of unit cells is again fabricated using electron-beam lithography aligned with respect to the first layer. Using this technique, researchers have achieved lateral interlayer alignments down to the 10 nm level. (2) *Direct-laser writing* (DLW).<sup>85, 86</sup> In the method, a tightly focused ultrafast laser is employed to incur polymerization in a photoresist material through a two-photon absorption at the focal point. A computer-assisted scan often accompanies to create an arbitrary three-dimensional pattern. If necessary, the polymer structures produced through DLW lithography can be filled with metal using electroplating.

Three-dimensional chiral metamaterials were proposed as an alternative route to obtain negative refraction.<sup>87</sup> Later, they were devised to achieve broadband polarization control<sup>85</sup> and ultrasensitive biomolecular detection.<sup>88</sup> Optical activity of the type of materials differs appreciably from both small chiral molecules and bulk chiral objects, yet the previous measurements are all subject to single-pixel detections. i.e. CD spectra taken by commercially available CD spectrometers.<sup>89-92e</sup> Given the nature of the structural inhomogeneity, a microscopy study on the chiral excitation may be informative. Moreover, the two primary fabrication techniques are exclusively employed for sample preparation. The integrated procedures, however, put challenges in placing molecules of interest in the vicinity of the highly contorted EM field. We, instead, seek alternative methods for preparing and examining the chiral nanostructures of interest.

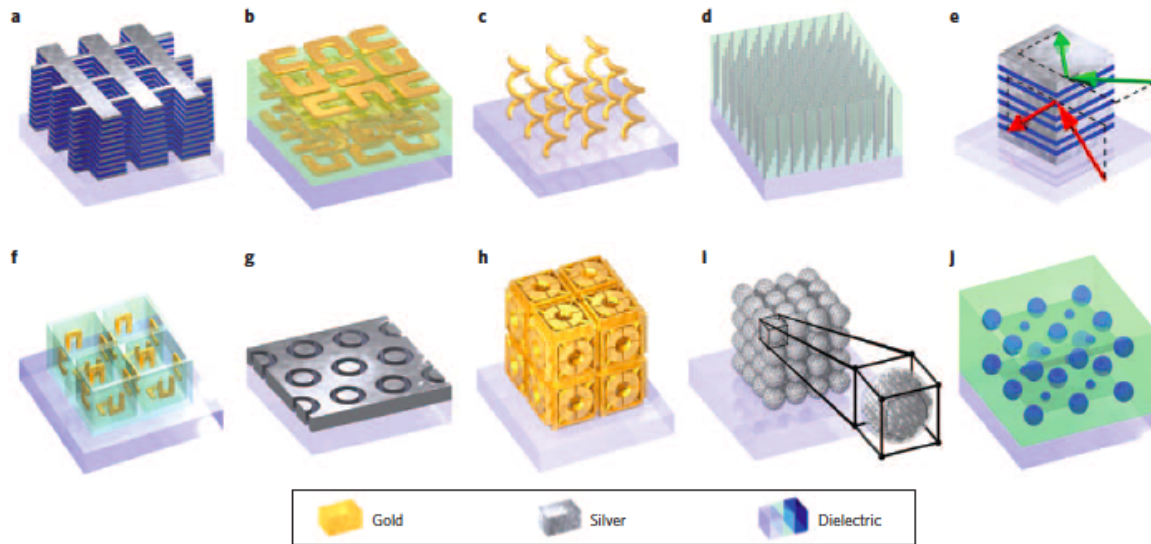


Figure 1.9 3D photonic-metamaterial structures. a, Double-fishnet negative-index metamaterial with several layers. b, 'Stereo' or chiral metamaterial fabricated through stacked electron-beam lithography. c, Chiral metamaterial made using direct-laser writing and electroplating. d, Hyperbolic (or 'indefinite') metamaterial made by electroplating hexagonal-hole-array templates. e, Metal-dielectric layered metamaterial composed of coupled plasmonic waveguides, enabling angle-independent negative  $n$  for particular frequencies. f, SRRs (Split-ring resonators) oriented in all three dimensions, fabricated using membrane projection lithography. g, Wide-angle visible negative-index metamaterial based on a coaxial design. h, Connected cubic-symmetry negative-index metamaterial structure amenable to direct laser writing. i, Metal cluster-of-clusters visible-frequency magnetic metamaterial made using large-area self-assembly. j, All-dielectric negative-index metamaterial composed of two sets of high-refractive-index dielectric spheres arranged on a simple-cubic lattice. The figure is adapted from reference 6.

# Chapter 2

## Theory on chirality of light

In section 1.5, we presented the theoretical framework on explaining optical activity of chiral molecules under circularly polarized light (CPL). Chirality of light, however, has not been under such examination so far. In this chapter, I start by proposing a quantitative measure of local handedness for arbitrary electromagnetic fields. Based on the quantity, I derive the existence of a superchiral solution to Maxwell's Equations that is more effective at distinguishing chiral species of opposite chirality than CPL. I further suggest the applicability of the current theory, and present a coupled-oscillator model that is suitable to describe metallic chiral structures of nanometer scale.

### 2.1 Optical chirality: a measure of EM handedness

Let's recall the definition of dissymmetry factor in conventional CD experiments:

$$g \equiv \frac{2(A^+ - A^-)}{A^+ + A^-} \quad (2.1)$$

where  $A^\pm$  is the molecular absorption rate in left ( $s^+$ ) or right ( $s^-$ ) CPL. We in the section seek for a measure of optical chirality that may be embodied in the dissymmetry factor from first principles. As we examined the published research, topological measures of chirality have been applied to plasma physics and astrophysics,<sup>93, 94</sup> fluid dynamics,<sup>95</sup> liquid crystals,<sup>96</sup> and Chern-Simons topological field theory.<sup>97</sup> To our surprise we have not found a discussion of this concept in relation to optical spectroscopy.

For non-plane wave EM fields, one expects the degree of dissymmetry to depend on local properties of the field. We begin by seeking a quantitative definition of the chirality of a vector field, independent of its interaction with matter. Chirality is time even (a movie of a right-handed screw shows a right-handed screw whether the movie is played forward or backward); parity odd (a mirror-image of a right-handed screw is a left-handed screw); and scalar (a right-handed screw remains right-handed no matter its orientation). Any measure of chirality must conform to the set of symmetry properties.<sup>29</sup>

In a chiral field, the field lines wrap around a central axis, but also have a component parallel to the axis. At the same time, we noticed a paper published in 1964 by Daniel Lipkin on the study of a set of bilinear invariants of the EM field.<sup>98</sup> While Lipkin and others dismissed them as lacking any physical significance,<sup>99,100</sup> we found that one of the quantities has both the required symmetry and mathematical picture. We renamed the quantity “optical chirality”:<sup>i</sup>

$$C \equiv \frac{1}{2} \left\{ \varepsilon_0 \mathbf{E} \cdot (\nabla \times \mathbf{E}) + \frac{1}{\mu_0} \mathbf{B} \cdot (\nabla \times \mathbf{B}) \right\}, \quad (2.2)$$

where  $\varepsilon_0$  and  $\mu_0$  are the permittivity and permeability of free space, respectively, and  $\mathbf{E}$  and  $\mathbf{B}$  are the time-dependent electric and magnetic fields. We see in the Table 2.1 that the quantity, optical chirality, completes the fundamental measures in EM theory.

Measures of chirality of the form  $q = \mathbf{A} \cdot \nabla \times \mathbf{A}$  have been introduced for a variety of physical transverse vector fields. Woltjer showed that, under suitable conditions,

---

<sup>i</sup> We deemed the original name “Zilch”, as Lipkin coined, no longer appropriate.

$\int \mathbf{A} \cdot \nabla \times \mathbf{A} d^3r$  gives a measure of the knottedness of the field lines of  $\nabla \times \mathbf{A}$ .<sup>93</sup>

Subsequent work continued to focus on global topological properties, rather than on local symmetry properties of chiral fields. Application to EM vector potentials, however, led to expressions that were not gauge invariant.<sup>101, 102</sup> By defining the EM chirality in terms of the fields rather than the potentials we avoid the problem of gauge dependence.

		Symmetry under mirror reflection			
		+	-		
scalar	Energy	$U \equiv \frac{1}{2} \left\{ \epsilon_0 \mathbf{E} \cdot \mathbf{E} + \frac{1}{\mu_0} \mathbf{B} \cdot \mathbf{B} \right\}$	<div style="background-color: #d8bfd8; padding: 5px;"> <b>Optical chirality</b>  <math display="block">C \equiv \frac{1}{2} \left\{ \epsilon_0 \mathbf{E} \cdot (\nabla \times \mathbf{E}) + \frac{1}{\mu_0} \mathbf{B} \cdot (\nabla \times \mathbf{B}) \right\}</math> </div>	+	Symmetry under time reversal
vector	Angular momentum	$\mathbf{J} \equiv \epsilon_0 \mathbf{r} \times (\mathbf{E} \times \mathbf{B})$	<div style="border: 1px solid black; padding: 5px;"> <b>Linear momentum</b>  <math display="block">\mathbf{p} \equiv \epsilon_0 \mathbf{E} \times \mathbf{B}</math> </div>	-	Symmetry under time reversal

Table 2.1 Conserved properties of the electromagnetic field, classified according to their symmetries. Optical chirality is a time-even pseudo-scalar.  $\epsilon_0$ , permittivity of free space;  $\mu_0$ , permeability of free space;  $\mathbf{r}$ , position vector.

## 2.2 Optical chirality in the interaction with matter

Is optical chirality observable? In the standard theory of CD the dissymmetry factor,  $g(\lambda)$ , measures the fractional difference in rates of excitation between left- and right-circularly polarized light at wavelength  $\lambda$ . In the section, we generalized the theory of CD to include pairs of arbitrary mirror-image fields.

The response of a molecule to an EM perturbation may be calculated at various levels

of theory<sup>17</sup> or obtained from experiment. Two approaches are presented here. The first is based on a response function-based description; and the second applies quantum time-dependent perturbation theory to examine a two-level chiral system. We will see that the two methods render equivalent results by the end.

We restrict attention to isotropic samples, for which the response tensors may be replaced by scalar response functions. The restriction to isotropic samples is necessary because in oriented samples even achiral molecules may show optical activity.<sup>103,104</sup>

### 2.2.1 Response function-based description

A chiral molecule subjected to monochromatic EM fields generates an electric dipole moment,  $\mathbf{p}$ , and a magnetic dipole moment,  $\mathbf{m}$ , given by:<sup>1,105</sup>

$$\begin{aligned}\tilde{\mathbf{p}} &= \tilde{\alpha}\tilde{\mathbf{E}} - i\tilde{G}\tilde{\mathbf{B}} \\ \tilde{\mathbf{m}} &= \tilde{\chi}\tilde{\mathbf{B}} + i\tilde{G}\tilde{\mathbf{E}}\end{aligned}\tag{2.3}$$

Quantities with a  $\sim$  are complex, e.g.  $\tilde{\alpha} = \alpha' + i\alpha''$ . The electric polarizability, magnetic polarizability, and optical rotatory strength are given by  $\tilde{\alpha}$ ,  $\tilde{\chi}$ , and  $\tilde{G}$ , respectively. In equation (2.3), one should take the real part of each side to obtain physical quantities. Electric quadrupole transitions contribute in the same order as magnetic dipole, but we neglect them here because the quadrupolar contribution to the differential absorption averages to zero in isotropic samples.<sup>106</sup>

In the most general time-periodic EM field, the electric and magnetic fields each describe an ellipse, with arbitrary relative phase and orientation. We consider a pair of fields with harmonic time dependence, from which we can build an arbitrary solution by

Fourier superposition. The fields are interchanged by application of Parity:

$$\begin{aligned}\tilde{\mathbf{E}}(t) &= \pm \tilde{\mathbf{E}}_0 e^{-i\omega t} \\ \tilde{\mathbf{B}}(t) &= \tilde{\mathbf{B}}_0 e^{-i\omega t} \end{aligned} \quad (2.4)$$

where again the real parts of  $\tilde{\mathbf{E}}(t)$  and  $\tilde{\mathbf{B}}(t)$  (denoted  $\mathbf{E}$  and  $\mathbf{B}$ ) describe the physical quantities.

In equation (2.4),  $\tilde{\mathbf{E}}_0$  and  $\tilde{\mathbf{B}}_0$  are arbitrary complex vectors.  $\mathbf{E}$  is odd under Parity while  $\mathbf{B}$  is even.

$$\text{The rate of excitation of the molecule is } A^\pm = \langle \mathbf{E} \cdot \dot{\mathbf{p}} + \mathbf{B} \cdot \dot{\mathbf{m}} \rangle = \frac{\omega}{2} \text{Im}(\tilde{\mathbf{E}}^* \cdot \tilde{\mathbf{p}} + \tilde{\mathbf{B}}^* \cdot \tilde{\mathbf{m}}),$$

where the brackets indicate an average over time and \* indicates the complex conjugate.

Expanding the rate of excitation using equation (2.3) we have:

$$A^\pm = \frac{\omega}{2} \left( \alpha'' |\tilde{\mathbf{E}}|^2 + \chi'' |\tilde{\mathbf{B}}|^2 \right) \pm G'' \omega \text{Im}(\tilde{\mathbf{E}}^* \cdot \tilde{\mathbf{B}}). \quad (2.5)$$

The term involving  $\chi''$  is negligibly small for most molecules and so we henceforth neglect it. We apply the identity  $\omega \text{Im}(\tilde{\mathbf{E}}^* \cdot \tilde{\mathbf{B}}) = \dot{\mathbf{B}} \cdot \mathbf{E} - \dot{\mathbf{E}} \cdot \mathbf{B}$  to the term involving  $G''$ .

Applying Maxwell's Equations in free space, we find  $A^\pm = \frac{1}{\epsilon_0} (2\omega U_e \alpha'' \mp CG'')$ , where

$U_e = \frac{\epsilon_0}{4} |\tilde{\mathbf{E}}|^2$  is the electric energy density and  $C$  is as defined in (2.2). We now generalize

the definition of  $g$  from equation (2.1) to include any pair of EM fields interchanged by

Parity, whereupon we find:

$$g = - \left( \frac{G''}{\alpha''} \right) \left( \frac{C}{\omega U_e} \right). \quad (2.6)$$

### 2.2.2. Calculation of chiral asymmetry using time-dependent perturbation theory

Here we calculate the interaction of a model two-level quantum system with a harmonically varying electromagnetic field with arbitrary spatial dependence. This

calculation reproduces equation (2.6) in the section 2.2.1. The rate of excitation of a chiral molecule subject to CPL is:

$$\Gamma^{(L/R)} = 2U_e (\sigma \pm \Delta\sigma), \quad (2.7)$$

where the absorption cross section  $\sigma$  and  $\Delta\sigma$  are given by the standard formulas:<sup>106</sup>

$$\sigma = \frac{\pi}{3\epsilon\hbar^2 \epsilon_0} |\mathbf{p}_{n0}|^2 \quad (2.8)$$

$$\Delta\sigma = \frac{2\pi}{3\epsilon c \hbar^2 \epsilon_0} \text{Im}(\mathbf{p}_{n0} \cdot \mathbf{m}_{n0})$$

where  $\mathbf{p}$  is the electric dipole operator and  $\mathbf{m}$  is the magnetic dipole operator. The molecule starts in its ground state 0 and undergoes a transition to an excited state  $n$ .

We now consider a chiral molecule subject to an arbitrary electromagnetic field and calculate the rate of excitation. The Hamiltonian is:

$$H = H_0 - \mathbf{p} \cdot \mathbf{E} - \mathbf{m} \cdot \mathbf{B} \quad (2.9)$$

The electric quadrupole term should be included at the same order, but for freely tumbling or randomly oriented molecules in space its contribution to CD vanishes.

Consider a pair of classical electromagnetic fields, related by a Parity operation:

$$\mathbf{E}(t) = \pm [\mathbf{E}_1 \cos(\omega t) + \mathbf{E}_2 \sin(\omega t)] \quad (2.10)$$

$$\mathbf{B}(t) = \mathbf{B}_1 \cos(\omega t) + \mathbf{B}_2 \sin(\omega t),$$

where  $\mathbf{E}_{1,2}$  and  $\mathbf{B}_{1,2}$  are arbitrary vectors. The electric and magnetic fields describe ellipses, with arbitrary relative phase and orientation. We make the rotating wave approximation

(neglecting terms in the Hamiltonian with dependence  $e^{i\omega t}$ ) and calculate the rate of one-photon excitation using Fermi's golden rule,  $\Gamma = \frac{2\pi}{\hbar} |V_{n0}|^2 \rho$ , where  $\rho$  is the density of final states and  $V_{n0}$  is the transition-matrix element.

The electric transition dipole is purely real and the magnetic transition dipole is purely imaginary.<sup>2</sup> Thus the squared transition-matrix element is:

$$|V_{n0}|^2 = \frac{1}{4} \left[ (\mathbf{E}_1 \cdot \mathbf{p}_{n0})^2 + (\mathbf{E}_2 \cdot \mathbf{p}_{n0})^2 + (\mathbf{B}_1 \cdot \mathbf{m}_{n0})^2 + (\mathbf{B}_2 \cdot \mathbf{m}_{n0})^2 \pm 2i [(\mathbf{E}_1 \cdot \mathbf{p}_{n0})(\mathbf{B}_2 \cdot \mathbf{m}_{n0}) - (\mathbf{E}_2 \cdot \mathbf{p}_{n0})(\mathbf{B}_1 \cdot \mathbf{m}_{n0})] \right] \quad (2.11)$$

We neglect terms quadratic in the magnetic field, average over all molecular orientations, and only consider times long relative to the optical period. The transition matrix element simplifies to:

$$\langle |V_{n0}|^2 \rangle_{\Omega} = \frac{\langle |\mathbf{E}|^2 \rangle_t}{6} |\mathbf{p}_{n0}|^2 \mp \frac{(\dot{\mathbf{B}} \cdot \mathbf{E} - \dot{\mathbf{E}} \cdot \mathbf{B})}{6\omega} \text{Im}(\mathbf{p}_{n0} \cdot \mathbf{m}_{n0}) \quad (2.12)$$

Substituting this expression into Fermi's Golden Rule yields:

$$\Gamma^{(L/R)} = \left( 2U_e \sigma \pm \frac{cC\Delta\sigma}{\omega} \right) \quad (2.13)$$

For the case of CPL, equation (2.13) reduces to equation (2.7). Equation (2.13) has the important consequence that the enantioselectivity of an arbitrary electromagnetic field is given by:

$$g = \left( \frac{cC}{\omega U_e} \right) \left( \frac{\Delta\sigma}{\sigma} \right) \quad (2.14)$$

Equation (2.14) is equivalent to equation (2.6).

### 2.3 Derivation of chiral continuity equation

Optical chirality is in many ways analogous to optical intensity. One can study the propagation of chirality through an optical system, calculate the distribution of chirality generated by an arbitrary time-dependent collection of charges and currents, and ask how matter couples to any chiral field. Chirality and intensity are both quadratic in the fields, so scaling all fields by a constant value does not change the ratio of chirality to intensity. Unlike intensity, optical chirality can be either positive or negative.

We present a continuity equation that governs the propagation of optical chirality.

Taking the time-derivative of equation (2.2) yields the relation:

$$\begin{aligned}
\frac{\partial C}{\partial t} &\equiv \frac{\epsilon_0}{2} \dot{\mathbf{E}} \cdot \nabla \times \mathbf{E} + \frac{\epsilon_0}{2} \mathbf{E} \cdot \nabla \times \dot{\mathbf{E}} + \frac{1}{2\mu_0} \dot{\mathbf{B}} \cdot \nabla \times \mathbf{B} + \frac{1}{2\mu_0} \mathbf{B} \cdot \nabla \times \dot{\mathbf{B}} \\
&= \frac{1}{2} \left[ \frac{1}{\mu_0} (\nabla \times \mathbf{B}) \cdot (\nabla \times \mathbf{E}) - \frac{1}{\mu_0} \mathbf{B} \cdot (\nabla \times (\nabla \times \mathbf{E})) - \frac{1}{\mu_0} (\nabla \times \mathbf{E}) \cdot (\nabla \times \mathbf{B}) + \frac{1}{\mu_0} \mathbf{E} \cdot (\nabla \times (\nabla \times \mathbf{B})) - \mathbf{j} \cdot \nabla \times \mathbf{E} - \mathbf{E} \cdot \nabla \times \mathbf{j} \right] \\
&= \frac{1}{2\mu_0} [\nabla \cdot (\mathbf{B} \times (\nabla \times \mathbf{E}) - \mathbf{E} \times (\nabla \times \mathbf{B}))] - \frac{1}{2} [\mathbf{j} \cdot \nabla \times \mathbf{E} - \mathbf{E} \cdot \nabla \times \mathbf{j}]. \tag{2.15}
\end{aligned}$$

In going from the first line of equation (2.15) to the second we applied Maxwell's Equations and in going from the second line to the third we used the identity  $\nabla \cdot (\mathbf{a} \times \mathbf{b}) = \mathbf{b} \cdot (\nabla \times \mathbf{a}) - \mathbf{a} \cdot (\nabla \times \mathbf{b})$  for arbitrary vector fields  $\mathbf{a}$  and  $\mathbf{b}$ .

Therefore,

$$\frac{\partial C}{\partial t} + \nabla \cdot \mathbf{F} = -\frac{1}{2} (\mathbf{j} \cdot \nabla \times \mathbf{E} + \mathbf{E} \cdot \nabla \times \mathbf{j}), \tag{2.16}$$

where quantity  $\mathbf{F} \equiv \frac{1}{2\mu_0} \{\mathbf{E} \times (\nabla \times \mathbf{B}) - \mathbf{B} \times (\nabla \times \mathbf{E})\}$  represents the flux of chirality. The

right hand side of equation (2.16) describes the interaction of chirality with material currents, and shows how matter can act as a source or sink of EM chirality.

Equation (2.16) has the same structure as Poynting's 1884 theorem<sup>107</sup> for flux of EM energy:  $\frac{\partial U}{\partial t} + \frac{1}{\mu_0} \nabla \cdot \mathbf{S} = -\mathbf{j} \cdot \mathbf{E}$ , where the EM energy density is  $U \equiv \frac{1}{2} \left( \varepsilon_0 |\mathbf{E}|^2 + \frac{1}{\mu_0} |\mathbf{B}|^2 \right)$ , the Poynting vector is  $\mathbf{S} \equiv \mathbf{E} \times \mathbf{B}$ , and the quantity  $\mathbf{j} \cdot \mathbf{E}$  describes how currents act as sources or sinks of EM energy. Chirality and energy need not flow in the same direction. For example, in left-CPL  $\mathbf{F}$  and  $\mathbf{S}$  are parallel, but in right-CPL they are antiparallel.

Finally, we note that conserved quantities and symmetry goes hand-in-hand, as ensured by Noether's theorem.<sup>108</sup> We conjecture that the conservation of optical chirality in vacuum may relate to the invariance of physics laws in electromagnetism under spatial reflection. We direct the interested readers to references<sup>109, 110</sup> for in-depth discussions.

## 2.4 Superchiral solution to Maxwell's Equations

We may rewrite the general dissymmetry factor in equation (2.6) by incorporating the parameters  $\alpha''$  and  $G''$  into  $g_{CPL}$ , where  $g_{CPL}$  is the dissymmetry factor under circularly polarized light:

$$g = g_{CPL} \left( \frac{cC}{2U_e \omega} \right). \quad (2.17)$$

Therefore, the search for superchiral solution to Maxwell's Equations translates into the following question: whether there exist fields for which  $|C| > 2U_e \omega / c$  in some regions of space, i.e. with greater chirality than that of a circularly polarized plane wave.

The answer is indeed "Yes". We are here to present one "superchiral" solution to Maxwell's Equations with surprising chiroptical properties.

The fields are everywhere circularly polarized, but modulated in amplitude in a

standing wave pattern. The remarkable finding is that, as the difference in the  $s^+$  and  $s^-$  amplitudes approaches zero, the chiral asymmetry at the nodes diverges. This divergence arises because, at a node,  $U_e$  goes to zero as  $(E_1 - E_2)^2$ , while  $C$  goes to zero as  $(E_1^2 - E_2^2)$ . The ratio  $C/U_e$  is thus proportional to  $(E_1 + E_2)/(E_1 - E_2)$ . The condition  $|g| < 2$  is enforced by the contribution from pure magnetic dipole transitions, which we have otherwise neglected. Nonetheless, enhancement of  $g$  by factors of several hundred is experimentally feasible, as shown below.

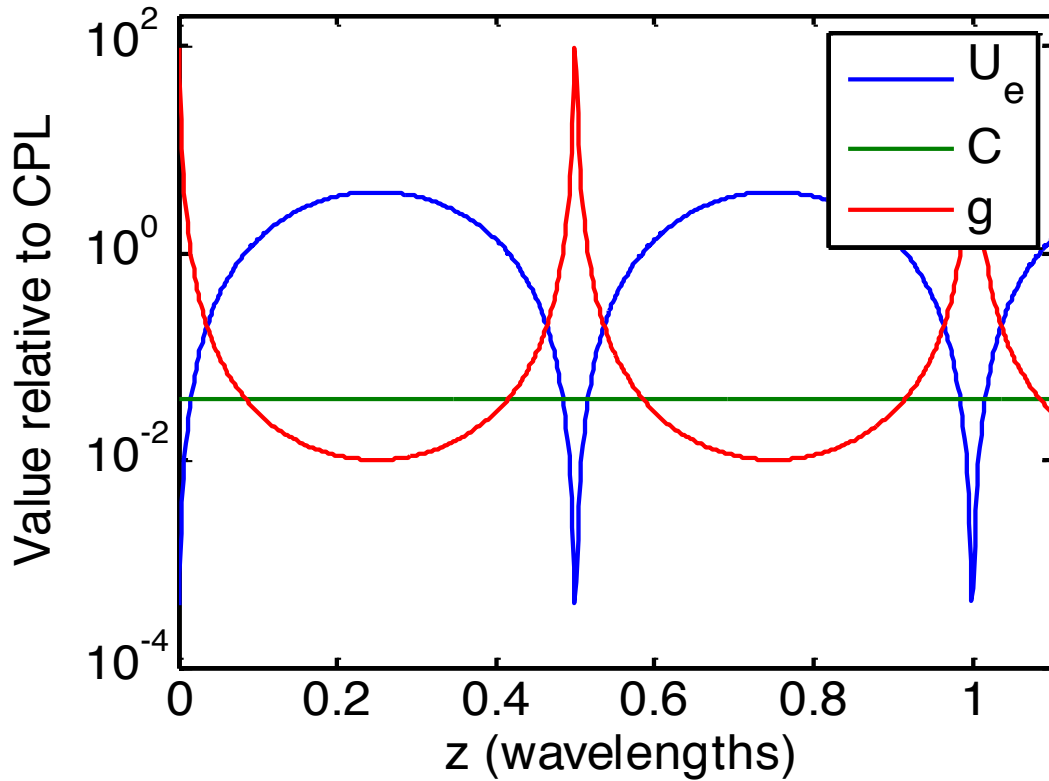


Figure 2.1 Enhanced chiral asymmetry in superchiral light. The intensity (blue) is modulated in a standing wave, while the optical chirality (green) is not. The ratio  $C = U_e$ , which determines the enantioselectivity (red), becomes large near a node in the standing wave. For this example,  $E_2 = 0.98E_1$ , and each quantity is plotted relative to its value for a single CPL plane wave.

We suggest a simple experiment to generate superchiral fields and to detect

enantioselective photoexcitation in these fields. The key challenge is to detect the excitation of a very thin film of chiral molecules, positioned with sub-wavelength precision in a superchiral standing wave. For the example of Figure 2.1, the regions in which  $g/g_{\text{CPL}} > 1$  have a thickness of  $0.032 \lambda$ , so for excitation with 355 nm light, this corresponds to a film thickness of 11 nm. The small volume of the enhancement region poses severe challenge in observing the superchiral effects.

Figure 1.2 illustrates an experimental schematic to generate a superchiral standing wave, with chiral molecules confined to a nodal plane. The key insight is that a superchiral standing wave is generated simply by reflecting CPL off a mirror at normal incidence: the reflected beam has the opposite chirality and direction, slightly lower amplitude, and fixed phase relative to the incident beam, leading exactly to the superchiral configuration.

Mathematically, let  $E_0$  and  $E_0'$  be the electric field amplitudes of the incident and reflected EM fields at normal incidence, respectively. The reflection coefficient is  $R = \left(\frac{E_0'}{E_0}\right)^2$ . The chirality is  $C = 2\frac{\omega\epsilon_0}{c}(E_0^2 - E_0'^2)$ . The optical chirality does not experience any interference and is independent of position. The energy density in the electric field is

$$U_e(z) = \frac{\epsilon_0}{2} [E_0^2 + E_0'^2 - 2E_0E_0' \cos(2kz)]. \quad (2.18)$$

At a node, the electric energy density reaches a minimum,  $U_e^{\text{min}} = \frac{\epsilon_0}{2}(E_0 - E_0')^2$ . From

equation (2.6), we see that the  $g$ -value of molecules confined to the node is:

$$g_{\max} = -\left(\frac{4G''}{c\alpha''}\right)\left(\frac{E_0 + E'_0}{E_0 - E'_0}\right) = g_{CPL}\left(\frac{1 + \sqrt{R}}{1 - \sqrt{R}}\right). \quad (2.19)$$

A silver mirror has a typical reflectivity of  $\sim 92\%$  throughout the visible part of the spectrum, whence we expect a 48-fold enhancement in the chiroptical asymmetry. For a 99% reflective mirror, one expects a nearly 400-fold enhancement.

## 2.5. Pictorial understanding of superchiral light

A more intuitive illustration of the superchiral enhancement comes from a pictorial approach. As suggested in section 1.4, the smallness of chiroptical effect is due to dimensional mismatch between wavelength of light and molecular size. That is, molecules may barely perceive helical pitch of chiral light field.

Helical pitch is determined by the rate of field-line reorienting around a central axis. In CPL, the rate of field-line reorientation is a constant. However, it is conceivable that the rate may be modulated in space, with an appropriate boundary condition set by a well-designed metallic and/or dielectric structure. Under the same wavelength excitation, more rapid reorientation of field-line leads to a larger chiral asymmetry.

Let  $\theta$  be the angle between field line at position  $z = z_0$  and at  $z = 0$ , and  $z$  be the axis of field propagation. The rate of field-line reorientation satisfies the following relation:

$$\frac{d\theta}{dz} = \frac{C}{4U_e} \quad (2.20)$$

Any change in the rate of field-line reorientation causes a corresponding modulation in  $C/U_e$ , which at the superchiral nodes appears as an enhancement in chiral excitation.

## 2.6 Chirality and polarization of standing waves

A closely related concept to optical chirality is polarization. In the section we distinguish the two attributes of light by giving a few field configurations, in which the two quantities behave very differently.

The polarization of an EM field describes the motion of the field vector within a single plane. Chirality relates to a fully three-dimensional property of the field. For propagating plane waves, chirality and circular polarization go hand in hand, but for more complex fields this needs not be the case. In particular, one can have fields that are everywhere linearly polarized, yet chiral; and one can have fields that are circularly polarized in places, yet everywhere achiral.

The fields we examine consist of standing waves, constructed from the interference of two plane waves counter-propagating along the  $z$ -axis. The waves have the same frequency but independently tunable amplitude. Each input wave has a polarization state selected from: linear vertical (V), linear horizontal (H), right CPL ( $\sigma^-$ ) or left CPL ( $\sigma^+$ ). Each field is labeled by the polarization states of the constituent plane waves, e.g.  $|H;V\rangle$  indicates horizontally polarized light coming from the left, interfering with vertically polarized light coming from the right. For each field we calculate the chirality and the ellipticity (i.e. polarization state), and show that these quantities are different. A summary of the field line distribution may be found in Table 2.2.

The ellipticities of the electric and magnetic fields are: <sup>111, 112</sup>

$$H_E = \frac{(\tilde{\mathbf{E}}^* \times \tilde{\mathbf{E}}) \cdot \hat{\mathbf{k}}}{2i|\tilde{\mathbf{E}}|^2}, \quad H_B = \frac{(\tilde{\mathbf{B}}^* \times \tilde{\mathbf{B}}) \cdot \hat{\mathbf{k}}}{2i|\tilde{\mathbf{B}}|^2}. \quad (2.21)$$

In the case where the Poynting vector is nonzero,  $\hat{\mathbf{k}}$  lies parallel to the Poynting vector. Otherwise  $\hat{\mathbf{k}}$  may be chosen to lie along either normal to the plane of polarization, and there is an overall ambiguity in the sign of  $H_E$  and  $H_B$ . In the discussion below we focus on the electric fields, but parallel arguments apply to the magnetic fields.

The two propagating plane waves are  $E_0 \boldsymbol{\varepsilon} e^{ikz}$  and  $E'_0 \boldsymbol{\varepsilon}' e^{-ikz}$ , where  $E_0$  is the amplitude of the wave,  $\boldsymbol{\varepsilon}$  is the polarization vector, and  $k$  is the magnitude of the wave vector. The total field is:

$$\tilde{\mathbf{E}}(\mathbf{z}) = E_0 \boldsymbol{\varepsilon} e^{ikz} + E'_0 \boldsymbol{\varepsilon}' e^{-ikz}. \quad (2.22)$$

We omit the  $e^{-i\omega t}$  time dependence because it cancels in the equation (2.21) for the ellipticity.

Field	Electric Field Magnetic Field	Chirality
$ H;V\rangle$		0
$ \sigma^+; \sigma^+\rangle$		$2 \frac{\omega \epsilon_0}{c} (E_1^2 + E_2^2)$
$ \sigma^+; \sigma^-\rangle$ superchiral		$2 \frac{\omega \epsilon_0}{c} (E_1^2 - E_2^2)$

Table 2.2 Chirality in optical standing waves. For each configuration the electric and magnetic fields are shown at intervals of  $\lambda/16$ . The fields lie in the plane perpendicular to the axis of propagation, but for illustration purposes each slice of the EM fields has been rotated to lie in the plane of the paper. The gray arrows represent the recent past positions of the field vectors. In the illustrations we have taken  $E_1 = E_2$  for the  $|H;V\rangle$  and  $|\sigma^+; \sigma^+\rangle$  configurations, and  $E_1 = 2E_2$  for the superchiral  $|\sigma^+; \sigma^-\rangle$  configuration.

### 2.6.1 $|H;V\rangle$ field configuration

This field consists of horizontally polarized light propagating from left to right and vertically polarized light propagating from right to left. The field is described by the

parameters:  $E_0 = E_0'$ ,  $\boldsymbol{\varepsilon} = \mathbf{e}_x$ , and  $\boldsymbol{\varepsilon}' = \mathbf{e}_y$ . Equation (2.22) gives for the electric field:

$$\tilde{\mathbf{E}}(\mathbf{z}) = \sqrt{2}E_0 \left[ \frac{\mathbf{e}_x + \mathbf{e}_y}{\sqrt{2}} \cos(kz) + i \frac{\mathbf{e}_x - \mathbf{e}_y}{\sqrt{2}} \sin(kz) \right] \quad (2.23)$$

According to equation (2.21), the electric ellipticity is  $H_E = \sin(2kz)$ . The polarization is linear at positions  $z = \frac{n\pi}{2k}$ , where  $n$  is an integer, and circular at  $z = \frac{\pi}{4k} + \frac{n\pi}{2k}$ .

Applying equation (2.2) we find that the optical chirality  $C = 0$ , everywhere.

### 2.6.2 $|\sigma^+; \sigma^+\rangle$ field configuration

This field consists of left-CPL propagating from left to right and left-CPL propagating from right to left. The field is described by the parameters  $E_0 = E_0'$ ,  $\boldsymbol{\varepsilon} = \frac{1}{\sqrt{2}}(\mathbf{e}_x + i\mathbf{e}_y)$ ,

and  $\boldsymbol{\varepsilon}' = -\frac{1}{\sqrt{2}}(\mathbf{e}_x - i\mathbf{e}_y)$ . Equation (2.22) gives for the electric field:

$$\tilde{\mathbf{E}}(\mathbf{z}) = \sqrt{2}iE_0 [\mathbf{e}_x \sin(kz) + \mathbf{e}_y \cos(kz)] \quad (2.24)$$

According to equation (2.21),  $H_E = 0$  everywhere. The field is linearly polarized with its polarization axis rotating around  $z$  axis. Applying equation (2.2) we find that the optical

chirality  $C = 2 \frac{\omega \varepsilon_0}{c} E_0^2$ , everywhere.

### 2.6.3 $|\sigma^+; \sigma^-\rangle$ field configuration

This is the superchiral field considered in the section 2.4. It consists of left-CPL propagating from left to right and right-CPL propagating from right to left. Here we consider the case where the two plane waves may be of different amplitudes:  $E_0$ , and  $E_0'$ .

The polarization vectors are:  $\boldsymbol{\varepsilon} = \frac{1}{\sqrt{2}}(\mathbf{e}_x + i\mathbf{e}_y)$ ,  $\boldsymbol{\varepsilon}' = -\frac{1}{\sqrt{2}}(\mathbf{e}_x + i\mathbf{e}_y)$ .

Equation (2.22) gives for the electric field:

$$\tilde{\mathbf{E}}(\mathbf{z}) = \frac{1}{\sqrt{2}} \left\{ (E_0 - E'_0)\cos(kz)\mathbf{e}_x - (E_0 + E'_0)\sin(kz)\mathbf{e}_y \right] + i \left[ (E_0 - E'_0)\cos(kz)\mathbf{e}_y + (E_0 + E'_0)\sin(kz)\mathbf{e}_x \right] \right\} \quad (2.25)$$

According to equation (2.21),  $H_E = 1$  everywhere. This field is circularly polarized in all space, although the amplitude is modulated with period  $\pi/k$ . Applying equation (2.2) we

find that the optical chirality  $C = \frac{\omega\boldsymbol{\varepsilon}_0}{c}(E_0^2 - E_0'^2)$ , everywhere.

## 2.7 Optical Chirality in nano-regime

The present theory is limited to chiroptical effects arising from an interference between electric dipole and magnetic dipole transitions, and to EM fields sufficiently weak that the material response remains linear in the fields. Interesting chiroptical phenomena occur outside these bounds.

Harris and coworkers showed that there is no single measure of chirality appropriate to all material bodies: for any measure, one can construct a chiral body for which the measure is zero.<sup>96</sup> Thus, electric dipole-magnetic dipole interferences may not be the dominant contributors to a body's chiroptical response; higher multipole moments may be necessary. This situation arises under far field illumination when the size of the body is comparable to the wavelength of light, such as with chiral polymers or cholesteric liquid crystals. Higher multipole transitions may also be important under near-field illumination when the field is highly contorted over the size of a single molecule, such as may arise near metallic

nanostructures. An infinite set of chiral parameters has been suggested to describe the geometry of a chiral body,<sup>113</sup> and so there exists an infinite set of parameters to describe its chiroptical response.

Similarly, there cannot be a single measure of electromagnetic chirality appropriate to all EM fields. There exist chiral fields for which  $C$  as defined in equation (2.2) is zero. Indeed, the field of any static, chiral configuration of point charges is chiral, yet by equation (2.2),  $C = 0$ . This claim is proved by noting that  $\nabla \times \mathbf{E} = -\frac{\partial \mathbf{B}}{\partial t}$  but  $\mathbf{B} = 0$  for a configuration of static point charges. Yet chiral fields with  $C = 0$  may undergo chirally selective interactions. The optical chirality of equation (2.2) may be part of a hierarchy of bilinear chiral measures that involve higher spatial derivatives of the electric and magnetic fields.<sup>114</sup> We speculate that all linear chiral light-matter interactions can be described by sums of products of material chiralities and time-even pseudoscalar optical chiralities.

In the context of nonlinear optics, time-even pseudoscalar measures of EM chirality can be constructed from third and higher powers of the electric and magnetic fields, and are distinct from  $C$ . For instance, magneto-chiral dichroism is proportional to the product of a magnetic field and two electric fields;<sup>1</sup> and chiral sum frequency generation is proportional to the product of three electric fields.<sup>115</sup>

Given our field of expertise and the active research on metallic nanostructure, we decided to examine chiral properties of a 3D plasmonic configuration. As for any metallic chiral structure with the size significantly smaller than the wavelength of incident light, quasi-static approximation may be applied. In such a configuration, far-field calculation

fails.

In 1929, Kuhn introduced a simple classical model for a chiral molecule, consisting of two dipolar oscillators, displaced vertically from each other by a distance  $h$ , and rotated about the displacement axis by an angle  $\theta$ .<sup>116</sup> For rotation angles that are not multiples of  $90^\circ$ , these oscillators form a chiral configuration, called the “twisted H”. This simple model became the paradigm for many subsequent treatments of circular dichroism, including extensions to quantum oscillators,<sup>117</sup> to more realistic models of molecular response,<sup>1</sup> and to retarded dipole-dipole interactions.<sup>118</sup>

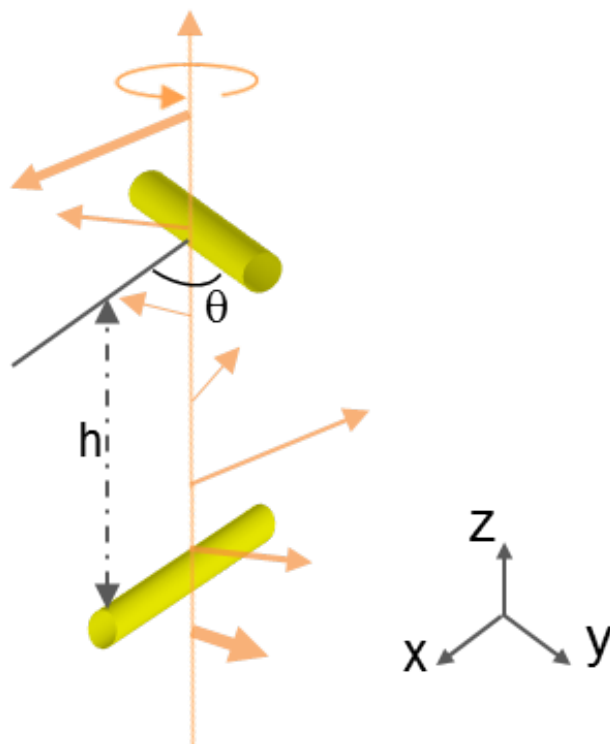


Figure 2.2 The twisted H configuration. The two polarizable anisotropic particles are oriented at an angle  $\theta$ , and separated by  $h$ .

We consider two identical anisotropic polarizable particles, located at  $\mathbf{r}_1 = (0,0,0)$  and  $\mathbf{r}_2 = (0,0,h)$ . The principal axes of the particles are  $\boldsymbol{\mu}_1 = \hat{\mathbf{x}}$  and  $\boldsymbol{\mu}_2 = \hat{\mathbf{x}} \cos \theta + \hat{\mathbf{y}} \sin \theta$ . The particles are exposed to circularly polarized illumination, with electric field  $\mathbf{E}^{(0)} = E_0(\hat{\mathbf{x}} \pm i\hat{\mathbf{y}})e^{i(kz - \omega t)}$ . This field propagates along  $\hat{\mathbf{z}}$ , with wave vector  $\mathbf{k}$  and angular frequency  $\omega$ . The  $+$  and  $-$  signs represent left- and right-circular polarization, respectively.

If we neglect dipole-dipole coupling, then the polarization of each particle is  $\mathbf{P}_i^{(0)} = \boldsymbol{\alpha}_i \cdot \mathbf{E}_i^{(0)}$ , where  $i = 1$  or  $2$ , and  $\boldsymbol{\alpha}_i$  is the frequency-dependent complex polarizability tensor. The single-rod polarizability is:

$$\boldsymbol{\alpha}_i = \varepsilon_0 AVR(\phi_i) \begin{pmatrix} 1 & 0 \\ 0 & \rho e^{i\beta} \end{pmatrix} R(-\phi_i), \quad (2.26)$$

where  $r$  and  $b$  measure linear dichroism and linear birefringence respectively, and the overall amplitude and phase of the particle response are determined by a complex coefficient  $A = A_0 e^{i\psi}$ . These four parameters ( $r$ ,  $\beta$ ,  $A_0$ , and  $\psi$ ) depend on the frequency of illumination, the composition of the particle, and its shape. The rotation matrix  $R(\phi)$  accounts for the orientation of the particles ( $\phi_1 = 0, \phi_2 = \theta$ ).  $V$  is an effective volume for the particle.

To introduce enantioselection, we include coupling between the two dipoles. Oscillating dipole  $\mathbf{P}_j^{(0)}$  induces a first-order correction to the electric field  $\mathbf{E}_i^{(1)}$  at location  $\mathbf{r}_i$ , ( $i, j = 1, 2; i \neq j$ ). The electric field propagates according to the retarded Green's function:

$$\mathbf{E}_j^{(1)} = \Gamma(\mathbf{r}_{ij}) \mathbf{P}_i^{(0)},$$

where

$$\Gamma(\mathbf{r}) = (3\hat{\mathbf{r}}\hat{\mathbf{r}} - \mathbf{1}) \left( \frac{1}{r^2} - \frac{ik}{r} \right) \frac{e^{ikr}}{4\pi\epsilon_0 r} + (\mathbf{1} - \hat{\mathbf{r}}\hat{\mathbf{r}}) \frac{k^2 e^{ikr}}{4\pi\epsilon_0 r} - \frac{1}{3\epsilon_0} \delta^3(\mathbf{r}) . \quad (2.27)$$

In the first Born approximation we neglect higher-order couplings between the rods (i.e. multiple scattering events). We used the far-field limit of Eq. 2 which, for displacements along the  $z$ -axis, becomes

$$\Gamma_{ff}(z) = \frac{k^2 e^{ikz}}{4\pi\epsilon_0 z} \quad (2.28)$$

The total dipole  $\mathbf{P}_i$  becomes:

$$\mathbf{P}_i = \boldsymbol{\alpha}_i \cdot (\mathbf{E}_i^{(0)} + \mathbf{E}_i^{(1)}). \quad (2.29)$$

We consider a detector located at height  $z$  (assuming  $z \gg h$ ). The electric field at the detector is:

$$\mathbf{E}_d(z) = \Gamma_{ff}(z) \mathbf{P}_1 + \Gamma_{ff}(z-h) \mathbf{P}_2 + \mathbf{E}^{(0)}(z) . \quad (2.30)$$

Eq. (5) is evaluated successively for left- and right CPL, to yield electric fields at the detector  $\mathbf{E}_d^+$  and  $\mathbf{E}_d^-$ . The measured dissymmetry factor,  $g$ , equals

$$g = \frac{2(|\mathbf{E}_d^+|^2 - |\mathbf{E}_d^-|^2)}{|\mathbf{E}_d^+|^2 + |\mathbf{E}_d^-|^2}. \quad (2.31)$$

In Chapter 5, we will apply equation (2.31) to fit experimental data on a coupled-dipole structure, and reveal remarkable features of its chiral excitation, both spatially and spectrally.

# Chapter 3

## Experimental material and apparatus

Experiments on optical activity of chiral matter are notoriously difficult.<sup>3</sup> The smallness of signal, often on the order of  $10^{-3}$  or less, puts severe challenges in the stability and sensitivity of measurement system. Moreover, superchiral enhancement only takes place within a narrow region of a fraction of wavelength at the nodes of a standing wave,<sup>119</sup> putting a further constraint on the available amount of molecules to detect.

In this chapter, I illustrate the apparatus we employed for assessing spatial distribution of chiral excitation over a thin film. The detailed discussions include the choice of polarization optics, the possible artifacts in the measurement, and the fluorescent molecules that we either prepared or used. In the end, I present a case study on how artifacts may easily sneak in and complicate the data interpretation in a single-molecule measurement of chiral fluorophores.

### 3.1 Imaging of fluorescence-detected circular dichroism (FDCD)

To observe enantioselective photoexcitation in a superchiral field, one must localize chiral molecules to a very thin film. For the example of Figure 2.1, the regions in which  $g/g_{\text{CPL}} > 1$  have a thickness of  $0.032\lambda$ . For excitation with light at 355 nm, the film thickness must be  $< 11$  nm. It is unrealistic to detect absorption in such a thin sample, but fluorescence provides a highly sensitive measure of the rate of excitation. Fluorescence

detected circular dichroism<sup>120</sup> can, in principle, be observed on single molecules,<sup>121</sup> though claims that this has been achieved have not been substantiated.<sup>122</sup> For the present purposes, one may signal-average over an area millimeters wide, containing millions of molecules.

As the superchiral enhancement is highly inhomogeneous in space, an imaging system that maps chiral excitation over a large field of view will be ideal. As most of the electro-optical devices operate either at high frequency (such as PEM) or under high voltage (Pockels cell and AOM), we attempted to avoid the complexities by devising a wide-field imaging system operating below frame rate of an EMCCD (electro-multiplying CCD) camera. That left us with wave plates and liquid crystal variable retarder (LCVR) as polarization modulators. In the section, we are to introduce in detail the working principle and choice of the various polarization optics. Other aspects of the imaging apparatus will be discussed as well.

Operating procedure of the wide-field imaging module will be elaborated in the next chapter.

### **3.1.1 Polarization optics**

Polarization as one intrinsic property of light has been a key dimension in controlling EM waves for desired functionalities. Accordingly, many types of polarization modulators are available. In general, polarization optics may be sorted in two categories. The first is a set of mechanical devices based on linear birefringence or linear dichroism of the chosen material. Polarization of incident light is modulated by changing relative

orientation of a few of such optical elements. The second are electro-optical units where voltage is applied to modulate polarization properties of material such as nonlinear crystal,

<b>Operation</b>	<b>Name</b>	<b>Pro</b>	<b>Cons</b>
<b>Mechanical</b>	<b>Polymer plate</b>	<ul style="list-style-type: none"> <li>• Uniform retardance</li> <li>• Wide spectrum coverage</li> <li>• Easy handling</li> </ul>	<ul style="list-style-type: none"> <li>• Mechanical rotation</li> <li>• Material defects</li> </ul>
	<b>Crystal plate</b>		
<b>Electrical</b>	<b>LCVR</b>	<ul style="list-style-type: none"> <li>• Minimum mechanical perturbation</li> <li>• Full wavelength retardance</li> </ul>	<ul style="list-style-type: none"> <li>• Not available in the UV</li> <li>• Fast axis wander <math>\sim 6^\circ</math></li> </ul>
	<b>EOM and Pockels Cell</b>	<ul style="list-style-type: none"> <li>• Minimum mechanical perturbation</li> <li>• Good transmission at UV</li> </ul>	<ul style="list-style-type: none"> <li>• High voltage required</li> <li>• Nonuniform retardance</li> </ul>
	<b>PEM</b>	<ul style="list-style-type: none"> <li>• Minimum mechanical perturbation</li> <li>• Coverage from UV to IR</li> </ul>	<ul style="list-style-type: none"> <li>• Modulated interference</li> <li>• Acoustic noise</li> <li>• High working frequency</li> </ul>

Table 3.1 Pros and cons of selected polarization optics

fused silica, and liquid crystal. A summary of different types of polarization optics may be found in Table 3.1

### 3.1.1.1 Mechanically driven polarization optics

The mechanically driven polarization units include polarizer and wave plates (half-wave and quarter-wave).

Linear polarizer, as the name suggested, creates linear polarization as light propagates through the optical element. Two types of polarizers were employed in different experiments in the thesis study. The first is called Glan-Taylor polarizer, which is made of birefringent, calcite crystals. Due to the birefringent structure of calcite, a differential delay is created between two orthogonally polarized waves traveling in the crystal. As

shown in Figure 3.1(A), this birefringent structure creates a polarization-dependent refraction that effectively steers the polarization planes in two angles. While the ordinary plane will travel straight through the crystal, the extraordinary plane will exit the crystal at an angle proportional to the wavelength as well as the length of the crystal.

Glan-Taylor polarizer has an extremely high extinction ratio (in the range of 100,000:1) and wide spectrum coverage (from 300 nm to 2  $\mu\text{m}$ ). However, it normally has small acceptance angle, i.e. extinction ratio of the polarizer degrades rapidly as light beam derails from normal incidence. This is particularly problematic for light beam of large N.A., where output light may have inhomogeneous polarization within the light spot.

An alternative to Glan-Taylor polarizer is the nanoparticle-based polarizers. It is a thin glass plate with silver nanoparticles embedded near both surfaces (Figure 3.1 (B)). Each nanoparticle acts as a polarization dependent and wavelength selective absorber – just like a dipole antenna. Surface plasmons are excited to resonate and thus absorb incident light of certain polarization state, while the rest is free to propagate through. A combination of particle shape and size are selected to ensure high extinction ratio and wide spectral range of function. This type of polarizer has an acceptance angle  $\sim 20$  deg., so is ideal to use with light source other than laser.

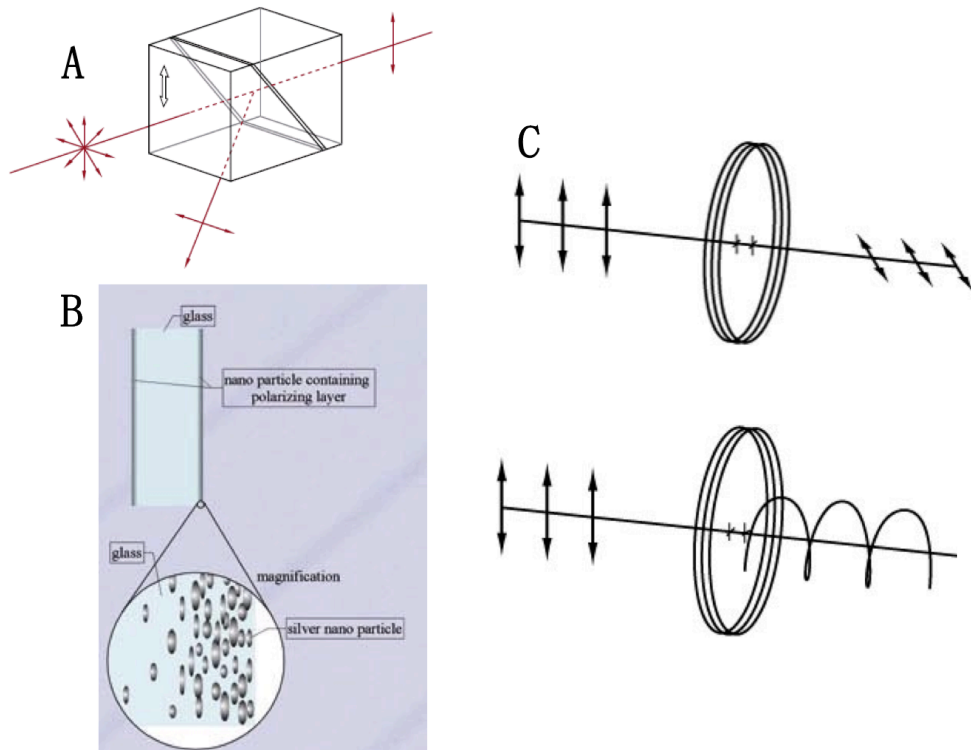


Figure 3.1 Working principles of selected linear polarizers and wave plates (A) Glan-Taylor polarizer; (B) nanoparticle-based polarizer; (C) half wave-plate (up) and quarter wave-plate (down). The figures are adapted from Thorlabs (A and C) and CODIXX website.

Wave plates are optical elements that create certain polarization state from linearly polarized incident light. They are constructed from birefringent materials, commonly fused silica, that introduce a phase difference between the fast and slow principal axis of the wave plate. A phase shift of  $\pi/2$  corresponds to a quarter wave plate (QWP), which subsequently converts linear to circular polarization, and a phase shift of  $\pi$  corresponds to a half wave plate (HWP). HWP effectively rotates the polarization plane of incident light by  $2\theta$ , where  $\theta$  is the angle between HWP's fast axis and the plane of incident polarization. (Figure 3.1(C))

### 3.1.1.2 Electrically driven polarization optics

Varieties of electrically-driven polarization modules are available. Out of the many, I will elaborate the working principles of Photoelastic modulator (PEM) and liquid crystal variable retarder (LCVR), as we have used the two in chiroptical measurement.

PEM is based on the photoelastic effect, in which a mechanically stressed sample exhibits birefringence proportional to the resulting strain. The precise oscillation frequency is determined by the properties of the optical element/transducer assembly. The transducer is tuned to the resonance frequency of the optical element along its long dimension, determined by its length and the speed of sound in the material. A current is then sent through the transducer to vibrate the optical element through stretching and compressing that change the birefringence of the transparent material. The resonant character leads to large amplitudes of modulation, while also limit operation at a single frequency, normally at 50 or 20 KHz.

LCVR is essentially a tunable wave plate by changing the effective birefringence of the material with applied voltage, thus altering the input polarized light to any chosen elliptical, linear or circular polarization. The core materials are anisotropic nematic liquid crystal molecules forming uniaxial birefringent layers in the liquid crystal cell. On average, molecules are aligned with their long axes parallel, but with their centers randomly distributed as depicted in Figure 3.2. With no voltage applied, the liquid crystal molecules lie parallel to the glass substrates and maximum retardation is achieved. When voltage is applied, liquid crystal molecules begin to tip perpendicular to the fused silica windows as

depicted in Figure 3.2. The response time for the device to switch from zero to half-wave is on the order of 10 ms, which limits the operating frequency below 100 Hz.

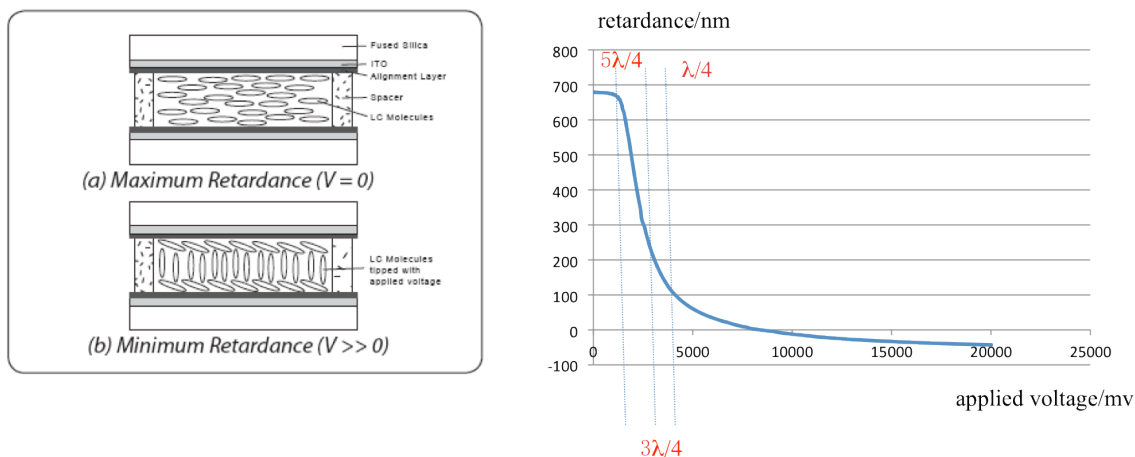


Figure 3.2 Working principle of Liquid crystal variable retarder (LCVR). Left: molecular arrangements in the LCVR (a) without and (b) with applied voltage. Right: retardance at 632 nm as a function of applied voltage. The figure on the left is adapted from Meadowlark website.

### 3.1.1.3 On the choice of polarization optics

We decided to build a wide-field imaging module that maps the spatial distribution of chiral excitation over a thin film of chiral fluorophores. In the system, an EMCCD was employed to record the images of chiral fluorophores under optical excitation of opposite chirality. The slow frame rate excludes the use of most electro-optical devices.

Mechanically driven polarization optics is an appealing option. Rotation of wave plates, however, projects defects, dents and stripes within the plates onto the image plane. These artifacts are dominant over small chiroptical signal. (Figure 3.3). Instead, LCVR is an electric-driven wave plate, with no moving part attached. The device may operate at

low frequency, compatible with most imaging devices. We combined a linear polarizer and an LCVR as a polarization module, and further integrated it with an EMCCD (Andor iXon+). The system is capable of detecting fractional chiral image of  $10^{-5}$  in the field of

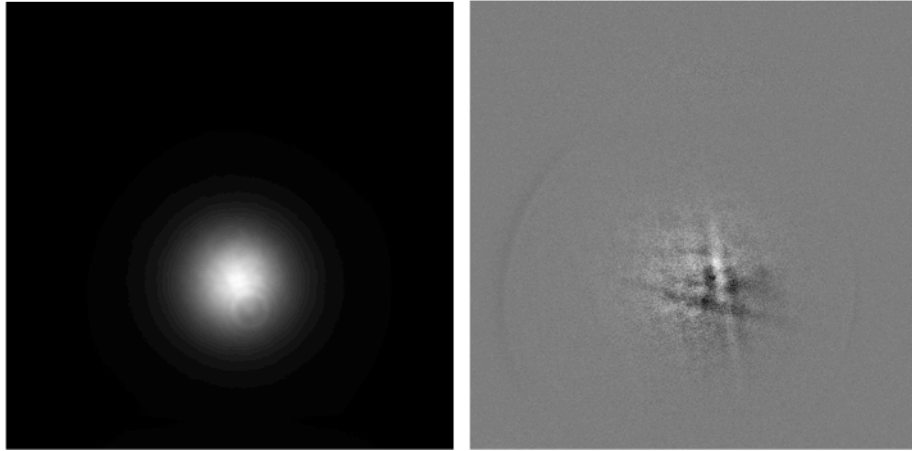


Figure 3.3 Defects in wave-plates. Left: the image of a light beam on an EMCCD. The light beam traveled through a wave plate. Right: differential image of laser spot through a wave plate at two orientations. The lines are defected that are inherent to the plate.

view, with mechanical drift less than  $0.5 \text{ \AA}$  over the course of a 20-minute experiment.

### 3.1.2 Imperfection of light source

Light sources, specifically lasers, are also a source of artifacts. Careful calibration and compensation are required to ensure a successful measurement. Three issues of concern are: (1) spectral impurity; (2) power fluctuation; (3) pointing instability.

Lasers have plasma emission at other wavelengths, which are in general vanishingly small. Therefore, the spectra impurity due to plasma is ignorable in most applications. However as we are looking for fractional signal on the order of  $10^{-3}$  or less, a narrow-band excitation filter is required to remove unwanted signal from excitation at other wavelength.

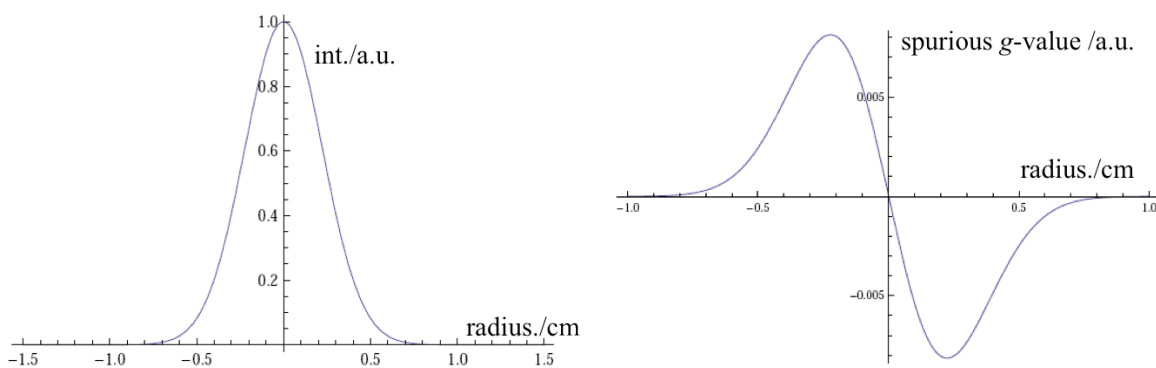


Figure 3.4 Calculated spurious  $g$ -value incurred by pointing instability. Left: distribution of laser intensity as a function of radius. We assumed a Gaussian distribution in the calculation. Right: the predicted dissymmetry factor as a function of radius, giving a pointing instability of 0.05 mrad. It is calculated by considering the lateral shift of laser spot at two extremes, and subtracting one from the other.

Power fluctuation is another common problem in the precise measurement. It results partially from quantum noise (associated with laser gain and resonator losses) and partly from technical noise sources such as excess noise of the pump source, vibrations of resonator mirrors, thermal fluctuations in the gain medium. The fractional intensity fluctuation may be up to 1 - 2%, one order of magnitude larger than the chiral signal. Accordingly, we devised a special arrangement in the sample preparation to compensate for any intensity noise, which will be discussed in detail later.

The direction of the output laser emission is subject to some beam pointing fluctuations. Pointing instability translates into lateral movement of the laser spot upon illuminating the sample, and thus degrades the measurement precision. As shown in Figure 3.4, a pointing instability of 0.05 mrad may cause a spurious dissymmetry factor of  $5 \times 10^{-3}$  in our setup.

Pointing instability originates from mechanical vibrations (as picked up from the ground, for example) and drifts (e.g. induced by thermal effects) that affect the alignment of optical elements. In addition, direct thermal effects may further perturb the beam position. In particular, thermal lensing in the gain medium (e.g. a laser crystal) may be associated not only with a focusing action, but also with some beam deflection.

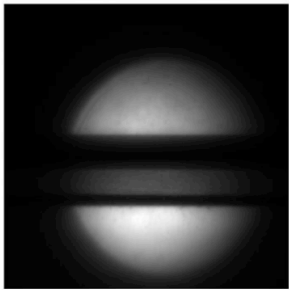
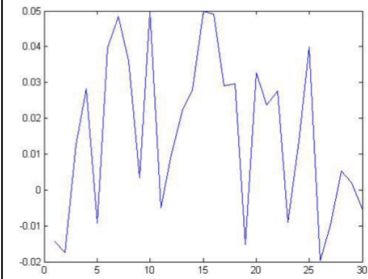
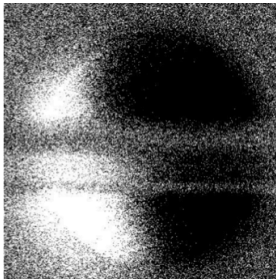
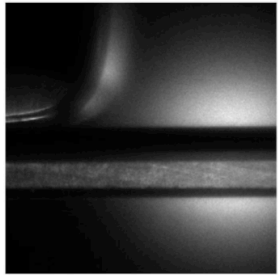
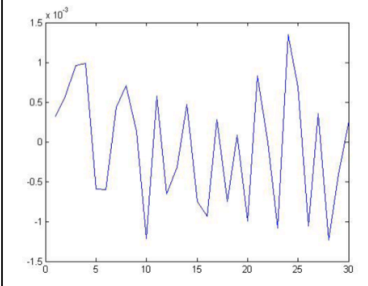
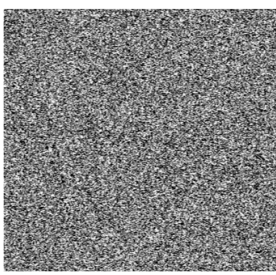
	Original picture	Dissymmetry-factor	Differential image
w/o fiber			
w/ fiber			

Table 3.2 Elimination of laser pointing instability by coupling the light source into a 2  $\mu\text{m}$  single-mode fiber. Left: images of laser pot on a homogenous dye solution. Middle: time-trace of 30 nominal dissymmetry factors within the light spot. The measurement was done by taken a movie of 60 frames under alternating left- and right-CPL illumination. Subtracting the images under left-CPL over under right-CPL generates 30 g-values. Right: maps of dissymmetry map, averaging images over the 30 pairs of left- and right-CPL illumination.

Cooling and/or softening mechanical vibrations of the laser may help alleviate the problem. Those however are difficult solutions. Instead, we coupled an optical fiber to the light source, in the hope of translating the angle instability to output power fluctuation. For a fiber of infinitesimal diameter, only normal incident beam may propagate through, where pointing instability is completely removed. In reality, one needs to compromise between output laser power and pointing noise by selecting core dimension of the optical fiber.

In the experiment, we adopted a single-mode fiber of 2  $\mu\text{m}$  core diameter. Table 3.2 shows the clear improvement of data quality by coupling the fiber to the laser head. With the fiber in place, mapping of the dissymmetry factor over a uniform sample was homogeneous. In contrast, apparent artifacts persisted with the laser alone. Attenuated laser power and additional intensity fluctuation may be compensated by more signal averaging and the special sample preparation, as suggested earlier in the section, respectively.

### **3.1.3 Linear Dichroism and linear birefringence of optical elements**

A chief pitfall in performing FDCD measurements in an optical microscope or macroscope is contamination of the signal by linear dichroism and linear birefringence, which is typically  $\sim 1000$  times larger than the CD signal. Even if one sends perfect CPL into the microscope, slight linear birefringence and linear dichroism in the internal components can lead to elliptically polarized light at the sample, and to a spurious signal

from linear dichroism. Therefore, compensation is needed to ensure an optimized CPL illumination on the sample.

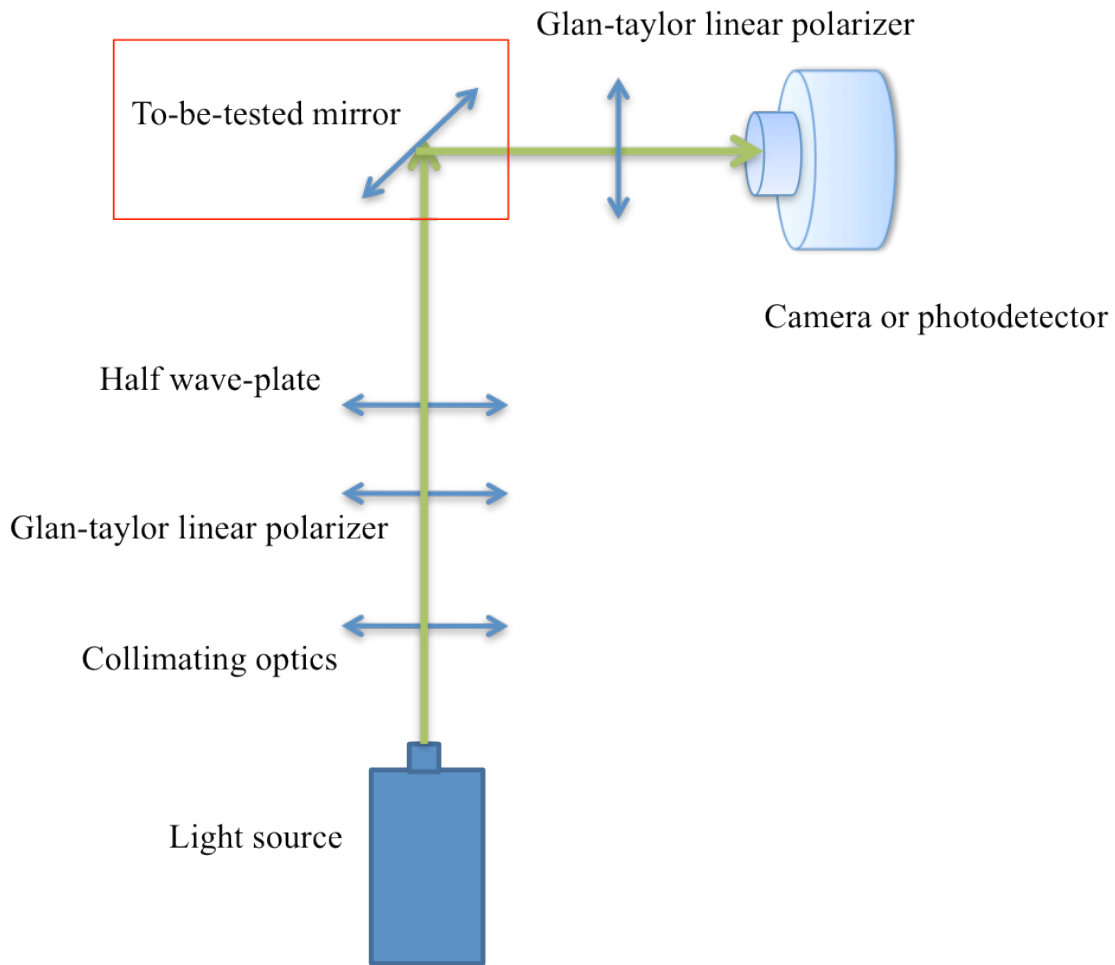


Figure 3.5 The experimental setup for calibrating linear dichroism and linear birefringence of an optical element.

In the experiment, we examined every optical element by assessing its Jones matrix, which is a 2-by-2 matrix that together with Jones vector of incident wave determines the polarization state of output light. Many methods are available to calibrate optics' Jones

matrices. Figure 3.5 illustrates one approach we adopted in calibrating the polarization property of a dielectric mirror, as enclosed in the rectangle. The first Glan-Taylor polarizer and the HWP are to assess its linear dichroism, while the analyzer after the mirror is to assess its linear birefringence. To create optimized CPL at the sample, we calculate the desired polarization state of input wave based on the measured Jones matrices and devise specific arrangement of optics to generate such a state of polarization. In section 3.3, I am to show the paramount importance of creating good CPL in performing chiroptical experiment.

### **3.2 Chiral fluorophores**

Several factors combined to dictate the choice of chiral molecule. **(a)** The regions of enhanced chiral selectivity were too thin to detect by direct differential absorption, so we sought a fluorescent compound with which we could detect differential induced fluorescence. **(b)** Many chiral molecules are fluorescent in the UV, but we sought a compound with visible excitation and emission due to the availability of better optics (LCVR in particular, which only operates in the visible and NIR) and more stable light sources in the visible. **(c)** The molecule are also needed to have a large value of  $g_{CPL}$  at a wavelength close to an available laser line, and is ideally photo-stable for a long period of experiment.

We were unable to locate commercially available molecules that are strongly chiral, fluorescent in the visible, and available in both enantiomers. Therefore, we acquired the chiral fluorophores by either running chemical synthesis ourselves or requesting samples

from peer chemists. Presented in the section are three types of small chiral fluorophores that we either synthesized or used for the chiroptical experiment. All compounds were characterized by  $^1\text{H}$  NMR,  $^{13}\text{C}$  NMR, mass spectrometry, adsorption and CD spectroscopy.

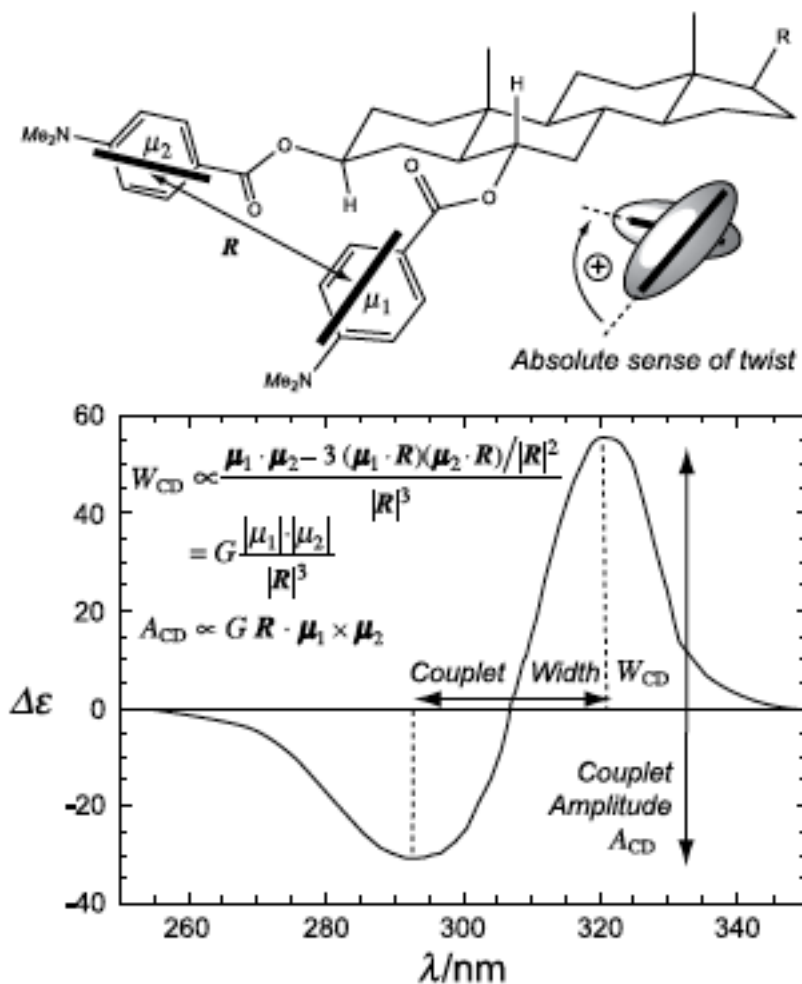


Figure 3.6 Exciton-coupled CD spectra of bis(4-dimethylaminobenzoate) of the chiral diol, 5-cholestan-3,6-diol. The two straight lines represent two electric dipoles (up), which couple to generate the exciton-split CD spectra (down). The figure is adapted from reference 123.

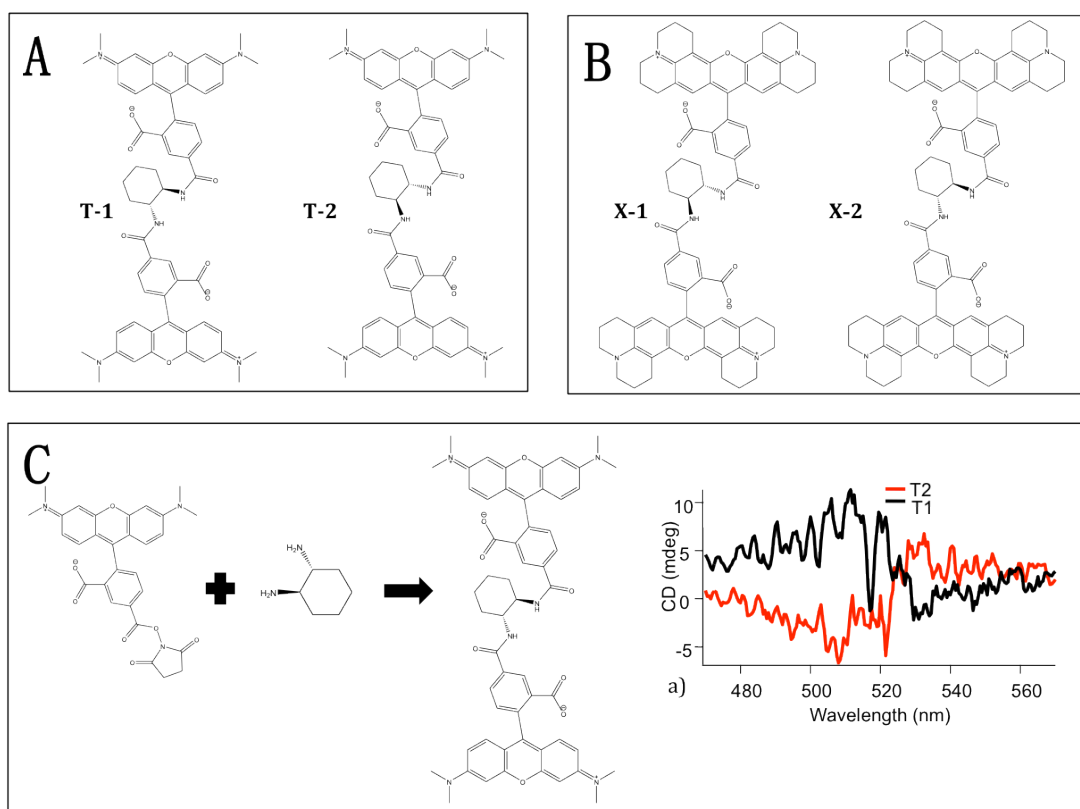


Figure 3.7 Diaminocyclohexane-based chiral fluorophores. (A) fluorescent reporter: 5/6-carboxytetra-methylrhodamine (TAMRA); (B) fluorescent reporter: 5-carboxy-X-rhodamine (XRD); (C) NHS-ester crosslinking reaction and the circular dichroism spectra of compound A.

### 3.2.1 Diaminocyclohexane-based fluorophores

We synthesized two pair of diaminocyclohexane-based fluorophores. Chirality in the molecules derives from the so-called “exciton coupling”.<sup>123</sup> Exciton coupling is when two chirally arranged and spatially close chromophores interact without perturbation from other factors. This results in an exciton-split CD spectrum, as shown in Figure 3.6. Using fluorophores as the two chosen chromophores, FDCD may be performed in addition to regular CD measurement. For all the molecules we synthesized, ( $\pm$ )-trans-1,2-Cyclohexanediamine was employed as the chiral backbone. We chose

commonly used fluorophores, 5/6-carboxytetra-methylrhodamine (TAMRA) and 5-carboxy-X-rhodamine (XRD), as the fluorescent reporters in the respective enantiomer pairs. (Figure 3.7 (A), (B)). We conjugated the fluorophores onto the chiral ligand through the NHS-ester crosslinking reaction.<sup>124</sup> (Figure 3.7 (C)).

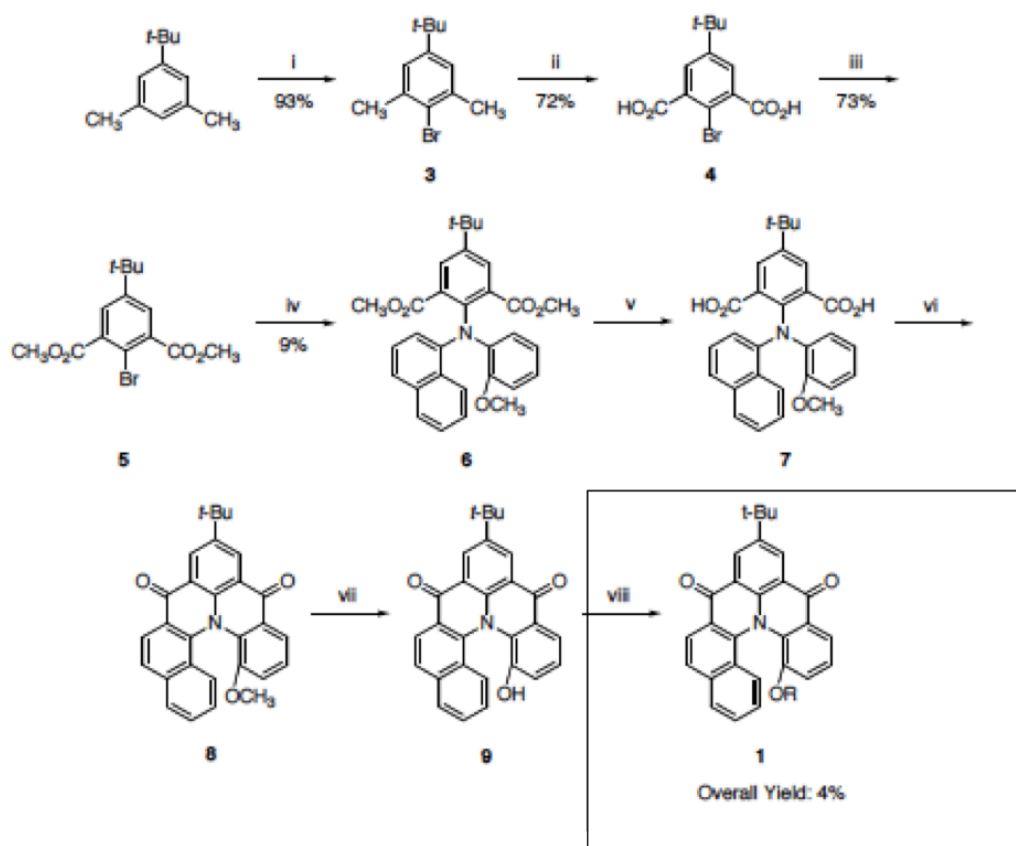
Unfortunately, CD spectrum taken on a CD spectrometer (J-710 JASCO) showed that the dissymmetry factor is only  $g_{CPL} = \pm 5 \times 10^{-5}$  at maximum for all the Diaminocyclohexane-based molecules we made. We deemed the number too exceedingly small to work with for ensuing experiment.

### 3.2.2 Bridged triarylamine helicenes

Heterohelicenes are inherently helical molecules that have exhibited several unique properties, one of which is their ability to absorb and emit CPL. A recent report<sup>121</sup> describes strong FDCD signals from bridged triarylamine helicenes. These molecules are not commercially available, and the published synthesis<sup>125</sup> is too involved to undertake in the lab. Fortunately one of my labmates, Jennifer Hou, told a friend of hers about our wish for these molecules, and the friend happened to be a TA for the undergraduate organic chemistry lab. Subsequently, Timothy Cook, James Liu and George Thampy run the chemical synthesis and obtained the desired enantiomeric pairs, M-2 and P-2. Figure 3.8 displays the key steps in the synthesis.

The camphanate group, as denoted by “R” in Figure 3.8, was used as a chiral resolving agent and rendered the two chiral species technically diastereomers. However, the

camphanate group had no detectable effect on the optical properties of either species. Circular dichroism spectrum of M-2 and P-2 was measured with a JASCO CD spectrometer. The CD spectra of the two compounds further confirmed the pair as “optical” enantiomers. As shown in Figure 3.9, dissymmetry factors are  $\pm 8 \times 10^{-3}$  at 355 nm excitation, a solid-state laser line.



<sup>a</sup> Reagents and conditions: (i)  $\text{Br}_2$ ,  $\text{Fe}^0$ , room temperature, 2h; (ii)  $\text{KMnO}_4$ ,  $\text{H}_2\text{O}/n\text{BuOH}$  (1:1) reflux for 18h and then  $\text{HCl}$ ; (iii)  $\text{MeOH}$ ,  $\text{H}_2\text{SO}_4$ , reflux for 18 h (iv) (2-Methoxy-phenyl)-naphthalen-1-yl-amine (**10**),  $\text{Cu}$ ,  $\text{CuI}$ ,  $\text{K}_2\text{CO}_3$ ,  $n\text{Bu}_2\text{O}$ ,  $120^\circ\text{C}$ , 96 h; (v)  $\text{NaOH}$ ,  $\text{H}_2\text{O}/\text{EtOH}$  (1:1), reflux for 22 h and then  $\text{HCl}$ ; (vi)  $\text{SOCl}_2$ ,  $\text{CH}_2\text{Cl}_2/\text{DMF}$  (cat.), reflux for 2 h, then  $\text{SnCl}_4$  and reflux for 18 h; (vii)  $\text{AcOH}/\text{HBr}$  (2:1), reflux for 72 h; (viii)  $\text{DMAP}$ , (1*S*)-camphanic chloride,  $\text{CH}_2\text{Cl}_2$ , reflux for 12 h.

Figure 3.8 Key steps in synthesizing bridged triarylamine helicenes. R is a camphanate group. The Figure is adapted from the lab report by Mr. James Liu at Harvard University.

### 3.2.3. Binaphthyl perylene derivative

Per the principle of exciton coupling as illustrated in section 3.2.1, binaphthyl perylene derivatives<sup>126</sup> exhibit strong circular dichroism in the visible. In the chiral molecules, binaphthyl unit acts as the chiral backbone, while two chirally arranged perylene derivatives are the fluorescent reporters. Figure 3.10 shows the molecular structures of the fluorophores used in the experiment. R indicates 1-hexylheptyl group, which was used to increase solubility of the chiral compound in organic solvent. Meanwhile, N,N'-bis(1-hexylheptyl)-perylene-3,4:9,10-bis-(dicarboximide) was employed as the

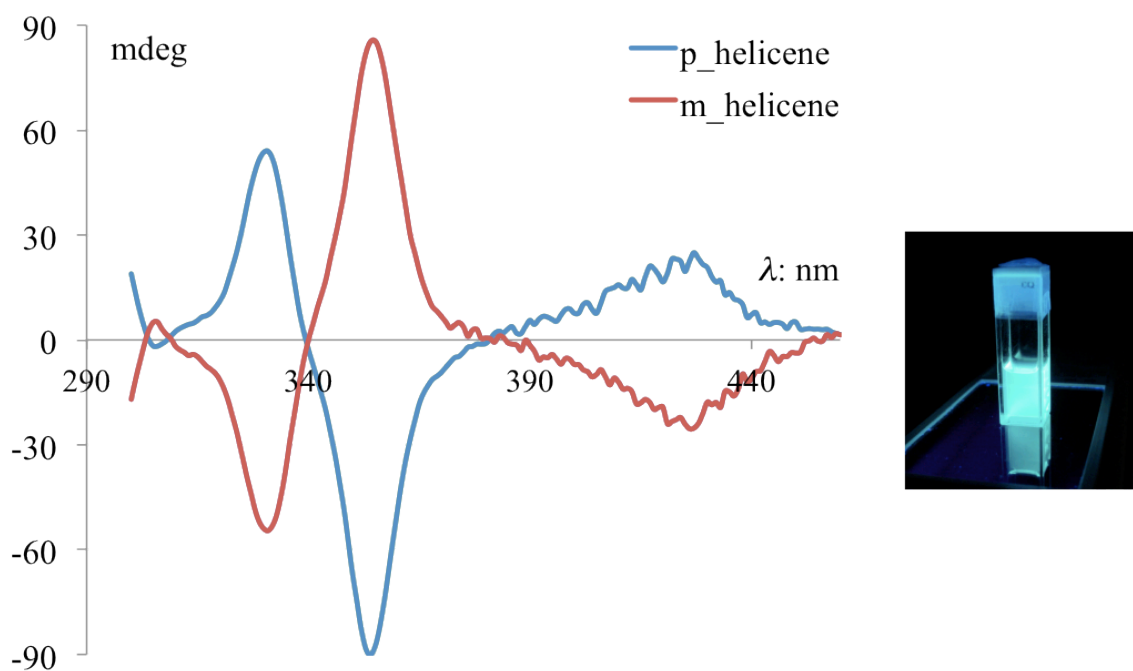


Figure 3.9 CD spectra of p- and m-triarylimine helicenes. Inset is a fluorescent image of helicene molecules under 355 nm excitation.

achiral reference, whose use will be elaborated in the next chapter. Figure 3.10 shows the CD spectrum in toluene of both enantiomers taken on a CD spectrometer (J-710 JASCO). A strong peak in the CD at 540 nm coincided closely to a He-Ne laser line at 543.5 nm,

while no detectable CD is identified for the achiral perylene.

Binaphthyl perylene derivatives are ideal candidates for the measurement, owing to their photo-stability, bright fluorescence and the strong CD band in the visible. We performed the experiment on demonstrating superchiral light with the chiral compounds, generously provided by Prof. Heinz Langhals at Ludwig Maximilians University Munich.

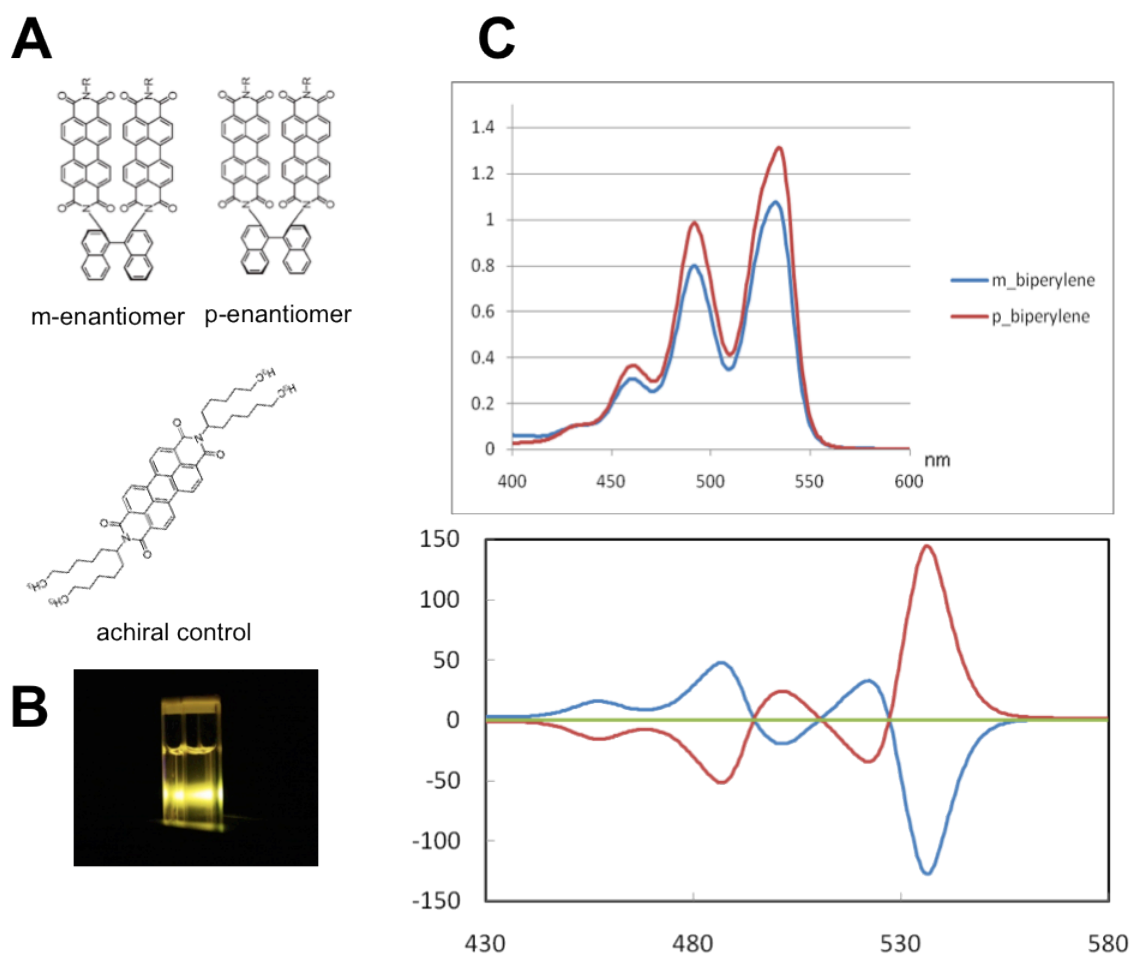


Figure 3.10 Binaphthyl perylene derives and achiral compound. A. Binaphthyl perylene dimer. R = 1-hexylheptyl group, for enhanced solubility. Achiral molecule: N,N'-bis(1-hexylheptyl)-perylene-3,4:9,10-bis-(dicarboximide); B. Photograph of a solution of the achiral perylene in toluene under 543.5 nm excitation; C. Absorption spectra (up) and CD spectra (down) of the chiral fluorophores and achiral control.

### 3.3 Pitfalls in chiroptical measurement

In the section, we present a case study on applying FDCD to study the optical activity of chiral fluorophores on a single-molecule level. In a report published in *Science* magazine, Hassey *et al.*<sup>121</sup> claimed to have observed vastly enhanced chiral asymmetry at single-molecule level. However as we carefully compensate linear dichroism and linear birefringence of optical elements, the dissymmetry factors of the single chiral fluorophores are found not to differ significantly from the bulk value of  $|g| < 10^{-4}$  at 457 nm. We will discuss how the artifacts are raised and may be eliminated.

#### 3.3.1. Single-molecule measurements on assessing molecular chirality

Single-molecule measurements have been used to probe the states and dynamics of a huge variety of biophysical and condensed matter systems,<sup>127</sup> and often yield information that is missed by bulk, ensemble-averaged techniques. In particular, measurements at ambient and low temperatures provide detailed information about the interactions between single fluorescent molecules and their local environment. The heterogeneously broadened lines visible in bulk often resolve into much narrower single-molecule lines, which show spectral diffusion,<sup>128</sup> blinking,<sup>129</sup> and polarization fluctuations<sup>130</sup> that indicate complex interactions with the host.

In principle, single-molecule spectroscopy may be employed to study chiroptical prosperities of molecules, which may reveal unexpected feature in the molecule-host matrix. Let's revisit the theory we presented in chapter 2, and identify if new phenomena may be derived on single molecule level from first principles. The Hamiltonian relevant to CD

for a chiral molecule in an electromagnetic field is:<sup>106</sup>

$$H = -\boldsymbol{\mu} \cdot \mathbf{E} - \boldsymbol{\theta} : \nabla \mathbf{E} - \mathbf{m} \cdot \mathbf{B},$$

where  $\boldsymbol{\mu}$  is the electric dipole operator,  $\boldsymbol{\theta}$  is the electric quadrupole operator, and  $\mathbf{m}$  is the magnetic dipole operator;  $\mathbf{E}$  is the electric field and  $\mathbf{B}$  is the magnetic field. The rate of excitation from an initial state  $i$  to a final state  $f$  involves the expression  $|\langle f | H | i \rangle|^2$ , as specified by Fermi's Golden Rule. This expression contains a term proportional to  $|\mu_{if}|^2$ , as well as cross-terms containing  $\boldsymbol{\mu}$  and  $\boldsymbol{\theta}$  or  $\boldsymbol{\mu}$  and  $\mathbf{m}$  (the remaining terms are small enough to be neglected). The term containing  $|\mu_{if}|^2$  represents electric dipole absorption, and is not sensitive to molecular chirality. The signs of the two cross-terms, however, depend on molecular chirality, so these terms are responsible for circular dichroism. Both cross terms depend on the orientation of the molecule relative to the incident field. Upon averaging over all molecular orientations, the electric quadrupole term averages to zero while the magnetic dipole term remains. Thus electric quadrupole transitions do not contribute to bulk CD, while magnetic dipole transitions do contribute.

Single-molecule FDCD might differ from bulk FDCD for several reasons:

- 1) Electric quadrupole and magnetic dipole matrix elements of orientationally fixed single molecules may differ from their rotationally averaged values in bulk systems;<sup>131</sup>
- 2) Local interactions with the host could modify the oscillator strengths or frequencies of the electric quadrupole or magnetic dipole transitions, to induce molecule-to-molecule variations in CD, i.e. heterogeneous broadening of CD lines.

The smallness of the electric quadrupole and magnetic dipole contributions to the Hamiltonian is purely geometrical in origin, a consequence of the small size of a molecule relative to the wavelength of light. Orientational averaging reduces the strength of the electric dipole/magnetic dipole interference by a factor of 3 relative to its peak value.<sup>106</sup> Electric quadrupole transitions average to zero in bulk, so bulk measurements provide no guidance on their magnitude. Geometrical considerations, however, indicate that the electric quadrupole term should be of the same order of magnitude as the magnetic dipole term. Density functional simulations of single helicene molecules support the prediction that single-molecule  $g$ -values are of the order of  $10^{-3}$ , of the same order as in bulk at the same excitation wavelength.<sup>132</sup>

### 3.3.2 Previous measurement and possible pitfalls

Theoretical models may be wrong, so there was considerable interest in the report from Hassey *et al.* that single molecules of bridged triarylamine helicenes show  $g$ -values ranging from +2 to -2, while in bulk the two enantiomers have  $|g| < 10^{-4}$  at the probe wavelength of 457 nm. Furthermore, they reported that both enantiomers of this compound show very similar broad distributions of single-molecule  $g$ -values, and that the wavelength dependence of the single-molecule  $g$ -values does not correspond to the bulk, even when averaged over many single molecules.<sup>132</sup>

We attempted to replicate the experiments of Hassey *et al.* and initially saw similar broad distributions of  $g$ -values. However, after correcting for the linear birefringence and linear dichroism inherent to the dichroic mirrors used in single-molecule FDCD

experiments, the distribution of  $g$ -values collapses to a sharp distribution around  $g = 0$ . The uncertainty in the measurements does not allow us to distinguish the  $g$ -values of opposite enantiomers.

### 3.3.3 Methods

We prepared the exact molecules as employed in Hassey's experiment. More information of the molecules may be found in section 3.2.2. The circular dichroism (Figure 3.9) and fluorescence (not shown) spectra are identical to earlier reports.<sup>125</sup> Both enantiomers show strong FDCD in bulk when excited with light at 355 nm, with  $g$ -values of  $+8.0 \times 10^{-3}$  for M-2 and  $-8.1 \times 10^{-3}$  for P-2. At 457 nm, the wavelength used in the experiments of Hassey *et al.*, the  $g$ -values are  $|g| < 10^{-4}$ .

Following the procedure of Hassey *et al.* we made solutions of the helicenes at  $10^{-8}$  molar in methanol and drop-cast these solutions onto a Zeonor film (ZF-14 ZEONEX/ZEONOR). A fused silica coverslip was cleaned in Piranha solution (3:1  $\text{H}_2\text{SO}_4$ :  $\text{H}_2\text{O}_2$ , Caution: highly corrosive). The Zeonor film was placed, helicene side down, onto the coverslip, and the samples were imaged in an inverted single-molecule fluorescence microscope.

The optical setup is shown in Figure 3.11(a). The setup is built around an Olympus IX71 inverted fluorescence microscope. The light source is a Melles Griot Argon-ion laser operating at 457 nm (0.4 mW at the sample). A narrow-band excitation filter (D457/10x Chroma) is used to remove plasma emission at other wavelengths. The light is polarized by a Glan Thompson polarizer (10GL08 Newport), passed through a liquid

crystal variable retarder (LCVR, LRC – 200 – VIS, Meadowlark Optics), and then through a quarter wave Fresnel rhomb retarder (FM600QM Thorlabs). The LCVR is driven with a 2 kHz square wave. An arbitrary state of ellipticity is generated by adjusting the LCVR drive voltage. We took care to avoid having any mirrors between the polarizer and the microscope, to avoid introducing spurious phase shifts onto the beam. The only reflection after the initial polarizer is off the dichroic mirror.

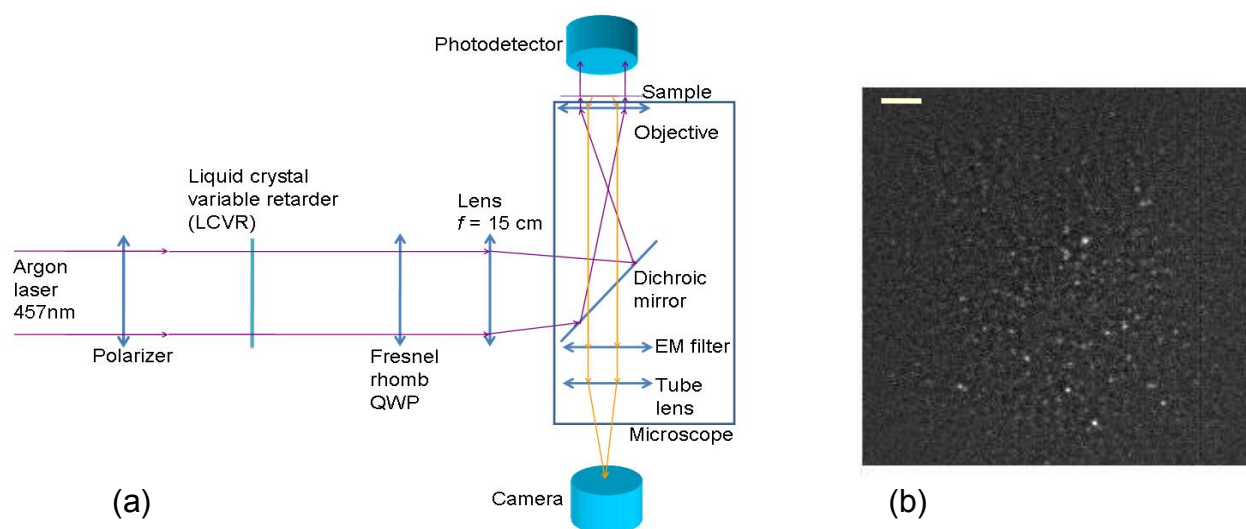


Figure 3.11. (a) Schematic diagram of optical setup for wide-field imaging. See text for detailed description. (b) Image of single helicene molecules. A diffuse background image was subtracted from the raw image to enhance the contrast of the single molecules.

A lens with a focal length of 15 cm (LA1433-A Thorlabs) brings the light to a focus at the back focal plane of the objective. After passing through the lens, the light is deflected upwards by a dichroic mirror. We performed experiments using either of two dichroics: DC1, 460 nm long pass; and DC2 (Olympus DM500), 500 nm long pass. Our objective

lens is a 60x, N. A. 1.45, oil immersion, plan apochromat (1-U2B616 Olympus). Fluorescence from the sample is collected by the same objective, passed through the dichroic mirror, and separated from the excitation light by a 470 nm long-pass emission filter (HQ470LP Chroma). Images are collected on an Andor iXon<sup>+</sup> electron-multiplying CCD (DU-897E-CS0-#BV), cooled to -50 °C.

A program written in LabView synchronizes the acquisition of images with the application of voltages to the LCVR. The LCVR has a ~30 ms response time to a change in the amplitude of its driving voltage, so each image acquisition starts 100 ms after a change in the voltage on the LCVR. In a typical experiment, 40 images are acquired, at 400 ms exposure per frame, with a switch in the polarization state between each frame. An amplified photodiode detector (PDA36A Thorlabs) is mounted on top of the microscope to monitor the intensity of the transmitted laser beam. This photodetector allows us to correct for laser power fluctuations.

Prior to each experiment, we measure the polarization state of the light entering the microscope and emerging from the objective. A polarizer (GL10 Thorlabs) is temporarily placed in the beam path at the point of measurement. The transmitted intensity is recorded using a power meter (FieldMaxII-TO Coherent Inc.) as a function of the angle of the polarizer.

Data are acquired under two conditions for each enantiomer: alternating left- and right-CPL sent into the microscope; and alternating left- and right-CPL at the sample plane. The analysis for all movies is completely automated using custom software written in

Matlab, with identical parameters for all data sets. Thus there is no possibility for bias in selecting molecules or extracting their intensities.

### 3.3.3 Experimental results and discussion

Figure 3.11(b) shows an image of single helicene molecules on the Zeonor film. We first imaged the molecules with alternating left- and right-CPL sent into the microscope. For both polarizations the ellipticity before the microscope is greater than 96%. Many molecules show strong asymmetries in their brightness, as shown in Figure 3b, leading to apparent  $g$ -values ranging from -2 to 2. However, we found that the light emerging from the microscope is not circularly polarized. Ellipticities are 36% for DC1 and 55% for DC2.

To generate CPL *at the sample* we measured the Jones matrices<sup>23</sup> for the dichroics. They are:  $\begin{pmatrix} 1 & 0 \\ 0 & 1.34e^{0.79i} \end{pmatrix}$  and  $\begin{pmatrix} 1 & 0 \\ 0 & 0.97e^{0.39i} \end{pmatrix}$ , for DC1 and DC2, respectively. We solved the matrix equations to identify the input polarization states which lead to CPL at the sample. These are:

$$\text{DC1: } \frac{1}{1.25} \begin{pmatrix} 1 & 1 \\ \pm 0.75e^{0.78i} & 1 \end{pmatrix} \quad \text{and} \quad \text{DC2: } \frac{1}{1.43} \begin{pmatrix} 1 & 1 \\ \pm 1.03e^{1.18i} & 1 \end{pmatrix}.$$

These polarizations are generated by applying appropriate voltages to the LCVR. Measurements confirmed ellipticities > 96% above the sample for both right- and left-CPL.

Figure 3.12(b) shows a histogram of  $g$ -values measured for single molecules with CPL before the microscope (using DC1) and with CPL at the sample (using DC2). The apparent  $g$ -values are broadly distributed in the case where the CPL is generated before the

microscope, using either DC2 (data not shown) or DC1. In contrast, with CPL at the sample, the  $g$ -values are not significantly different from zero:  $g = 0.026 \pm 0.27$  for M-2 and  $g = 0.033 \pm 0.29$  for P-2. The width of the observed distribution is largely due to statistical uncertainties in the extraction of single-molecule  $g$ -values in the presence of shot-noise and molecular blinking and photobleaching. Thus current experimental techniques cannot detect deviations from 0 in the  $g$ -values of single helicene molecules measured at 457 nm.

We conclude that the broad distribution of  $g$ -values observed by Hassey *et al.* can be explained by *linear dichroism*<sup>133</sup> in the randomly oriented helicene molecules, coupled with imperfect circular polarization of the illumination. We believe that such a mechanism is a more probable explanation for their data than is anomalously large circular dichroism at the single-molecule level, which would require a hitherto unknown physical effect. In addition to the dichroic mirrors discussed above, a third dichroic mirror with a cutoff of 570 nm (Olympus DM570) also showed strong linear birefringence for 532 nm light. We conclude that strong linear birefringence is a general feature of dichroic mirrors. Finding a dichroic with nearly equal reflectivities for  $s$ - and  $p$ -polarized light (such as our dichroic DC2) is not sufficient to preserve the polarization state of incident light; the phase shift between  $s$ - and  $p$ -polarizations is important too. An observation of CPL in light back-reflected from the sample is also not proof of CPL at the sample, because the back-reflected light has undergone a second phase-shifting reflection at the dichroic.

If CPL is sent into a fluorescence microscope, the dichroic mirror converts this light into elliptically polarized light at the sample, with different principal axes arising from the

two input circular polarizations. The linearly polarized component of this illumination leads to different rates of pure electric dipole excitation for each randomly oriented molecule. Many authors have documented the perils of performing microscopic CD measurements.<sup>134, 135</sup> Claborn and coworkers avoided any reflective elements in their optical train and so were not subject to this source of error.<sup>134</sup>

Circular dichroism measurements at the single-molecule level promise important information on molecular structure and local environmental interactions. However, uncompensated linear birefringence and linear dichroism in optical elements inside a microscope can cause linear dichroism to masquerade as circular dichroism. Caution is advised in performing and interpreting such experiments.

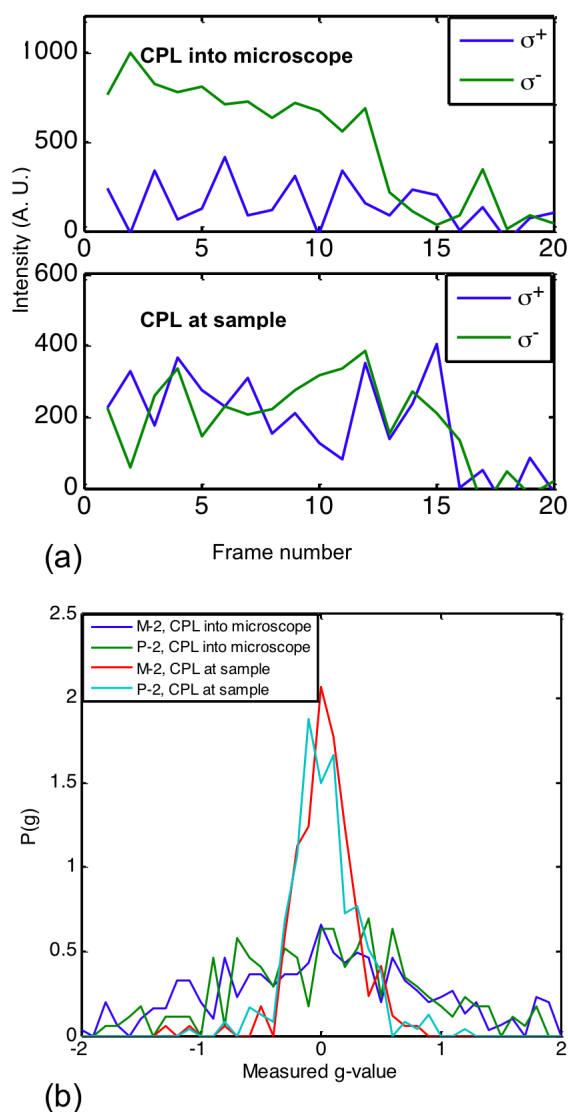


Figure 3.12 Fluorescence of single helicene molecules in CPL. (a) Time-traces of single helicene molecules with CPL sent into the microscope (top), and CPL generated at the sample plane (bottom). There is a large apparent  $g$ -value when CPL is sent into the microscope, but not when CPL is generated at the sample. Both molecules show single-step photobleaching. (b) Histogram of  $g$ -values for both enantiomers, under both polarization conditions. With CPL at the sample, the  $g$ -values are much more narrowly distributed. The number of molecules measured for each histogram are: M-2 CPL in: 303; P-2 CPL in: 173; M-2 CPL out: 169; P-2 CPL out: 234.

# Chapter 4

## On generating and observing superchiral light

Superchiral light is generated by employing a partial mirror that converts CPL of normal incidence to its opposite chirality. The incident and reflected waves interfere in space, and the enhancement in chiral excitation takes place at the nodes of the superchiral standing waves. In the preceding chapters, we introduced theories behind the predicted enhancement and issues on the selection of material and optics. In this chapter, we account details of experimental procedure in generating and observing the superchiral electromagnetic modes.

The chapter is organized as such: We first elaborate experimental arrangement on imaging chiral excitation through fluorescence detected circular dichroism (FDCD) measurement. We then introduce a few approaches to put the chiral molecules precisely at the superchiral nodes. Lastly, we discuss the experimental results.

### 4.1 Overview of the FDCD measurement

Fluorescence is the emission of light by a substance that has absorbed light or other electromagnetic radiation. Oftentimes, the emitted light has longer wavelength than the incident wave, owing to a non-radiative vibrational relaxation at the excited states. Due to the wavelength shift of fluorescent emission, an emission filter may be employed to remove

the scattered incident light. Therefore, fluorescence measurement gains fame for its extreme sensitivity in assessing molecular excitation.

In the linear regime, fluorescence intensity is proportional to the absorption rate. Thus FDCD was proposed as an alternative to absorption CD spectroscopy in assessing chiral asymmetry. Strictly speaking, FDCD and CD do not generate equivalent results, given a finite sample thickness. Let  $\varepsilon_R$  and  $\varepsilon_L$  be the molar absorptivity under right- and left-CPL illumination,  $L$  be the thickness of the sample, and  $C$  be the molar concentration.

Per the Beer's law, the dissymmetry factor in CD measurement is:

$$g_{\text{Abs}} = \frac{2\left((1-e^{-\varepsilon_R LC}) - (1-e^{-\varepsilon_L LC})\right)}{(1-e^{-\varepsilon_R LC}) + (1-e^{-\varepsilon_L LC})}. \quad (4.1)$$

And FDCD results in the dissymmetry factor:

$$g_{\text{FDCD}} = \frac{2\left(\int_0^L (1-e^{-\varepsilon_R l C}) dl - \int_0^L (1-e^{-\varepsilon_L l C}) dl\right)}{\int_0^L (1-e^{-\varepsilon_R l C}) dl + \int_0^L (1-e^{-\varepsilon_L l C}) dl}. \quad (4.2)$$

Equations (4.1) and (4.2) differ at any finite  $L$ . However at the limit  $L \rightarrow 0$ , the two dissymmetry factors coincide:

$$g_{\text{Abs}} = g_{\text{FDCD}} = \frac{2(\varepsilon_R - \varepsilon_L)}{\varepsilon_R + \varepsilon_L}. \quad (4.3)$$

We note that the discrepancy is insignificant in our experiment for the following reasons: (1) in the imaging experiment, only a thin layer of sample is in focus. Therefore, the effective sample thickness,  $L$ , is restricted; (2) in the superchiral experiment, the film thickness is only about 10 nm. This is very close to the limit that generates the same results for the two approaches.

In conventional CD spectroscopy, incident light is modulated between left- and

right-polarization at high frequency, and a lock-in amplifier is subsequently employed to record transmitted intensity after a chiral sample. Following the principle, we devised a PEM-based polarimetry to perform FDCD measurement on bridged triarylamine helicenes.

As shown in Figure 4.1, helicene molecules were dissolved in toluene solution, and held by a quartz cuvette. The setup consists of mercury arc lamp filtered to provide illumination at 355 nm, a polarizer and a PEM (PEM 100 HINDS) to create alternately left- and right-CPL at 50 KHz, and a highly sensitive photodiode (PDA36A Thorlabs) to record the fluorescence emission. The averaged fluorescence reads as 4.5 mV at the photodiode, while the differential fluorescence is  $\pm 33 \mu\text{V}$  for the respective enantiomers. Dissymmetry factor  $g_{\text{FDCD}}$  is determined to be  $\pm 33 \times 10^{-3} / 4.5 = \pm 7.3 \times 10^{-3}$  for the respective enantiomers, which are very close to  $g_{\text{Abs}} = \pm 8.0 \times 10^{-3}$  by a JASCO CD spectrometer.

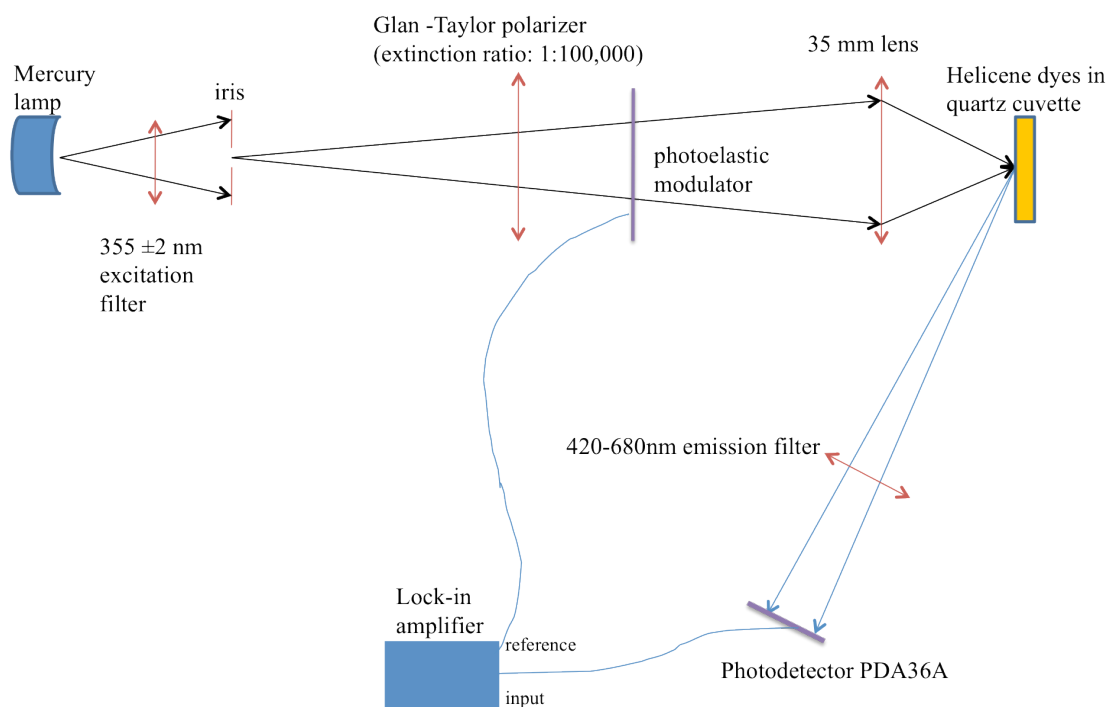


Figure 4.1 The experimental setup for PEM-based FDCD measurement

In chapter 3, we argued the necessity of performing FDCD measurement on observing the superchiral enhancement. We propose using an achiral reference to correct experimental artifacts, which include: (1) power fluctuation (1 ~ 2%) of light source; (2) photo-bleaching of chiral fluorophores, which leads to a constant bias in evaluating dissymmetry factors;<sup>ii</sup> (3) imperfection of the polarization optics. For compensating the photobleaching-induced bias, the achiral molecules are either racemic mixture of chiral enantiomers or of very similar molecular structure to its chiral counterpart (for example, if the chiral compounds are too precious to mix up).<sup>iii</sup> In experiment the achiral and chiral molecules are put next to each other in space, ensuring a simultaneous illumination by the incident light. As switching between illumination of opposite chirality, any changes in the fluorescence intensity in the achiral molecules can be used to perform a background correction to the signal from the chiral molecules.

#### 4.1.1 Sideways FDCD in liquid

As a preliminary proof-of-principle we imaged the CD of biperylene derivatives using fluorescence (without any superchiral enhancement). To our knowledge, this experiment is the first demonstration of fluorescence detected circular dichroism *imaging*. As shown in Figure 4.2, our camera-based FDCD setup consists of a HeNe laser, coupled to a narrow-band excitation filter to provide illumination at 543.5 nm, a polarizer and a LCVR

---

<sup>ii</sup> Photo-bleaching leads to a decrease in fluorescence intensity over time. Under current scheme where input helicity alternates, differential fluorescence may be nonzero even with the same excitation rate of left- and right-CPL illumination.

<sup>iii</sup> For triarylamine helienes, we use racemic mixture as the achiral reference. For biperylene derivatives, the achiral counterpart is N,N'-bis(1-hexylheptyl)-perylene-3,4:9,10-bis-(dicarboximide), which has very similar structure to the chiral compounds.

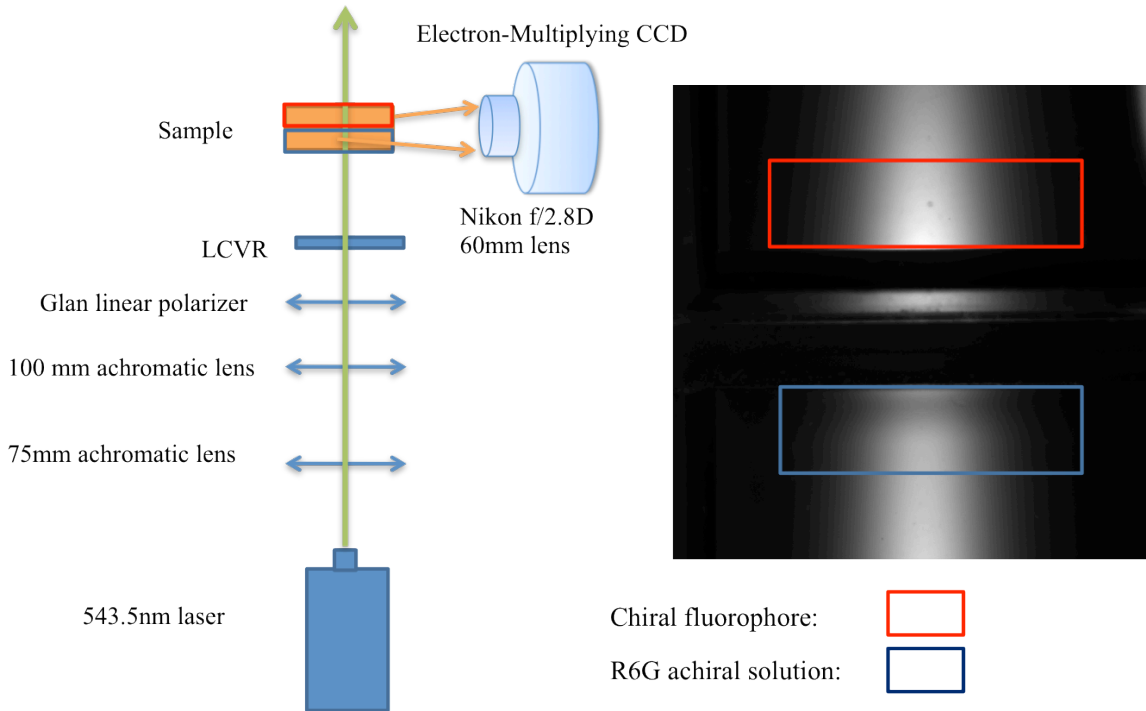


Figure 4.2 Left: the Experimental setup for sideways FDCD measurement; (B) a photo of two cuvettes, the up is filled with binaphthyl perylene dimers, and the lower is filled with achiral control molecules

(liquid crystal variable retarder) to create alternately left- and right-CPL at the sample, and a high-sensitivity Electron-Multiplying CCD (Andor iXon<sup>+</sup>) to record the images. One cuvette was filled with a solution of single enantiomer, and a second cuvette was filled with achiral compound. The two cuvettes were put in series along the beam path. The EMCCD was set on the side at 90° to monitor fluorescence from the two samples under left/right-polarized illumination.

For each frame taken by the camera, we normalized the image by the total intensity of the achiral region. We calculated a map of the dissymmetry factor by

$$g_{image} = 2 \frac{(F_L - F_R)}{(F_L + F_R)}$$

where  $F_L$  and  $F_R$  are the normalized images under left- and right-CPL illumination, averaging over the complete dataset. The map should reflect the spatial distribution of chiral excitation in the field of view. Figure 4.3 shows the result. The maps of the dissymmetry factor show the p-enantiomer as brighter than the achiral control, while the m-enantiomer is dimmer. Quantitatively, p-enantiomer has a dissymmetry factor of  $(2.35 \pm 0.42) \times 10^{-3}$ , and m-enantiomer  $-(2.12 \pm 0.36) \times 10^{-3}$ . Inhomogeneity in the map of dissymmetry factor may originate from oblique incidence of CPL and absorption of light in the sample.

#### 4.1.2 Facial FDCD in solid thin film

Following the same principle, we devised the experiment for performing facial FDCD measurement on a solid thin film. (Figure 4.4) The distinct differences from sideways experiment include: (1) a single mode fiber was coupled to the light source, to eliminate the pointing instability of laser beam; (2) LCVR was put after the mirror, to ensure optimized CPL on the sample. In such an arrangement, linear polarized light was sent along the respective edge of the mirror, and the polarization state of reflected beam may be preserved. LCVR simply acted as a wave plate alternating between 1/4- and 3/4-wave retardance. Fluorescence from the molecules is largely unpolarized, so that its intensity may not be modulated by the LCVR; (3) chiral molecules were embedded in an amorphous polymer matrix, instead of liquid.

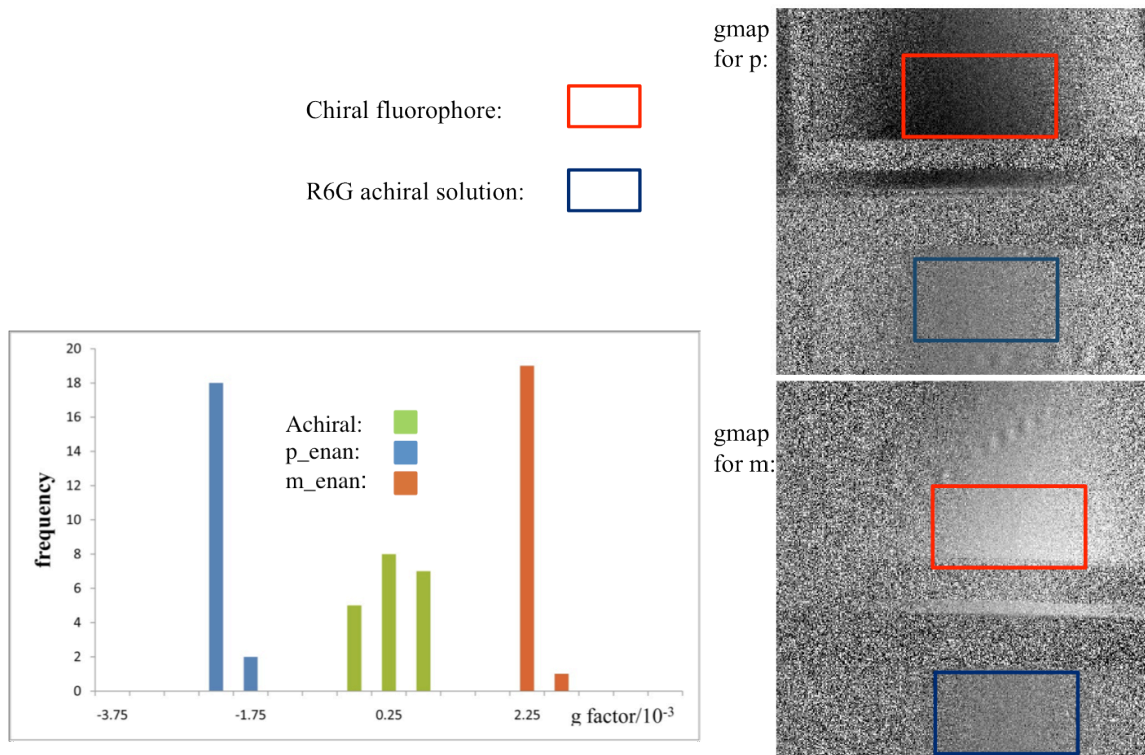


Figure 4.3 Sideways FDCD. Left: map of dissymmetry factor for the p-enantiomer and achiral control (up); map of dissymmetry factor for the m-enantiomer and achiral control (down). Right: Histogram of  $g$  factor based on 40 images (for both the m- and p-enantiomer)

We determined the dissymmetry factors under conventional circularly polarized light to be  $g_{CPL} = (1.41 \pm 0.03) \times 10^{-3}$  (for  $p$ ) and  $g_{CPL} = -(1.42 \pm 0.04) \times 10^{-3}$  (for  $m$ ), as shown in Figure 4.5. The apparent discrepancy between the dissymmetry factor of molecules in solid and liquid might originate from different types of interaction between chiral molecules and organic hosts (In liquid, the host is toluene; while in solid, it is PMMA)

The exact setup was employed for the superchiral experiment. (Figure 4.4(b))

## 4.2 Preparing samples for generating superchiral light

The goal was to position a chiral film of thickness much less than the wavelength of light in a standing wave generated by reflection of CPL off an imperfect mirror. The film had to be positioned with extreme stability relative to the mirror so that drift of the

interference fringes did not overwhelm the small changes in total fluorescence due to CD. The fractional changes in fluorescence in conventional CD are expected to be of order  $\sim 10^{-3}$ , implying that the separation of the film and the mirror had to be stable to  $\lambda/10^4 \approx 0.5 \text{ \AA}$  during a 20-minute data acquisition.

In the section, I will introduce three generations of sample structures for generating the superchiral light. By the end, we adopted generation III for a successful experiment.

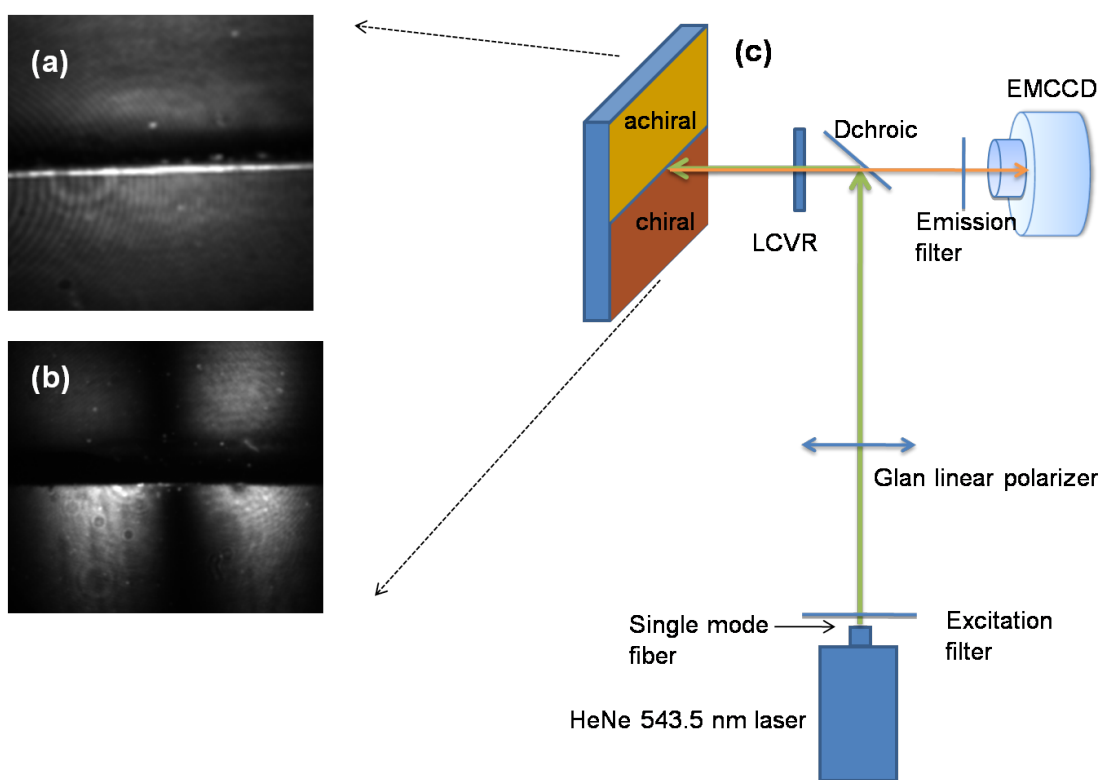


Figure 4.4 Measurement apparatus for facial FDCD (a) Photograph of fluorescent sample without (b) Photograph of fluorescent sample with Al mirror and a vertical interference stripe. (c) Experimental layout

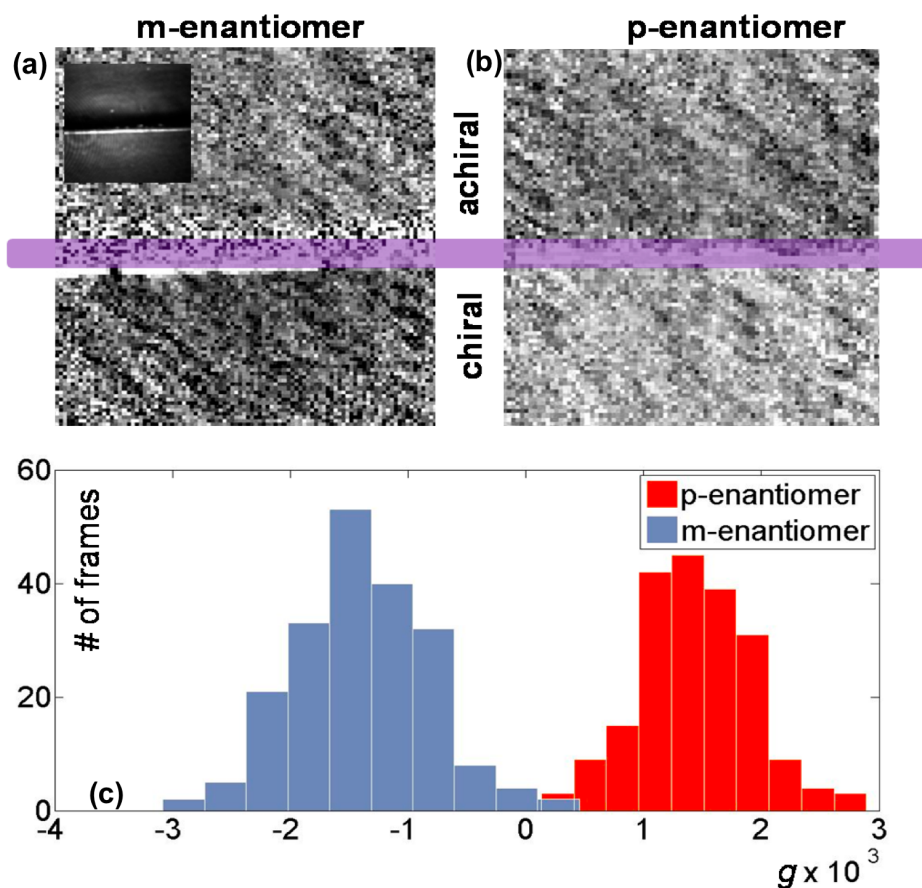


Figure 4.5. Fluorescence detected circular dichroism without superchiral enhancement. (a) Map of dissymmetry factor for the m-enantiomer and achiral control. Inset: photo of the fluorescent image. (b) Map of dissymmetry factor for the p-enantiomer and achiral control. (c) Histogram of  $g$  factor based on 400 images (for both the m- and p-enantiomer)

#### 4.2.1 Generation I: Nano-staircases

We created nanostructures consisting of a staircase of a transparent dielectric ( $\text{SiO}_2$  or  $\text{Si}_3\text{N}_4$ ) sitting atop a high quality reflector (Ag or Al), backed by a Si wafer (Figure 4.6). The top of the staircase was coated with a monolayer of chiral fluorophores. When illuminated at normal incidence with monochromatic light, the nanostructure generated a

standing wave, with molecules on different steps experiencing different relative electric and magnetic field intensities. A detailed discussion of the electrodynamics of such a structure (considering only the electric field) was given by Lambacher and Fromherz.<sup>136</sup> Similar structures (without the metallic reflector underneath) have been made for fluorescence interference microscopy, and used to measure the z-coordinate of fluorophores with great precision.<sup>137</sup>

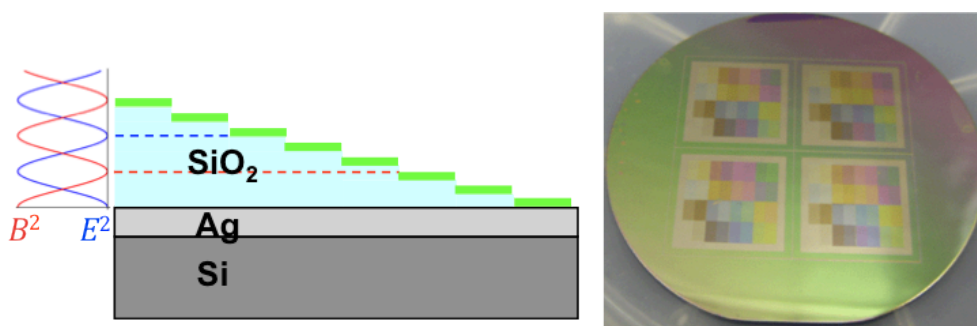


Figure 4.6 Staircase nanostructures for probing superchiral light. Left: The schematic of the structure showing transparent steps of SiO<sub>2</sub> on a reflective backing. When illuminated with monochromatic light at normal incidence, some steps will reside in a node of either the electric field or the magnetic field. Right: Photograph of a device we made with 64 steps.

We fabricated staircase nanostructures using standard techniques of nanofabrication. In brief, a silicon wafer was coated with a thin layer of a reflective metal, typically aluminum or silver, by thermal evaporation. Photolithography was used to mask a region of the surface, and a layer of SiO<sub>2</sub> was deposited on the exposed region via chemical vapor deposition (CVD). The photoresist was then removed, followed by another round of photolithography and CVD. By using the photolithographic patterning scheme developed by Ajo-Franklin et al.<sup>138</sup> we generated a staircase of  $2n$  steps in  $n$  rounds of

photolithography and CVD. Figure 4.6 shows some staircases of 64 steps, made with 6 rounds of processing. The step height was 50 nm. The colors resulted from thin-film interference from the differing step-heights.

We didn't pursue the approach for long, due to complexity of the nanofabrication being involved. Instead, a simple tilted mirror was employed to generate the superchiral configuration.

#### **4.2.2. Generation II: Micro-printing**

In this generation, the spatial arrangement of chiral and achiral species was achieved by micropatterning scheme, as shown in Figure 4.7. The idea was to use microcontact printing<sup>139</sup> to lay down alternating lines of chiral and achiral fluorophores. We made microfabricated PDMS stamps which we used to print alternating lines of chiral and achiral molecules. Figure 4.8 shows the result of this stamping procedure.

The superchiral standing wave was generated by reflecting CPL off an imperfect mirror mounted just above the patterned coverslip (Fig. 4.8). We mounted the coverslip at a slight angle relative to the mirror, so that a single image of the coverslip recorded fluorophores at a range of  $z$ -coordinates along the standing wave. The vertical stripes in Fig. 4.8 (c) were due to the standing wave from the mirror.

The problems with the micropatterning scheme are: (1) the mirror is on a separate piece from the coverslip with chiral molecules. Mechanical stability becomes a concern in the measurement; (2) we examined the stripes by a single micropatterning step under AFM (atomic force microscopy). As can be seen in Figure 4.7(i), particles lay in between of the

patterned stripes. Cross-contamination between chiral and achiral molecules might take place; (3) molecules aggregated during the transfer step. The aggregations appeared as extremely bright spots under a fluorescent microscope, which restricted the observation on other parts of the sample.

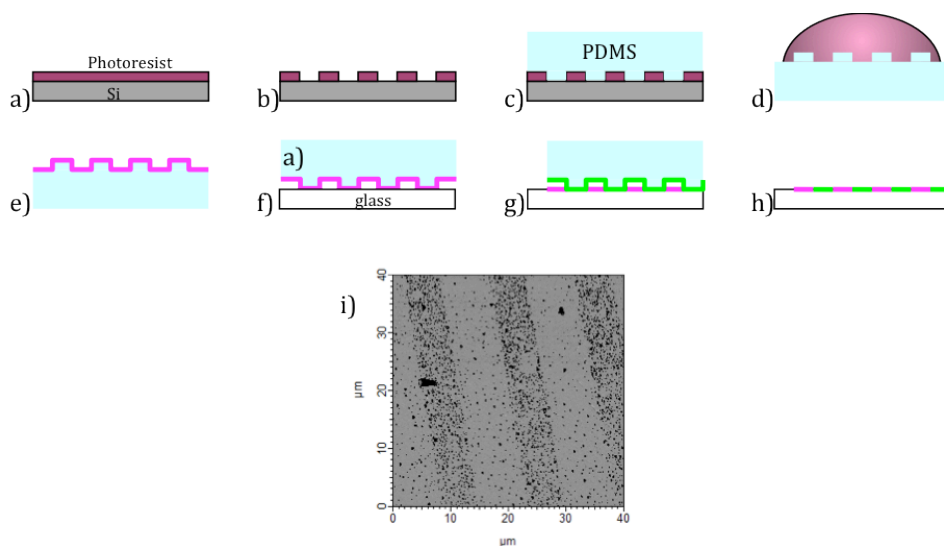


Figure 4.7 Microfabrication of alternating stripes of chiral and achiral fluorophores. a) – c) formation of a poly(dimethyl siloxane) (PDMS) stamp by conventional photolithography followed by casting of PDMS; d) – e) inking of the stamp with a solution of chiral fluorophores; f) transferring the pattern to a substrate via microcontact printing; g) – h) repeating the process with achiral fluorophores. i) AFM image of the patterned fluorophores

The first two generations were both designed to offer structures compatible with the use of a microscope. Fabricating devices of such small features was an avoidable challenge, as we realized later. The optics is capable of generating polarization state of enable observation over mm scale.

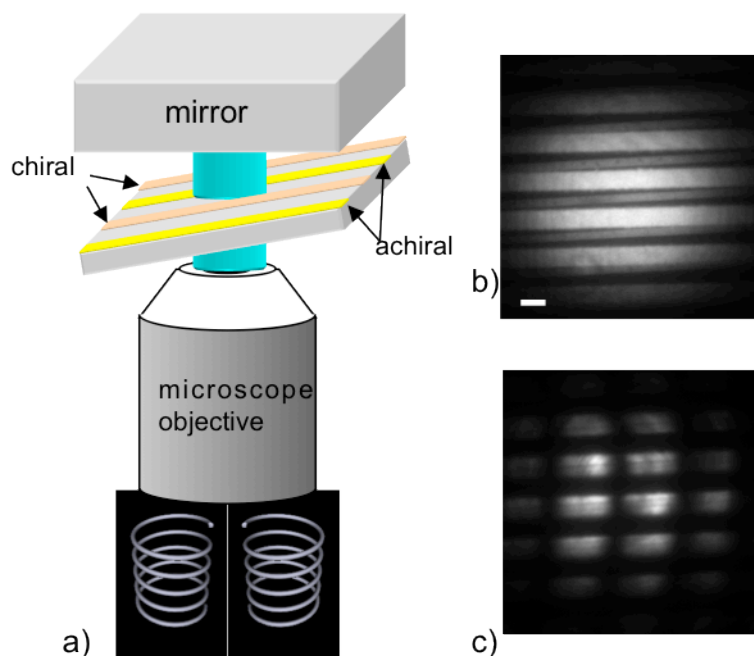


Figure 4.8 a) Illumination scheme for detecting enantioselective excitation in a superchiral standing wave. Left- and right-CPL are alternately introduced into the microscope. A mirror mounted above the sample reflects the light to generate a superchiral standing wave. A coverslip patterned with chiral and achiral molecules is introduced at an angle relative to the mirror. b) Fluorescence image without the top mirror, showing alternating chiral and achiral stripes (the chiral and achiral stripes are different widths so we can distinguish them). Scale bar 10  $\mu\text{m}$ . c) Fluorescence image with the top mirror, showing an optical standing wave (vertical stripes) superimposed on the patterned molecules (horizontal stripes).

#### 4.2.3. Generation III: Nanometer-scale sandwich geometry

In the latest generation, we deposited thin films of achiral and chiral molecules and the mirror on opposite sides of a 150  $\mu\text{m}$ -thick glass coverslip. The aims were to achieve both mechanical stability and superchiral mode generation at a macroscopic length scale.

Figure 4.9 shows the sample preparation. A box of #1.5 coverslips (VWR) was searched for coverslips that showed straight, well-spaced interference fringes when viewed under fluorescent room lights. A favorable coverslip was cleaned and coated on one side

with 19 nm of Al via thermal evaporation. This mirror had a reflectivity of 72% at 543 nm. The Al-coated side of the coverslip was then bonded to a 1 mm thick glass slide using optical adhesive (Norland 68). The glass slide protected the Al film and provided a rigid support for the coverslip.

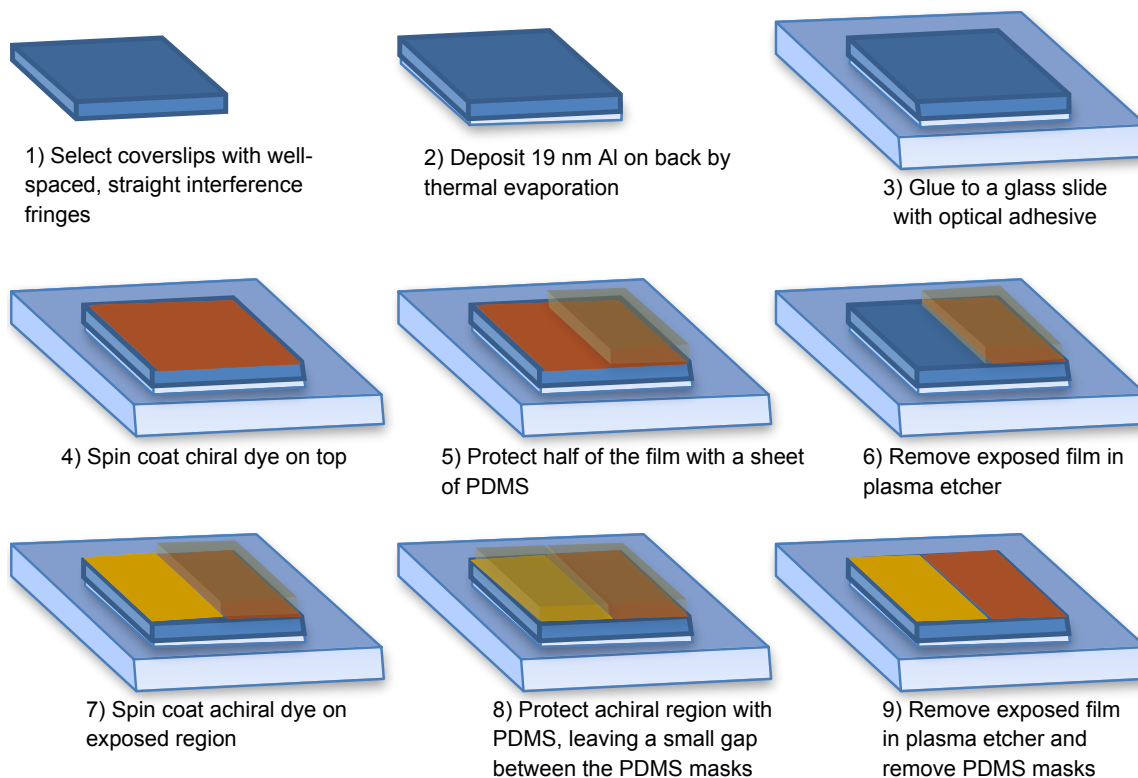


Figure 4.9 Procedure for preparing the nanometer-scale sandwich geometry

Chiral fluorophores ( $2 \times 10^{-4}$  M) and poly(methyl methacrylate) (PMMA, molecular weight 350,000, 0.75%) were dissolved in toluene. A chiral film was deposited by spin coating the solution onto the exposed face of the coverslip (60 s at 2800 rpm). The film thickness was determined to be 10 nm by ellipsometry. We then covered half of the film with a piece of polydimethylsiloxane (PDMS), which served as an etch mask for the next step. The exposed film was removed in a plasma etcher (500 mTorr, 5 min. SPI Plasma

Prep II), while the part covered by the PDMS remained on the coverslip.

Leaving the PDMS over the chiral film, we spin coated a solution of the achiral control ( $2 \times 10^{-4} \text{ M}^{\text{iv}}$  with 0.75% PMMA in toluene, 60 s at 2800 rpm) onto the exposed part of the coverslip. We then masked the achiral region with a second piece of PDMS, leaving a thin gap between the two pieces of PDMS. This assembly was subjected to a second round of plasma etching, to remove a thin trench of polymer separating the chiral and achiral regions. The PDMS masks were then removed. A second sample was prepared as above, using the opposite enantiomer. This procedure led to two samples in which achiral and chiral thin layers each occupied half of the coverslip, with a small gap in between.

### 4.3 Results and discussion

The optical setup is shown in Figure 4.10. This system was designed to be immune to laser pointing instability and intensity fluctuations, while permitting measurements of fluorescence intensity under well-defined polarization conditions to a fractional precision of  $4 \times 10^{-5}$ .

---

<sup>iv</sup> The choice of concentration is a compromise between ensuring abundant fluorescence under excitation and avoiding self-quenching when intermolecular spacing becomes unduly small.

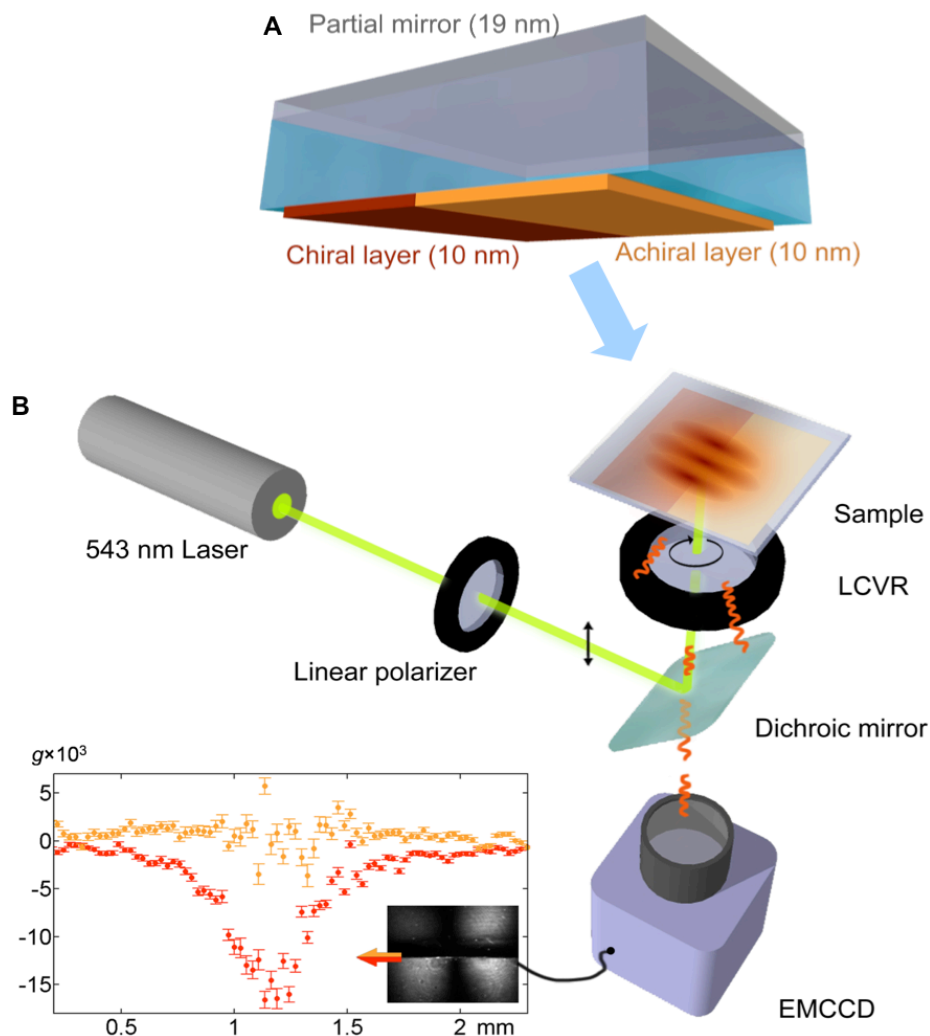


Figure 4.10. (A) Nanofabricated structure for positioning a chiral fluorescent film with extreme stability relative to a partially reflecting mirror. The achiral fluorescent film served as a built-in control. The glass coverslip separating the chiral film from the mirror was  $170 \mu\text{m}$  thick. (B) Apparatus for generating and detecting superchiral light. Light impinging on the dichroic mirror was purely  $p$ -polarized to avoid distortion from birefringence in the dichroic mirror.<sup>122</sup> The liquid crystal variable retarder (LCVR) converted the linearly polarized light alternately into left- and right-circularly polarized light. Fluorescence was separated from excitation light by the dichroic mirror and an emission filter (not shown), and imaged on an electron-multiplying CCD camera (EMCCD).

The light source was a HeNe laser operating at 543.5 nm (JDS1674P, power: 0.9 mW). A narrow-band excitation filter (Z543/10X Chroma) removed plasma emission at other wavelengths. The beam was coupled through a single mode optical fiber to eliminate pointing instability. The beam was then expanded to a diameter of 7.8 mm and polarized by a Glan-Taylor polarizer (GL10-A Thorlabs). The principal axis of linear polarization was chosen to be vertical, to minimize distortion of the polarization upon reflection on the dichroic mirror (Z543RDC Chroma). After the dichroic, the light passed through a liquid crystal variable retarder (LCVR, LRC - 200 - VIS, Meadowlark Optics). The LCVR was driven with a 2 kHz square wave with amplitude selected to generate the desired circular polarization incident on the sample. The LCVR was mounted on a linear motion stage (MT1-Z8 Thorlabs) which could translate its position perpendicular to the beam. This motion was essential to average out subtle interference fringes due to imperfections in the LCVR that otherwise contaminated the data analysis.

The sample was aligned perpendicular to the beam, with illumination falling equally on the chiral and achiral regions. Fluorescence passed back through the LCVR and the dichroic mirror. An emission filter (HQ565lp Chroma) passed fluorescence while blocking scattered laser light. A Nikon macro-lens (60 mm f/2.8D AF Micro-Nikkor) imaged fluorescence from the sample onto an Andor iXon+ electron-multiplying CCD (DU-897E-CS0-UVB), cooled to -70 °C.

A program written in LabView synchronized acquisition of images with application of voltages to the LCVR. The LCVR had a 30 ms response time to a change in the amplitude

of its driving voltage, so we waited 100 *ms* before acquiring an image. Full field images (512 x 512 pixels) were acquired with an exposure time of 0.8 s and an EM gain of 5. For each sample, 400 images were acquired with a switch in the chirality of CPL between each frame. Every 40 frames the lateral position of the LCVR was shifted by 0.2 mm using the motorized translation stage.

The LCVR and glass produced autofluorescence that led to a spatially inhomogeneous background signal. To correct for this autofluorescence, we prepared a sample lacking fluorophores and repeated the experiment, acquiring another 400-images alternately under left- and right-CPL. We averaged the left-CPL and right-CPL background images separately. Each average image was subtracted from the images with a fluorescent film taken under corresponding helicity of the illumination.

To compensate for residual differences in the fluorescence between left- and right-CPL that were not due to CD, a scaling factor  $Q$  was applied to the background images to eliminate an apparent dissymmetry in the achiral control regions. These scaling factors were: Figure 4.5,  $Q_R = 1$ ,  $Q_L = 1.013$  for both enantiomers; for Figure 4.11,  $Q_R = 1$ ,  $Q_L = 1.012$  for the m-enantiomer, and  $Q_R = 1$ ,  $Q_L = 1.008$  for p-enantiomer.

The reflectivity,  $R$ , of this film determined the degree of chiral enhancement at the superchiral nodes according to:

$$g = g_{CPL} \frac{1 + \sqrt{R}}{1 - \sqrt{R}} .$$

The electric energy density at the node, which determined the total fluorescence brightness was

$$U_e = U_{e,CPL} (1 - \sqrt{R})^2$$

where  $U_{e,CPL}$  is the electric component of the energy density of the incident circularly polarized plane wave. Higher reflectivity led to larger chiral selectivity, but at the expense of a smaller electric energy density at the node, and hence a smaller overall fluorescence intensity at the node.

Figure 4.11 (A) shows plots of the average fluorescence intensity as a function of position in the superchiral standing wave and Fig. 4.11 (B) shows plots of the dissymmetry factor along a line cutting through a superchiral node. The superchiral nodes were located by their correspondence with a minimum in the average fluorescence intensity. The maximum dissymmetry factors were  $g = (1.50 \pm 0.08) \times 10^{-2}$  and  $g = -(1.65 \pm 0.08) \times 10^{-2}$  for the *p*- and *m*-enantiomers, respectively. The achiral control samples had  $g \approx 0$  throughout the standing wave.

To determine the degree of superchiral enhancement, the experiments were repeated using conventional circularly polarized light. As we described in section 4.1.2, Samples were prepared identically to above, except that the partially reflecting mirror was omitted so that no standing wave was generated. The dissymmetry factors under conventional circularly polarized light were  $g_{CPL} = (1.41 \pm 0.03) \times 10^{-3}$  (for *p*) and  $g_{CPL} = -(1.42 \pm 0.04) \times 10^{-3}$  (for *m*), and were independent of position. Thus the superchiral enhancements were  $10.6 \pm 0.6$  (for the *p* enantiomer) and  $11.6 \pm 0.6$  (for the *m* enantiomer).

A quantitative comparison of these results to theory requires consideration of the roles of several types of electronic transitions. Conventional CD in isotropic media (solid or

liquid) arises through an electric dipole-magnetic dipole interference. This is described by equation (2.17). The present experiment involves molecules immobilized in an amorphous polymer host. Though we deem it unlikely, it is conceivable that the ensemble of fluorophores developed a net orientation through short-range interactions with the glass substrate during the deposition of the polymer film. In oriented chiral molecules, electric dipole-electric quadrupole transitions may contribute to CD as well.

We recently calculated the contribution of electric dipole-electric quadrupole transitions to optical dissymmetry in arbitrary electromagnetic fields.<sup>7</sup> The relevant local field property is a third-rank tensor,  $\Theta_{ijk} = E_i \frac{\partial}{\partial x_j} E_k$ , where  $i, j, k$  each vary over the three Cartesian coordinates. Remarkably, for the superchiral fields studied here, the enhancement in optical dissymmetry due to electric dipole-electric quadrupole transitions is identical to the enhancement due to electric dipole-magnetic dipole transitions.<sup>7</sup> Thus the fields are truly superchiral, in that they do not distinguish between the two sources of molecular optical dissymmetry.

On the basis of these considerations, we find that the enhancement in optical dissymmetry is expected to be a function only of the reflectivity of the Al mirror, given by equation (2.19), regardless of possible orientational order in the film. For a film with reflectivity  $R = 0.72$ , the predicted 12.2-fold enhancement at the superchiral nodes is within 15% of the experimental value. Moreover, In the vicinity of superchiral nodes, the theory predicts that the enhancement in the dissymmetry factor is inversely proportional to the

intensity of fluorescence.<sup>5</sup> Figure 4.11(B) shows the fitting of the inverse fluorescence intensity to the enhancement of the dissymmetry factor. The two curves coincide nicely for both the p- and m-enantiomers.

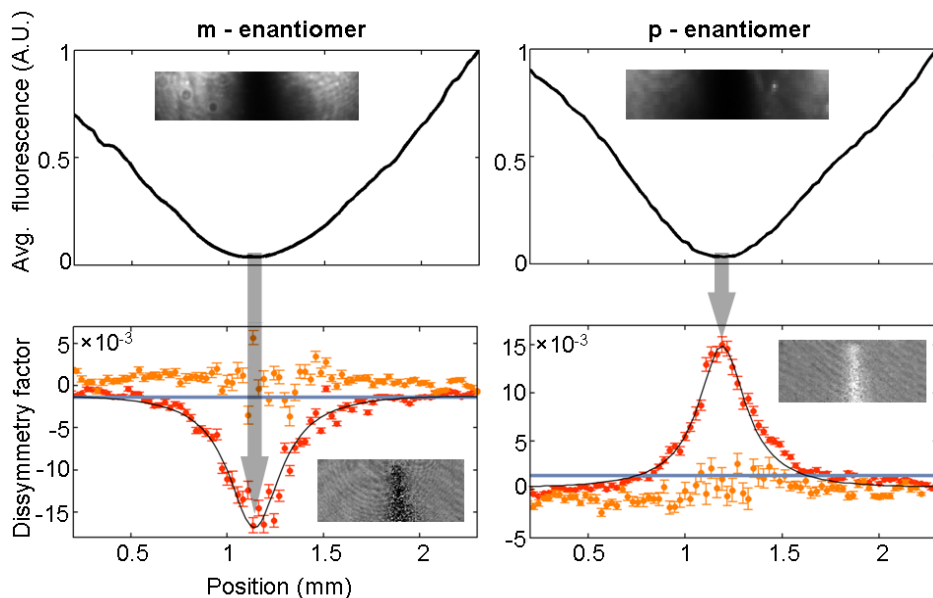


Figure 4.11. Observation of enhanced optical dissymmetry in superchiral light. Upper: Average fluorescence intensity distribution in a superchiral standing wave. Superchiral nodes were identified by their correspondence with minima in the average fluorescence intensity. Insets show images of the average fluorescence. Down: Dissymmetry factor along a line cutting through a superchiral node in chiral (red) and achiral (orange) regions. Blue line marks the value of the position-independent dissymmetry factor measured in chiral films without superchiral enhancement. Black line is the theoretical prediction for the dissymmetry factor. Insets show spatial maps of the dissymmetry factor near the superchiral nodes.

It is perhaps surprising that superchiral light can be created with far-field optics alone. One might expect near-field or plasmonic effects to be necessary to generate highly twisted fields. This observation led us to ask whether there are any local configurations of electric

and magnetic fields and field gradients that can be made with near-field but not far-field optics. One could imagine that the constraints imposed on propagating plane waves might rule out certain local field configurations that were otherwise allowed by Maxwell's equations. In reference 7, we showed that any local field configuration allowed by Maxwell's equations can be created at a single point in space through judicious interference of multiple far-field plane waves. These exotic local fields can enhance a wide variety of molecular multipole transitions, of which the chiral ones discussed here are but one example. Many of these multipole spectroscopies have not previously been demonstrated.

# Chapter 5

## On the chiroptical response of twisted nanowire plasmonic oscillators

Optical activity in chiral metal nanostructures cannot be explained by the interference of electric dipole and magnetic dipole or electric quadrupole: As we demonstrated in section 2.7,  $C$  at nanoscale vanishes, while the structures may still enable chirally sensitive interactions.

In fact, chiral metamaterials are proved to show strongly enhanced chiroptical properties, including strong circular differential scattering<sup>85, 140-142</sup> and asymmetric interactions with chiral molecules.<sup>88, 143</sup> Experiments have probed spatially averaged chiroptical responses; yet the local fields around chiral nanostructures may be highly heterogeneous.

In the chapter, we introduce a simple tunable chiral nanostructure, which we characterized using a circular dichroism imaging microscope. We observed localized chiroptical “hot spots” with dramatically enhanced circular differential scattering. These chiroptical hot spots are not apparent in the spatially averaged spectra. The sign and magnitude of the chiroptical enhancement showed a complex dependence on sample geometry, which we reproduce with a fully retarded analytical scattering model. These results suggest new strategies for engineering enhanced chiral light-matter interactions.

## 5.1 Introduction

Chiral metallic nanostructures have been fabricated with 2-D<sup>144, 145</sup> and 3-D geometries<sup>83, 86, 142</sup> (Figure 5.1). Spatially averaged measurements showed circular dichroism spectra that depended on the nanostructure geometry, but these measurements were not sensitive to spectral features that may be localized to particular regions of the sample. We thus sought to create a simple chiral metal nanostructure where the chiroptical response could be probed as a function of space and device geometry.

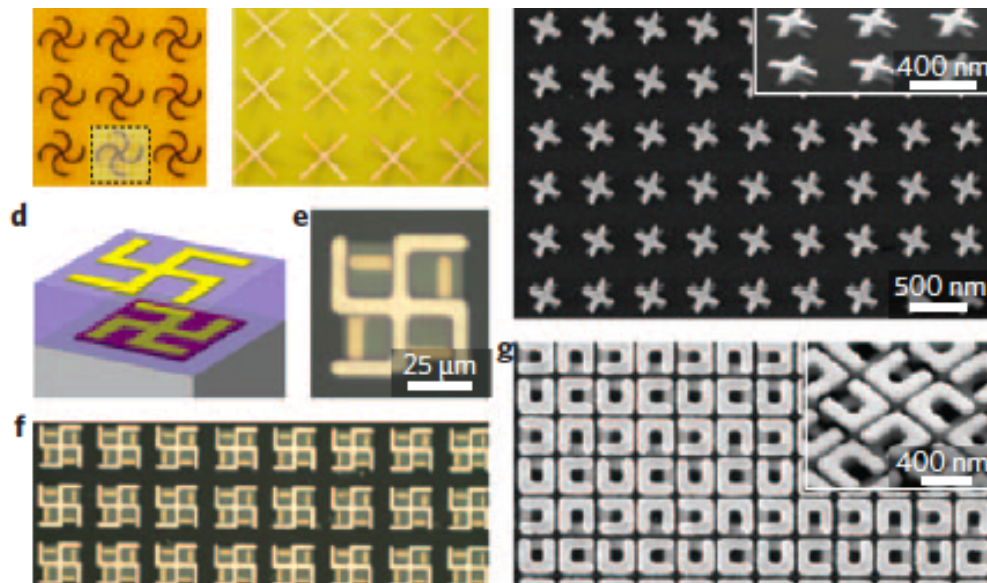


Figure 5.1 a, Experimentally fabricated rosette chiral metamaterials that give negative  $n$  at gigahertz frequencies. b, Experimentally fabricated cross-wire chiral metamaterials that give negative  $n$  at gigahertz frequencies. c, Large-area electron micrograph of a chiral structure composed of right-handed twisted gold crosses, shown at normal and oblique (inset) angles. d, Schematic of the unit cell of a tunable chiral metamaterial. e, Top view of a single unit cell. f, Large-scale top view of a tunable chiral metamaterial. g, Electron micrographs of U-shaped SRRs. The figure is adapted from reference 6.

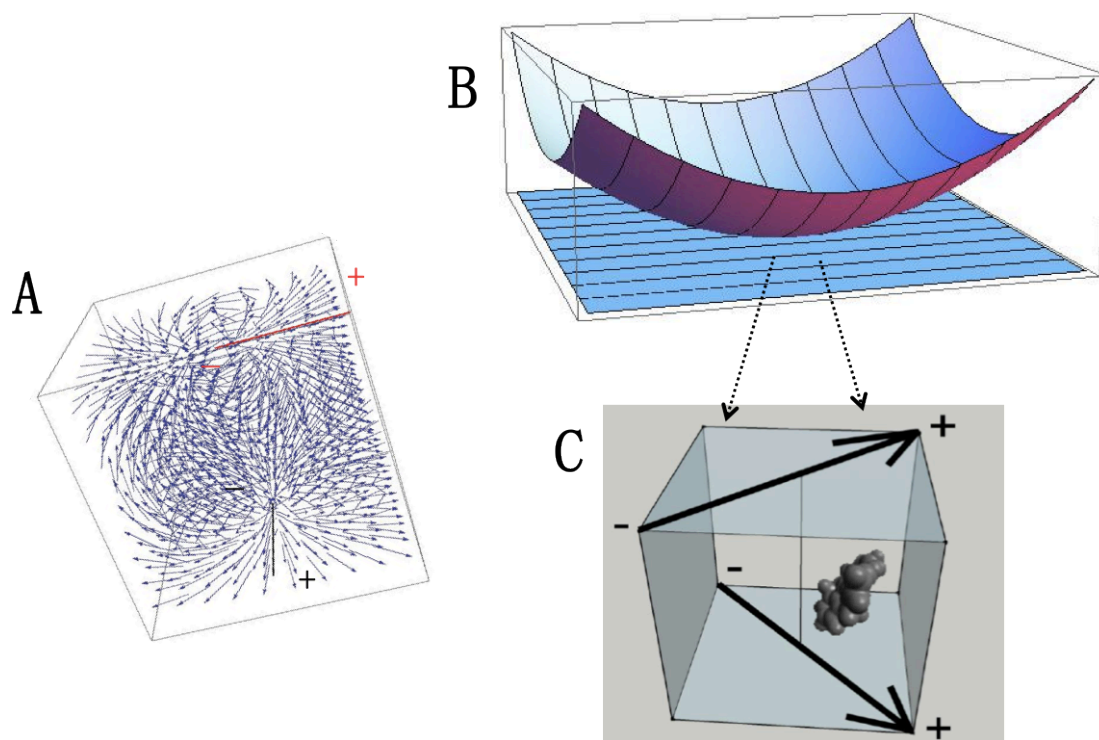


Figure 5.2 (A) A simulation (by Mathematica) of the distribution of electric field around the two static electric dipoles, forming a twisted H configuration; (B) CLIC geometry: The two layers made contact a single point. The lines are nanowires on the respective coverslips; (C) Molecules in the nano-junctions of two nano-rods.

In 1929, Kuhn introduced a simple classical model for a chiral molecule, consisting of two dipolar oscillators, displaced vertically from each other by a distance  $h$ , and rotated about the displacement axis by an angle  $\theta$  (Figure 2.2).<sup>116</sup> Yet a close experimental examination of the Twisted H model was lacking (Figure 5.2 (A)).

We created twisted H dipolar oscillators from crossed nanowires, with gap heights  $h$  ranging from  $h < \lambda$  to  $h > \lambda$  where  $\lambda$  is the optical wavelength. We studied the circular dichroism spectra as a function of  $h$  and  $\lambda$ , and observed remarkable chiroptical “hot spots”

at the crossing points of the nanowires.

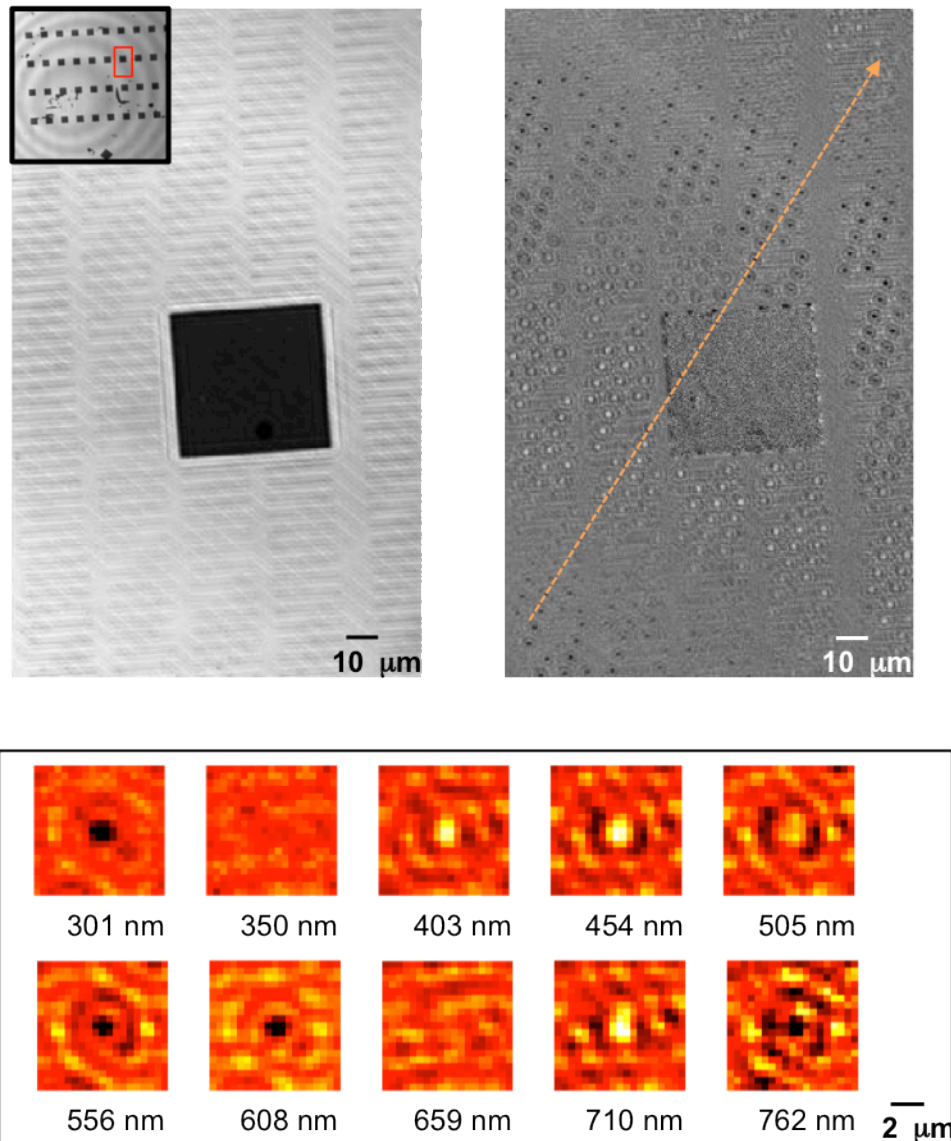


Figure 5.3 Chiral hot-spots in twisted nanowire plasmonic oscillators. Left: Transmitted light image of a crossed nanowire array ( $l = 630$  nm). The black square in the middle is an alignment mark. Inset: low-magnification image showing circular Newton's rings interference pattern. This pattern was used to obtain a precise calibration of the gap at every nanowire crossing. Right: Dissymmetry map of the field of view shown on the left. Hot-spots were clearly visible at the junctions of the nanowires, while the nanowires themselves did not appear. The orange arrow points in the direction of increasing gap height. Within this field of view, the dissymmetry at the nanowire junctions changed sign. Bottom: Close-up images of the dissymmetry patterns at the nanowire junctions as a function of the gap height. Each image was constructed by averaging the dissymmetry maps of all junctions whose gaps were within 10 nm of the stated value. Dissymmetry at the nanowire crossing as a function of gap height.

To create devices with tunable dipole-dipole spacing we used the technique of Convex Lens Induced Confinement (CLIC; Figure 5.2 (B)).<sup>12</sup> We fabricated arrays of parallel metal nanowires on two fused silica substrates. The patterned substrates were aligned face to face with the nanowire axes oriented at  $\pm 45^\circ$  relative to each other. An annular spacer created a  $10\ \mu\text{m}$  air gap between the flat substrates. A convex lens pushed down on the top substrate, causing the substrate to bow downward until it made contact with the bottom substrate at a single point. The deformed substrate had a radius of curvature of  $0.128\ \text{m}^{-1}$ , leading to twisted H nanojunctions with vertical gaps that varied continuously from zero at the contact point to  $10\ \mu\text{m}$  at the edge of the annulus.

The CLIC apparatus was mounted in a homemade microscope designed for spectroscopic polarimetry. The microscope reported maps of the Jones matrices (linear and circular dichroism, linear and circular birefringence) in a sample, with diffraction-limited spatial resolution and  $<10\ \text{nm}$  spectral resolution between wavelengths of 525 and 910 nm.

Figure 5.3 shows an image under transmitted monochromatic light (630 nm) of the crossed nanowire array. At low magnification (4 $\times$ ; inset) we observed a Newton's rings pattern due to interference of reflections from the top and bottom glass-air interfaces. At higher magnification (40 $\times$ ), the crossed nanowire arrays were resolved as well. The square alignment marks enabled precise location of each high magnification image within the low magnification image. The gap height at every nanowire junction was then determined through reference to the Newton's rings pattern.

## 5.2 Experimental procedure and discussions

As shown in Figure 5.4, Light from a tungsten-halogen lamp (Ocean Optics HL-2000) passed through a homemade monochromator. The monochromator consists of two silver-coated concave mirrors ( $f = 100$  mm: Thorlabs CM508-100-P01), one ruled diffraction grating (Thorlabs GR50-1210) and an adjustable mechanical slit (Thorlabs VA100). The light source was placed at the focal plane of the first mirror, thus the reflected beam was collimated. The collimated light was diffracted by the grating and then was collected by the other mirror, which refocused the beam onto the adjustable slit. The diffraction grating sat on a motorized rotation stage (Thorlabs PRM1Z8), as to select the desired wavelength at the exit slit.

The light passed through a linear polarizer selected for good transmission and high contrast in the visible and NIR (Codixx colorPol VIS-IR). The polarizer was mounted on a motorized rotation stage (Thorlabs PRM1Z8). A liquid crystal variable retarder (Meadowlark, LRC-200-IR1-1L) allowed rapid ( $< 30$  ms) switching of the polarization between left circular, right circular, linear horizontal or linear vertical. Rapid switching was essential to achieve sufficient sensitivity for circular dichroism measurements.

Metallic rods exhibit strong linear anisotropy, therefore imperfection in the circular polarization may cause spurious signal in the CD measurement. As shown in Figure 5.5(A), a 96% ellipticity, which suffices for the experiments on small chiral molecules, incurred severe artifacts in the maps of dissymmetry factor for the two-dimensional nanowire arrays. We found that to achieve high quality CPL, it was necessary to adjust

the angle of the polarizer by up to  $3^\circ$  between left- and right-CPL. All the measurements were performed under ellipticities  $> 99\%$ , where the apparent artifacts were eliminated (Figure 5.5(B))

In the squeezing experiment, light passed through an N-BK7 plano-convex lens ( $f =$

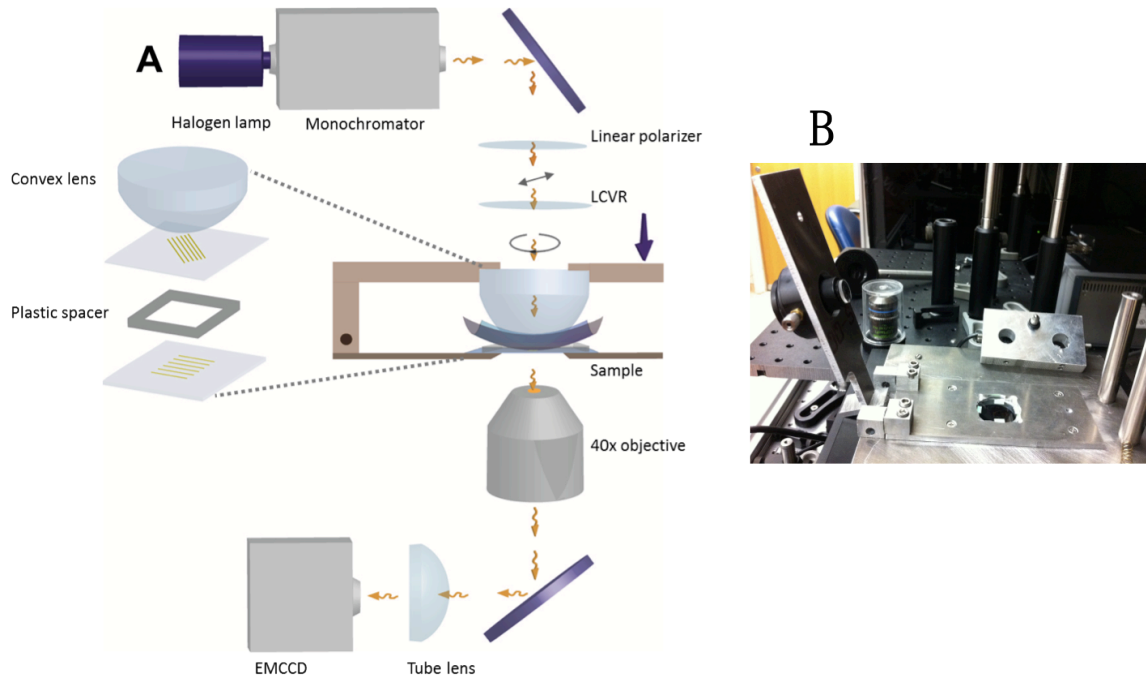


Figure 5.4 (A) Schematic of CLIC apparatus; (B) photograph of the experimental apparatus

100 mm: Thorlabs, LA1207) and sample and was collected by an objective lens (4 $\times$ : Olympus Plan 4 $\times$ /0.1; 40 $\times$ : Olympus LCPlanFL 40 $\times$ /0.60 Ph2). To minimize unwanted interference, immersion oil (Cargille Labs, type FF) was applied in the interface between the lens and the top coverslip. An 18 cm focal length tube lens (Olympus U-TLU-1-2) projected the image onto an EMCCD camera (Andor DU-897, 512 x 512 pixels), cooled to  $-70^\circ\text{C}$ . Physical contact between the two coverslips was ensured by observing areas of

distorted wires, owing to the shear stress upon engaging the two coverslips. We performed the experiment in the area of intact wire arrays that are close to the contact point. As the gap height increased, one of the two wire arrays became blurred thanks to the short focal depth of the 40 x objective. We took care to quantify and correct for spurious linear

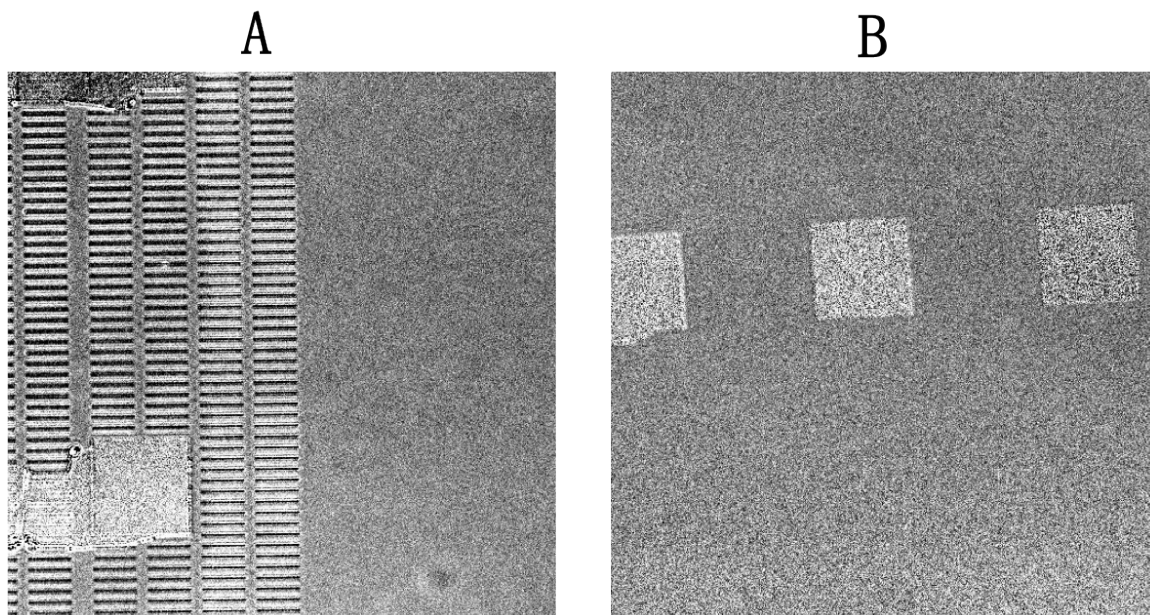


Figure 5.5 Map of dissymmetry factor of single layer of nanowire arrays under left- and right-CPL. (A) Ellipticity = 96% for two CPLs; (B) ellipticity > 99% for two CPLs

birefringence or linear dichroism in any of the optical elements.

Linear dichroism and linear birefringence of a single gold nanowire are quantified by the set of polarization optics and the EMCCD. For measurements of linear dichroism, the LCVR was switched between zero- and half-wave plate. Thus the polarization plane of incident light is either perpendicular or in parallel to the nanowire orientation. Transmission intensity was recorded by the EMCCD (Figure 5.6). For measurements of linear birefringence, a second linear polarizer (Codixx colorPol VIS-IR) was placed at 45°

to the ground between the objective and the tube lens. The LCVR alternated between 1/4- and 3/4-wave plate, creating create left- and right-CPL on the sample, respectively (Figure 5.7). Amplitude of linear birefringence may be found at Table 5.1 for a few selected wavelengths.

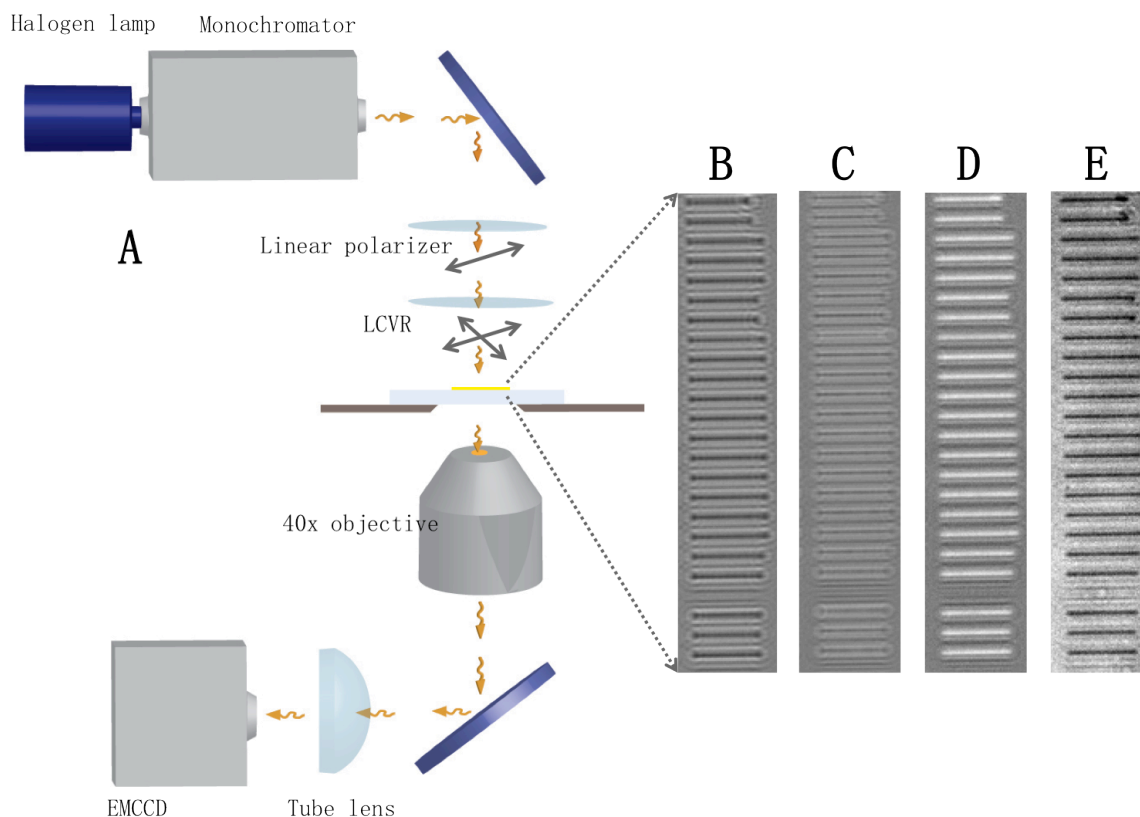


Figure 5.6 A. Experimental apparatus for measuring linear dichroism of single nanowire. B. Maps of linear dichroism at 600 nm; C. maps of linear dichroism at 630 nm. D. Maps of linear dichroism at 760 nm. E. Photograph of nanowire arrays

In a typical data set, 40 images were acquired under alternating left- and right-CPL at each wavelength. Typical exposure times were 300 ms. The orientations of the optics and the LCVR control voltages were tuned manually to achieve maximal ellipticities (> 99%) at each wavelength. The apparatus was controlled by custom software written in

LabView and analysis was performed in Matlab.

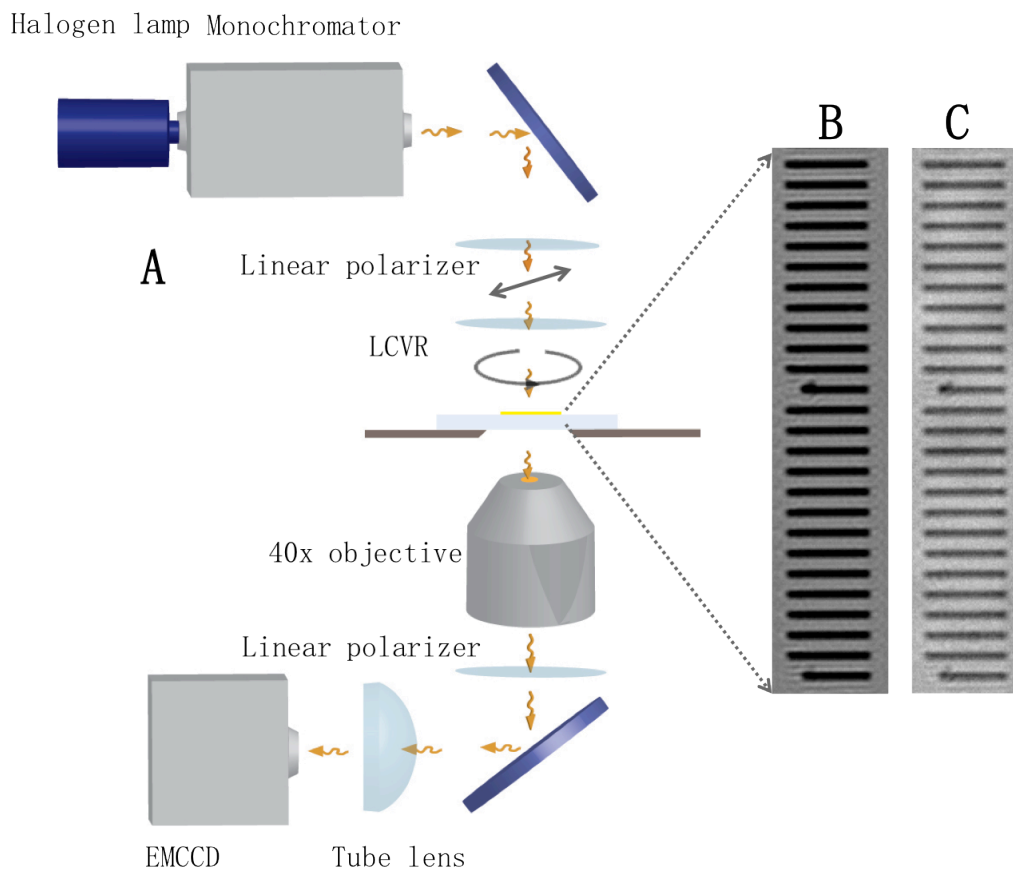


Figure 5.7 A. Apparatus for measuring linear birefringence of single nanowires; B. maps of linear birefringence at 630 nm; C. photograph of nanowire arrays.

### 5.3 Experimental results and data analysis

We found that the lamp exhibited small frame-to-frame fluctuations in intensity ( $< 1\%$ ), and that the transmission of the LCVR varied by  $\sim 1\%$  depending on the control voltage. To correct for these artifacts, we normalized each frame by the intensity in a nanowire-free region. We then averaged measurements taken under corresponding polarizations.

Circular dichroism dissymmetry images were calculated according to:

$$g = \frac{2(I_L - I_R)}{I_L + I_R}$$

where  $I_L$  and  $I_R$  represent the images acquired under left- and right-CPL, respectively. The coordinates of nanowire crossings were determined by automated image processing.

Each high-magnification image was located within a low-magnification image of Newton's rings. The weak interference pattern visible within the high magnification image was used to calculate the gap height  $h$  at each nanowire junction. Dissymmetry images around nano-junctions with similar values of  $h$  were grouped and averaged. To our surprise, "hot spots" appeared in this dissymmetry map at the nanowire crossings (Figure 5.3). The dissymmetry pattern around the hot spot varied with separation between the nanowires, and even changed sign at some gap heights.

To explore further these chiral hot spots we acquired circular dichroism images as a function of wavelength and gap height. We extracted from these images the dissymmetry factor at the nanowire crossing points,  $g(h, \lambda)$ . This quantity oscillated as a function of  $h$ , with a period of  $\lambda/2$ . However, the  $h$ -dependence was not sinusoidal, and at some wavelengths  $g$  was predominantly positive, at some wavelengths  $g$  was predominantly negative, and at others  $g$  changed sign as a function of  $h$ . Switching the orientation of the top nanowires from  $+45^\circ$  to  $-45^\circ$  changed the sign of  $g(h, \lambda)$ , as expected.

To interpret the surprising dependence of  $g$  on  $h$  and  $\lambda$ , we next developed an analytical model of twisted H dipole oscillators, including fully retarded electrodynamic coupling. We measured the dielectric properties of individual, uncoupled rods. The rods were coupled in the first Born approximation using the retarded Green's function. The fields scattered by the rods in the forward direction were added to the incident fields, to

determine the intensity in the forward direction. This calculation is modeled on the work of Keller and Bustamante.<sup>14</sup> Repeating this calculation for left- and right-CPL produced a prediction for the wavelength- and separation-dependent dissymmetry factor.

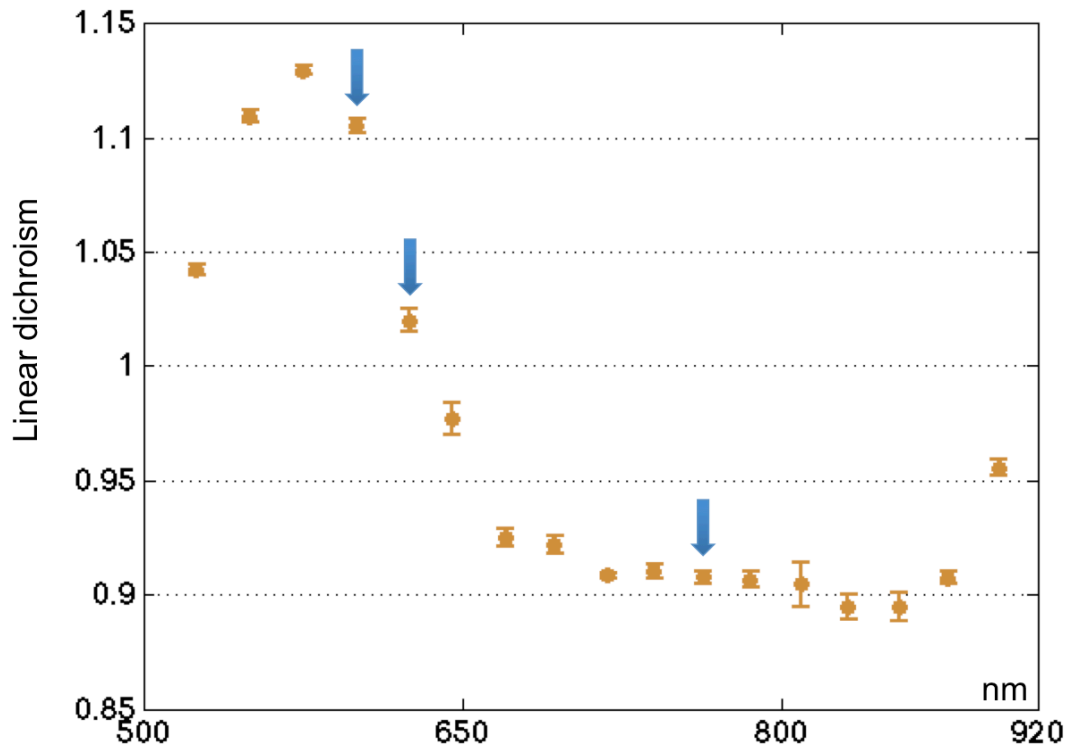


Figure 5.8 Linear dichroism of single nano wires as a function of excitation wavelength

Let's recall the fitting formula we presented in section 2.7:

$$\frac{2\left(|\mathbf{E}_d^+|^2 - |\mathbf{E}_d^-|^2\right)}{|\mathbf{E}_d^+|^2 + |\mathbf{E}_d^-|^2} = g(\rho, h, \beta, \theta, \mu, \psi, E_0). \quad (5.1)$$

Angle  $\theta$  are  $\pm 45^\circ$  in the experiment.  $h$  is determined by counting interference fringes between the two glass substrates. The polarizability tensors of the individual rods can be calculated numerically or measured experimentally. We chose an experimental approach

and determined linear dichroism  $\rho$  and linear birefringence  $\beta$  spectra of rods. Our results are in quantitative agreement with preceding measurements on chemically synthesized Au nanorods.

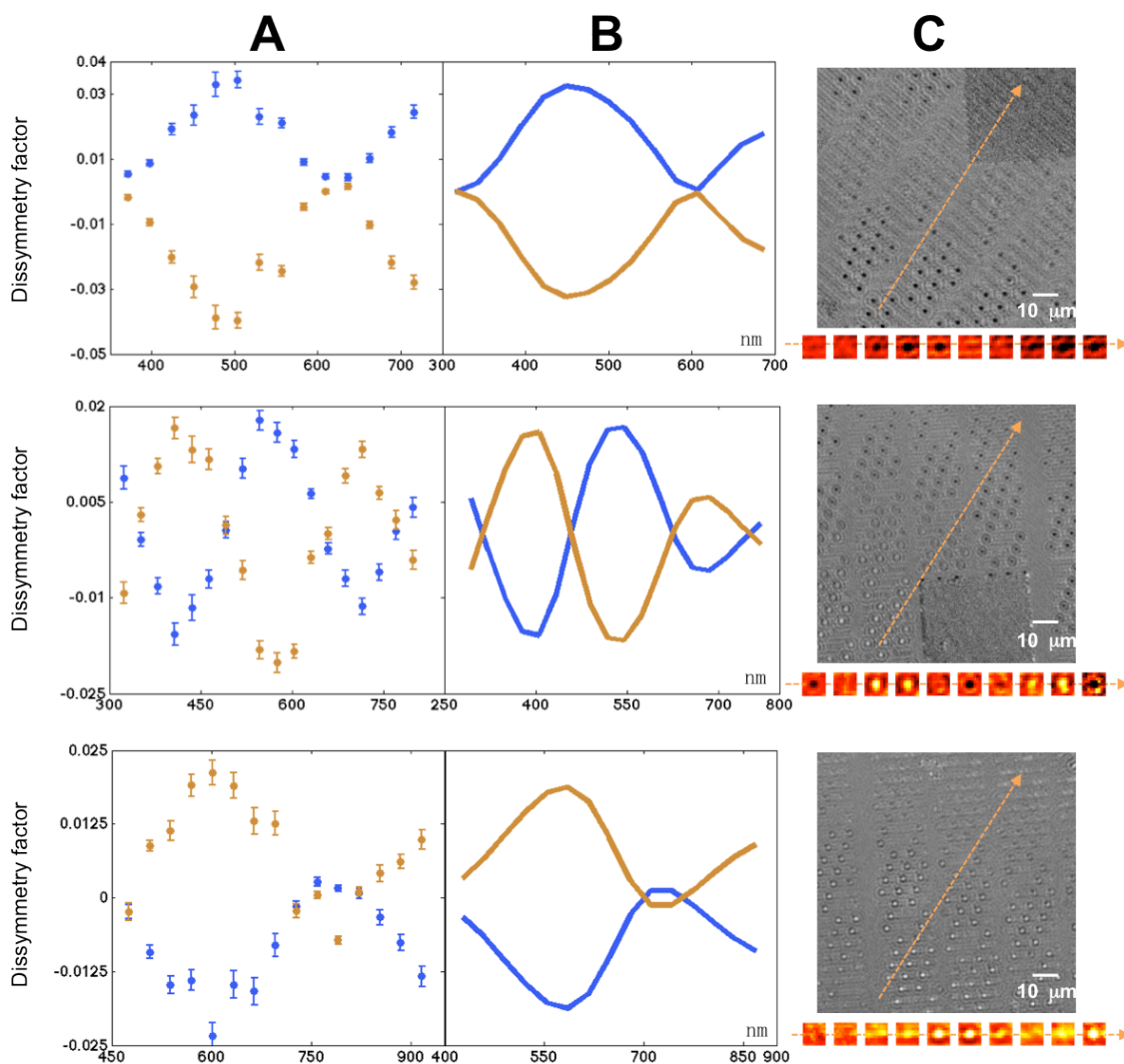


Figure 5.9 (A) dissymmetry factors at the central pixel of chiroptical hot spots as a function of gap height; (B) the optimal fittings of dissymmetry factors at three exciting wavelengths; (C) maps of dissymmetry factor.

The linear dichroism data may be best understood by the use of screening parameter,  $\kappa$ .

$\kappa$  is determined by the particle shape, and conditions the plasmonic resonance. When the incident electric field is polarized parallel to the main axis of a nanowire or prolate ellipsoid, the corresponding screening parameter  $\kappa$  is large and leads to an extinction maximum at long wavelength. On the other hand, when the EM field is perpendicular to the particle axis,  $k$  is small, thus leading to an extinction maximum at short wavelengths. In our wire geometry, the transition took place at around 630 nm (Figure 5.8).

$\lambda$ (nm)	Linear dichroism ( $\rho$ )	Linear birefringence ( $\beta$ )	$h$ (nm)	Global phase ( $\psi$ )	A·V ( $\mu\text{m}^3$ )	$E_{\text{inc}}/E_{\text{sca}}$
600	1.1	0.11	360 - 720	3.0761	$1.07 \times 10^{-2}$	2.1
630	1.02	0.15	310 - 770	3.0607	$0.78 \times 10^{-2}$	1.9
760	0.91	0.1	470 - 900	3.0701	$1.18 \times 10^{-2}$	2.0

Table 5.1 fitting (the red) and measured (the blue) parameters in the three selected wavelength.

The linear birefringence measurements yielded the relative phase shift in scattered light in the parallel vs. perpendicular orientations. This measurement did not yield the phase shift of the scattered light relative to the incident light. We left this overall phase,  $\psi$ , as a fitting parameter. Two other fitting parameters are the external field strength,  $E_0$ , and the interaction strength  $\mu$ .

Figure 5.9 shows the fitting of the dissymmetry factors as a function of gap height,  $h$ , at three selected wavelengths, 600 nm, 630 nm, and 760 nm. The theoretical fitting and

data coincide nicely for both enantiomeric configurations ( $\theta = \pm 45^\circ$ ). A summary of measured and fitting parameters may be found in Table 5.1.

#### **5.4 Tunable metamaterials**

In metamaterial research, the conventional fabrication processes create rigid structures with inherent and limited response to a narrow frequency band at any given time. Greater flexibility and functionality, as required for any practical use, may be achieved by controlling the effective EM parameters of the artificial medium through externally tunable components. One venue on pursuing the goal is through the integration of the dielectric/metallic structures with other classes of materials, such as semiconductor, ferrite, and liquid crystal. Another approach, “structural tuning”, is based on a continuous adjustment of the lattice structure. For example, a recent study employed a highly compliant polymeric substrate (PDMS), which rendered the deliberate deformation of unit cells that finely shifted their resonant frequency. The CLIC apparatus, as we demonstrated here, is another viable option adding to the arsenal.

In principle, the CLIC geometry may generate a gap height down to only a few nanometers, allowing observing physical and/or chemical reactions in the confined space to an extreme. For example, one may spin coat a thin layer of chiral molecules on the interface, and examine chiroptical excitation of molecules in the twisted nano-junctions as a function of gap height. Such experiment is difficult with traditional MIM (metal-insulator-metal) or any other 3D chiral geometry, owing to the integrated nanofabrication protocols. One constraint in the current experiment is the shear stress

upon engagement, which crumbles the nanostructure in the vicinity of the point contact. Better surface protection is required for future experiment.

### **5.5 Appendix: Fabrication of gold nanowire arrays**

Gold nanowires were fabricated using E-beam lithography. Specifically, We deposited a solution of poly(methyl methacrylate) (PMMA, molecular weight 495,000) onto a fused silica coverslip (40 s at 4000 rpm). After baking at 180 °C for 10 min, another sample of PMMA (molecular weight 950,000) was spun onto the first layer (40 s at 4000 rpm). The top layer of heavier molecular weight is more resistant to electron beams than the bottom layer, resulting in an easy metal liftoff process. After the second layer deposition, we baked the sample at 180 °C for 10 min. Subsequently, water-soluble conducting polymer (Showa Denko, Espacer 300) was deposited (30 s at 2000 rpm). A conductive layer is necessary for E-beam lithography; otherwise the sample will have significant charge buildup disturbing the electron beam path.

The standard E-beam (Raith 150) exposure is ensued by a development in 1:3 MIBK:IPA for 40 s, yielding the wire shaped grooves in the PMMA. A 1.5 nm titanium and 30 nm gold layer was deposited onto the substrate and then liftoff was performed in acetone overnight. Titanium is critical because gold does not adhere well to the substrate during the liftoff step. We examined the nanostructure under SEM and optical microscope. The nanowires are 100 nm in width, 20  $\mu\text{m}$  in length and 30 nm in thickness. The spacing between adjacent wires is 5  $\mu\text{m}$ .

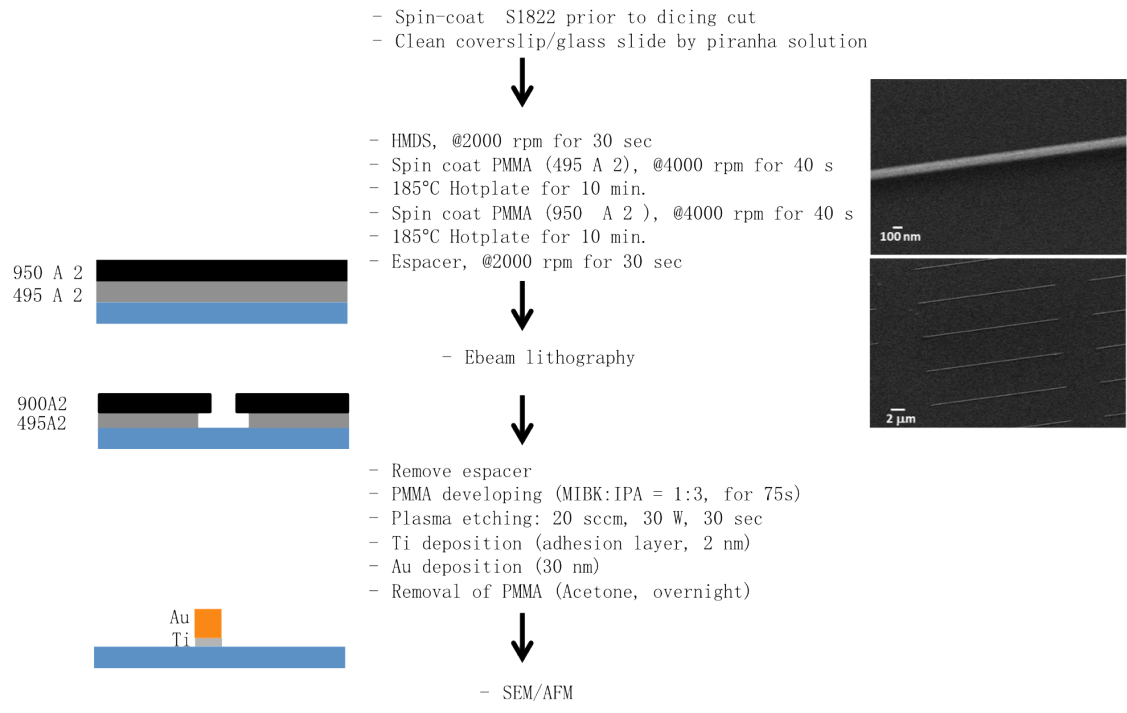


Figure 5.10 Nanofabrication of nanowire arrays: procedure (left) and photograph of wires under SEM (right).

# Chapter 6

## Conclusion and future perspectives

In the thesis, I have discussed (i) the underlying theory on quantifying chirality of light, both in a far-field limit and at the nanoscale, (ii) an image-based methodology in examining chiroptical excitation in optically thin films, (iii) and novel approaches (CLIC for example) for preparing structures of interest.

Much work remains in the three directions. For example, our work has treated the electromagnetic field classically. What does optical chirality look like in a quantized radiation field, and how does it behave? Can superchiral light induce chirally selective photochemical reactions with large enough enantiomeric excess to be useful (e.g. to synthesize drugs)? How does superchiral light interact with cold atoms, metallic nanostructures, or magnetic particles? What are the forces that superchiral light generates on dielectric particles? What are the other imaging schemes with improved speed and accuracy? How may the CLIC geometry be applied to study other interesting nano-optical phenomena? In the chapter, I will examine some of the issues in detail and suggest a few interesting and/or promising future directions.

### **6.1 More theory: On quantizing optical chirality and spin angular momentum of photons**

It is straightforward to quantize the optical chirality and the associated chiral flux.

We recall the definition of the two quantities:

$$C \equiv \varepsilon_0 \mathbf{E} \cdot \nabla \times \mathbf{E} + \frac{1}{\mu_0} \mathbf{B} \cdot \nabla \times \mathbf{B} \quad (6.1)$$

$$\mathbf{F} \equiv \frac{1}{2\mu_0} \{ \mathbf{E} \times (\nabla \times \mathbf{B}) - \mathbf{B} \times (\nabla \times \mathbf{E}) \}, \quad (6.2)$$

where  $\varepsilon_0$  and  $\mu_0$  are the permittivity and permeability of free space, respectively, and  $\mathbf{E}$  and  $\mathbf{B}$  are the time-dependent electric and magnetic fields. In Fourier space, the total chirality and flux in the entire space are respectively:

$$\int C d^3\mathbf{r} = -i\hbar c \sum k^2 \left( \vec{a}^+ \times \vec{a}^- \right) \cdot \hat{\mathbf{k}}, \quad (6.3)$$

$$\int \mathbf{F} d^3\mathbf{r} = -i\hbar c^2 \sum k^2 \left( \vec{a}^+ \times \vec{a}^- \right), \quad (6.4)$$

where  $\vec{a}(\mathbf{k}, t) = -i\sqrt{\varepsilon_0/2\hbar\omega}(\mathbf{e}_\perp - c\hat{\mathbf{k}} \times \mathbf{b})$  is the quantum annihilation operator for photons with  $\mathbf{e}_\perp$  and  $\mathbf{b}$  the electric and magnetic fields in Fourier space,  $\mathbf{k}$  the wave vector, and  $\hat{\mathbf{k}} \equiv \frac{\mathbf{k}}{|\mathbf{k}|}$ , and “+” represents a complex conjugation.<sup>111, 112</sup>

We found the relations of no significant physical implications. Instead, the quantity  $-i\hbar c \sum \left( \vec{a}^+ \times \vec{a}^- \right) \cdot \hat{\mathbf{k}}$  attracted our attention because of its apparent connection to angular momentum of an EM field. In the following, we switch gear towards studying angular momentum EM fields and by the end, comment on the relations between photon spin and chirality of light.

An electromagnetic field carries angular momentum in addition to energy and momentum. As a fundamental descriptor, angular momentum accounts for many properties of an EM field and its interactions with matter. Angular momentum of light is

defined as:

$$\mathbf{J} = \epsilon_0 \int d^3r \mathbf{r} \times (\mathbf{E} \times \mathbf{B}), \quad (6.5)$$

where  $\epsilon_0$  is the permittivity of free space,  $\mathbf{E}$  and  $\mathbf{B}$  are the time-dependent electric and magnetic fields, and  $\mathbf{r}$  is the position vector.  $\mathbf{J}$  is routinely divided into the longitudinal and transverse part, associated with a longitudinal electric field,  $\mathbf{E}_{//}$ , that originates from the charge distribution  $\rho(\mathbf{r}, t)$  and with a transverse electric field,  $\mathbf{E}_{\perp}$ , that relates to propagating waves in space, respectively.<sup>111</sup>

Quantum mechanically, the photon angular momentum along the direction of its motion can have only two eigenvalues  $\pm \hbar$ , which correspond to the left- ( $+\hbar$ ) and right- ( $-\hbar$ ) - circular polarization. In recent years, there are growing interests, both in theory and experiment, in exploring spin-dependent transportation of photons. One major progress is the "spin hall effect of light", where beams of left- and right-circularly polarized light (CPL) displace oppositely in the plane perpendicular to the refractive index gradient upon refraction in an air-glass interface.<sup>146</sup> The phenomenon was largely understood by performing a geometrical calculation on the trajectory of light in momentum-space.<sup>147</sup> Alternatively, one may ask how spin current of photons is properly defined and subsequently, if a material torque may affect its propagation. In the parallel study of electron spins, the same questions have been actively pursued, bearing good fruits.<sup>148, 149</sup> No such studies, however, have been extended for photon spins.

The total angular momentum for EM fields is composed of longitudinal (LAM) and transverse (TAM) parts.<sup>111</sup> As we are only interested in the radiation field, the TAM will

be examined in the article. TAM can be written as:

$$\mathbf{J}_{\text{trans}} = \epsilon_0 \int d^3r \mathbf{r} \times (\mathbf{E}_{\perp} \times \mathbf{B}). \quad (6.6)$$

Routinely,  $\mathbf{J}_{\text{trans}}$  is decomposed into intrinsic  $\mathbf{S}$  and external  $\mathbf{L}$  that are associated with field polarization<sup>111, 112</sup> and spatial distribution,<sup>2, 150</sup> respectively:

$$\mathbf{J}_{\text{trans}} = \epsilon_0 \int d^3r \left\{ \sum_i E_{\perp,i} (\mathbf{r} \times \nabla) A_{\perp,i} + \mathbf{E}_{\perp} \times \mathbf{A}_{\perp} \right\} = \mathbf{L} + \mathbf{S}, \quad (6.7)$$

where  $\mathbf{A}_{\perp}$  is the transverse magnetic vector potential,  $i$  is the spatial coordinates (i.e.  $x, y, z$ ).

$\mathbf{L} = \epsilon_0 \int d^3r \left( \sum_i E_{\perp,i} (\mathbf{r} \times \nabla) A_{\perp,i} \right)$  and  $\mathbf{S} = \epsilon_0 \int d^3r (\mathbf{E}_{\perp} \times \mathbf{A}_{\perp})$ .<sup>151-153</sup> Conventional wisdom often assigns  $\mathbf{S}$  to the total spin angular momentum for an EM field. Spatial density of photon spin is accordingly determined by  $\mathbf{s}_1 = \epsilon_0 (\mathbf{E}_{\perp} \times \mathbf{A}_{\perp})$ .<sup>154, 155</sup>

The conventional division of TAM into  $\mathbf{S}$  and  $\mathbf{L}$  suffers apparent flaws that prevent the quantities from being relevant to observables:

(1) Any fundamental descriptor in EM fields should put electric and magnetic fields on equal footings, thanks to the unification of  $\mathbf{E}$  and  $\mathbf{B}$  under special relativity.<sup>2</sup> However,  $\mathbf{E}$  and  $\mathbf{B}$  are not equivalently included in either  $\mathbf{L}$  or  $\mathbf{S}$ : Electric field reflects a variance of  $\mathbf{A}$  in time, while magnetic field relates to spatial inhomogeneity of  $\mathbf{A}$ .

(2) The physical interpretation of  $\mathbf{S}$  remains elusive. Giving the nonexistence of a rest frame for a propagating photon, no proper definition of its spin operator is viable. S. J. Enk suggested that the commutation relation for  $\mathbf{S}$  satisfies  $[S_i, S_j] = 0$  (where  $i, j = x, y, z$ ), which do not generate a rotation in space.<sup>156</sup> Strictly speaking,  $\mathbf{S}$  is not an operator for angular momentum.

In addition, the mathematical transformation in equation (6.7) is not unique under the assumption that fields vanish at infinity. The particular decomposition of  $\mathbf{J}_{\text{trans}}$  in equation (6.7) is short of any theoretical underpinnings.

To address the first concern, we use the transverse electric vector potential  $\mathbf{C}$ <sup>102, 157</sup> and introduce transverse vector  $\mathbf{m}_{\perp}$ , which satisfies  $\nabla \times \mathbf{m}_{\perp} = \mathbf{j}_{\perp}$  and  $\mathbf{j}_{\perp}$  is the transverse component of material current density.  $\mathbf{C}$  and  $\mathbf{m}_{\perp}$  satisfy the following relations, as ensured by Maxwell's Equations:

$$\begin{aligned}\mathbf{E}_{\perp} &= c^2(\nabla \times \mathbf{C}) = -\frac{\partial \mathbf{A}_{\perp}}{\partial t} \\ \mathbf{B} &= \frac{\partial \mathbf{C}}{\partial t} + \mu_0 \mathbf{m}_{\perp} = (\nabla \times \mathbf{A}_{\perp}),\end{aligned}\tag{6.8}$$

where  $\mu_0$  is the permeability of free space, and  $c$  is the speed of light. An EM field may be either constructed by the pair  $(\mathbf{E}, \mathbf{B})$  or  $(\mathbf{A}, \mathbf{C})$ . We rewrite the transverse angular momentum as:

$$\begin{aligned}\mathbf{J}_{\text{trans}} &= \frac{\epsilon_0}{2} \int d^3r \mathbf{r} \times (\mathbf{E}_{\perp} \times (\nabla \times \mathbf{A}_{\perp})) - \frac{1}{2\mu_0} \int d^3r \mathbf{r} \times (\mathbf{B} \times (\nabla \times \mathbf{C})) \\ &= \frac{1}{2} \int d^3r \left\{ \epsilon_0 \sum_i E_{\perp,i} (\mathbf{r} \times \nabla) A_{\perp,i} - \frac{1}{\mu_0} \sum_i B_i (\mathbf{r} \times \nabla) C_i \right\} + \frac{1}{2} \int d^3r \left\{ \epsilon_0 (\mathbf{E}_{\perp} \times \mathbf{A}_{\perp}) - \frac{1}{\mu_0} (\mathbf{B} \times \mathbf{C}) \right\}.\end{aligned}\tag{6.9}$$

In equation (6.9), the intrinsic part of  $\mathbf{J}_{\text{trans}}$  becomes,  $\frac{1}{2} \int d^3r \left\{ \epsilon_0 \mathbf{E}_{\perp} \times \mathbf{A}_{\perp} + \frac{1}{\mu_0} \mathbf{B} \times \mathbf{C} \right\}$  with spatial density:

$$\mathbf{s}_2 = \frac{1}{2} \left\{ \epsilon_0 \mathbf{E}_{\perp} \times \mathbf{A}_{\perp} - \frac{1}{\mu_0} \mathbf{B} \times \mathbf{C} \right\}.\tag{6.10}$$

$\mathbf{s}_2$  puts  $\mathbf{B}$  and  $\mathbf{E}$  on equal footings, as can be seen from equation (6.8). This becomes more explicit in a time-harmonic electromagnetic field, where  $\mathbf{s}_2$  becomes

$$\frac{1}{2\omega^2} \left\{ \epsilon_0 \mathbf{E}_\perp \times \frac{\partial \mathbf{E}_\perp}{\partial t} + \frac{1}{\mu_0} \mathbf{B} \times \frac{\partial \mathbf{B}}{\partial t} \right\} \quad \text{while} \quad \mathbf{s}_1 = \frac{1}{\omega^2} \left\{ \epsilon_0 \mathbf{E}_\perp \times \frac{\partial \mathbf{E}_\perp}{\partial t} \right\}.$$

Decomposing an EM field into the transverse and longitudinal components is unique, even in the presence of material charge and current;<sup>111</sup> therefore,  $\mathbf{s}_2$  is a generally valid quantity. In addition, both  $\mathbf{A}_\perp$  and  $\mathbf{C}$  are invariant under gauge transformation. The quantity  $\mathbf{s}_2$  is gauge-invariant and therefore a physical observable.

Now we are to address the second concern. We switch to the momentum space and quantize the EM radiation fields. Fields in Fourier space may be expressed as:

$$\begin{aligned} \mathbf{e}_\perp &= i \sqrt{\frac{\hbar \omega}{2\epsilon_0}} (\vec{a}(\mathbf{k}, t) - \vec{a}^*(-\mathbf{k}, t)), \\ \mathbf{b} &= i \sqrt{\frac{\hbar \omega \mu_0}{2}} (\hat{\mathbf{k}} \times \vec{a}(\mathbf{k}, t) + \hat{\mathbf{k}} \times \vec{a}^*(-\mathbf{k}, t)), \\ \mathbf{a}_\perp &= \sqrt{\frac{\hbar}{2\omega \epsilon_0}} (\vec{a}(\mathbf{k}, t) + \vec{a}^*(-\mathbf{k}, t)), \\ \mathbf{c} &= -\sqrt{\frac{\hbar \mu_0}{2\omega}} (\hat{\mathbf{k}} \times \vec{a}(\mathbf{k}, t) - \hat{\mathbf{k}} \times \vec{a}^*(-\mathbf{k}, t)). \end{aligned} \quad (6.11)$$

Integrating  $\mathbf{s}_1$  and  $\mathbf{s}_2$  over space yield  $\mathbf{S} = \int d^3r \mathbf{s}_1 = \int d^3r \mathbf{s}_2 = -i\hbar \sum_{\mathbf{k}} \vec{a}^+(\mathbf{k}, t) \times \vec{a}(\mathbf{k}, t)$ , where summation is over the entire Fourier space. Choosing two circular polarizations,  $\vec{a}_R(\mathbf{k}, t)$  and  $\vec{a}_L(\mathbf{k}, t)$ , as the eigenmodes in the Hilbert Space,  $\mathbf{S}$  becomes:

$$\mathbf{S} = \hbar \sum_{\mathbf{k}} \hat{k} (\vec{a}_L^+(\mathbf{k}, t) \vec{a}_L(\mathbf{k}, t) - \vec{a}_R^+(\mathbf{k}, t) \vec{a}_R(\mathbf{k}, t)). \quad (6.12)$$

Therefore,  $\mathbf{S}$  is a measure of the difference in the photon number between left- and right-circular polarizations over all wave vectors.

The motivation to include the transverse vectors  $\mathbf{C}$  and  $\mathbf{m}_\perp$ , and to replace  $\mathbf{s}_1$  with  $\mathbf{s}_2$

largely lies in deriving a continuity equation for photon spins. In general, the operator for spin density of an arbitrary particle may be defined as  $s_z = \psi^\dagger(\mathbf{r})\hat{s}_z\psi(\mathbf{r})$ , and spin current density  $\mathbf{j}_s = \frac{1}{2}\psi^\dagger(\mathbf{r})\{\hat{\mathbf{v}}, \hat{s}_z\}\psi(\mathbf{r})$ , where  $\hat{s}_z$  is the  $z$  component of spin operator,  $\hat{\mathbf{v}}$  is the velocity operator,  $\{, \}$  is the Poisson commutator, and  $\psi(\mathbf{r})$  is the wave function of particle at position  $\mathbf{r}$ .<sup>148</sup> For an arbitrary EM field,  $\hat{\mathbf{v}}$  equals  $c\hat{\mathbf{k}}$ . We define:

$$\begin{aligned} s_z &= \frac{1}{2} \sqrt{\frac{\epsilon_0}{\mu_0}} (\mathbf{B} \cdot \mathbf{A}_\perp + \mathbf{E}_\perp \cdot \mathbf{C}), \\ \mathbf{j}_s &= \frac{c}{2} \left\{ \epsilon_0 \mathbf{E}_\perp \times \mathbf{A}_\perp - \frac{1}{\mu_0} \mathbf{B} \times \mathbf{C} \right\}, \\ t &= -\frac{c}{2} \left\{ (\nabla \times \mathbf{m}_\perp) \cdot \mathbf{C} + (\nabla \times \mathbf{C}) \cdot \mathbf{m}_\perp \right\}. \end{aligned} \quad (6.13)$$

We then find the following continuity equation:

$$\frac{\partial s_z}{\partial t} + \nabla \cdot \mathbf{j}_s = t. \quad (6.14)^\vee$$

Equation (10) is the main result of the article. Structurally, It closely resembles to the continuity equation for electron spins. Integrating  $s_z$  and  $\mathbf{j}_s$  over the whole space, we have:

$$\begin{aligned} G_z &= \int s_z d^3r = -i\hbar \sum_{\mathbf{k}} (\vec{a}^\dagger \times \vec{a}) \cdot \mathbf{k} \\ \mathbf{Q} &= \int \mathbf{j}_s d^3r = -i\hbar c \sum_{\mathbf{k}} (\vec{a}^\dagger \times \vec{a}). \end{aligned} \quad (6.15)$$

For photons, only  $z$ -component of spin operator is well-defined, thanks to the transversality of radiation EM fields. *Helicity* of photons, i.e. the component of its spin angular momentum along the momentum vector  $\mathbf{k}$ , is defined as  $\hat{s}_z = \hat{\mathbf{s}} \cdot \hat{\mathbf{k}}$ , where  $\hat{\mathbf{s}}$  is the spin

---

<sup>∨</sup> We note that the derivation of the continuity equation for photon spins is closely related to the continuity equation for optical chirality. The mathematical transformations presented in equation (2.15) may be directly applied here.

angular momentum. In Fourier space,  $\hat{s}_z = -i\hbar(\bar{a}^+ \times \bar{a}) \cdot \hat{\mathbf{k}}$ . Therefore  $G_z$  is the total photon *helicity* and  $s_z$  in equation (11) is the density of photon helicity in real space. Without the source term, *helicity* is a conserved quantity, as shown in equation (10). The conservation of photon *helicity* in vacuum is a well-known result from the axial symmetry of light field along its propagating direction. A recent article exhibited a similar conservation law of photon spin in vacuum as we conclude here.<sup>157</sup>

Moreover, considering photon speed as the constant  $c$ , the density of photon spin current in Fourier space becomes  $\frac{1}{2}\{\hat{\mathbf{v}}, \hat{s}_z\} = -i\hbar c(\bar{a}^+ \times \bar{a})$ , with the corresponding total spin current  $-i\sum_{\mathbf{k}} \hbar c(\bar{a}^+ \times \bar{a}) = \mathbf{Q}$ . Therefore,  $\mathbf{j}_s = \frac{c}{2}\left\{\varepsilon_0 \mathbf{E}_\perp \times \mathbf{A}_\perp - \frac{1}{\mu_0} \mathbf{B} \times \mathbf{C}\right\}$  is the current density of photon spin in real space.  $\mathbf{j}_s$  is not necessarily parallel to the wave vector of a propagating field. For example, the direction of spin current is parallel to wave vector in left-CPL, while is antiparallel to wave vector in right-CPL.

Comparing the equation (6.13) and (6.10), we find the simple relation  $\mathbf{j}_s = c\mathbf{s}_2$ . Accordingly,  $\mathbf{S} = \mathbf{Q}/c$  relates to the spin current for photon field rather spin angular momentum. This is consistent with the commutation relations  $[S_i, S_j] = 0$  ( $i, j = x, y, z$ ).

With the proper physical interpretation of  $\mathbf{S}$  and  $\mathbf{s}_2$ , let's examine an exemplary EM configuration. The field is composed of two free counter-propagating waves with orthogonal linear polarizations, equal amplitudes  $E_0$ , and the same frequency  $\omega$ .

The field setup generates the so-called ‘‘polarization gradient’’: the electric field spatially changes from linear to circular polarization every eighth of wavelength, as shown

in Figure 1. “Field gradient” is widely used in selectively exciting dipolar transitions in semiconductor,<sup>158</sup> metal vapor<sup>159</sup> and neutral atoms.<sup>160,161</sup>

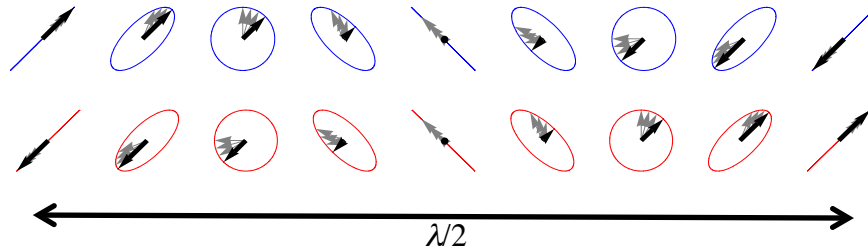


Figure 6.1 Electric and magnetic fields in the “field gradient” configuration. The fields are shown at intervals of  $\lambda/16$ . The fields lie in the plane perpendicular to the axis of propagation, but for illustration purposes each slice of the EM fields has been rotated to lie in the plane of the paper. The gray arrows represent the recent past positions of the field vectors.

A close examination of the configuration further reveals that the magnetic field component also has the alternating polarization state, which exactly opposes to the electric field polarization at every point in space (Figure 6.1). Essentially, linear polarization may be decomposed into a coherent superposition of left- and right-CPL of equal amplitude and fixed phase. The two incident beams of linear polarization should carry absolutely equal number of left- and right-circular modes everywhere in space. Therefore, both spin density and spin current for the “polarization gradient” configuration should vanish in space. Simple calculations yield a consistent result, i.e.  $s_z = \mathbf{j}_s = 0$ . In contrast,  $s_1$  in the EM configuration equals  $\frac{1}{\omega} E_0^2 \sin(2kz) \hat{\mathbf{k}}$ .

The r.h.s of equation (6.14) implies that material charge and current may act as a source or sink for photon *helicity*. The quantity  $t$  quantifies how electrically charged

bodies may apply torques on photon spins. Quantum mechanically, the torque density

$t = \frac{\partial s_z}{\partial t}$ . In the Heisenberg representation, the total torque in space is:

$T = \int t d^3r = \frac{\partial G_z}{\partial t} = \frac{[G_z, H]}{i\hbar}$ , where  $H$  is the total Hamiltonian of the system. In Fourier

space,  $H$  may be decomposed into  $H_{\text{field}}$  and  $H_{\text{source}}$ , respectively:

$$H = H_{\text{field}} + H_{\text{source}} = \sum_{\mathbf{k}} \left\{ \hbar c k (a_L^+ a_L + a_R^+ a_R) - \mathbf{j}_{\perp, L}^* \cdot \mathbf{a}_{\perp, L} - \mathbf{j}_{\perp, R}^* \cdot \mathbf{a}_{\perp, R} \right\}, \quad (6.16)$$

where  $H_{\text{source}} = -\int d^3r \mathbf{A}_{\perp} \cdot \mathbf{j}_{\perp}$ ,  $\mathbf{j}_{\perp, L}$  and  $\mathbf{j}_{\perp, R}$  are the components of transverse current density on the left- and right-circular polarization bases, respectively; and  $\mathbf{a}_{\perp, L}$ ,  $\mathbf{a}_{\perp, R}$  are the corresponding vector potentials in Fourier space. Applying equations (6.11) and (6.15) to (6.16), one has:

$$\frac{[G_z, H]}{i\hbar} = -c \sum_{\mathbf{k}} \left\{ \mathbf{j}_{\perp, L}^* \cdot \mathbf{c}_{\perp, L} + \mathbf{j}_{\perp, R}^* \cdot \mathbf{c}_{\perp, R} \right\} = -\frac{c}{2} \int d^3r \left\{ (\nabla \times \mathbf{m}_{\perp}) \cdot \mathbf{C} + (\nabla \times \mathbf{C}) \cdot \mathbf{m}_{\perp} \right\}. \quad (6.17)$$

Therefore  $t = -\frac{c}{2} \left\{ (\nabla \times \mathbf{m}_{\perp}) \cdot \mathbf{C} + (\nabla \times \mathbf{C}) \cdot \mathbf{m}_{\perp} \right\}$  represents the torque density in space

exerted by material current on photon spins. Mechanical measurement of the torque effect on photon helicity dates back to 1930s, as first reported by Beth.<sup>162, 163</sup>

We note the remarkable resemblance between optical chirality and photon spins, as reflected in equations (6.1 - 4) and equations (6.13, 14). The resemblance is less surprising if one considers the fact that circular polarizations are both chiral objects as we examine their topological properties and are eigenstates of a light field as we quantize it in the Hilbert space. Therefore, an intriguing question is: can one devise chiral structures

that may enable a spin-dependent transportation of light in some desired fashion. We are certainly equipped with both theoretical foundations (as the continuity equation (6.14) and (2.16)) and experimental methods (as the active research in making three-dimensional chiral metamaterials<sup>6</sup>) to search for an answer.

## **6.2 Innovation in imaging apparatus**

Optical imaging plays an essential role in all aspects of modern science, from sensitive fluorescence microscopy, to ultrafast spectroscopy, to astronomy. One usually hopes to extract the maximum information from the available photons: their polarization, their wavelength, and their distribution in space and time. Often there is a tradeoff between spatial and temporal resolution: wide-field cameras provide megapixel spatial information, but have slow readouts. Confocal and point-scanning techniques provide excellent dynamic information, but no spatial information. In our CD imaging experiment, the EMCCD was used with an LCVR (liquid crystal variable retarder), operating at 1 Hz. While fractional precision is above  $10^{-4}$ , the apparatus may not detect any temporal dynamics faster than 1 s.

Therefore, great interests lie in devising an imaging apparatus of both spatial and temporal resolution. One prominent progress was made in 2011, where an all-analog lock-in amplifier with a response time of  $\sim 100$  ns was integrated with a confocal stimulated Raman scattering microscopy, achieving a video-rate molecular imaging in vivo.<sup>164</sup> A new generation of cameras, developed for TOF (time-of-flight) imaging, offers an alternative with much simplified hardware.

The so-called “Scientific Lock-in Imaging Module” (SLIM) operates on a time-of-flight technology. The imaging module is to be used with a modulated light source, which may be a pulsed laser or a cw modulated by mechanical or electronic units. The imaging chip consists of 176 by 144 pixels (the exact number varies depending on the manufacturers). Each pixel contains two capacitors: one is in phase with the light source, while the other is one out of phase. During measurement, photoelectrons are generated by the incident photons from a sample (either reflected photons from the light source, or secondary photons such as fluorescence, Raman, etc). Depending on the timing of the incident photon, either the in-phase or out-of-phase capacitor is at work. By examining the number of photoelectrons in the two capacitors over the entire pixel arrays, spatial and temporal dynamics may be resolved, simultaneously.

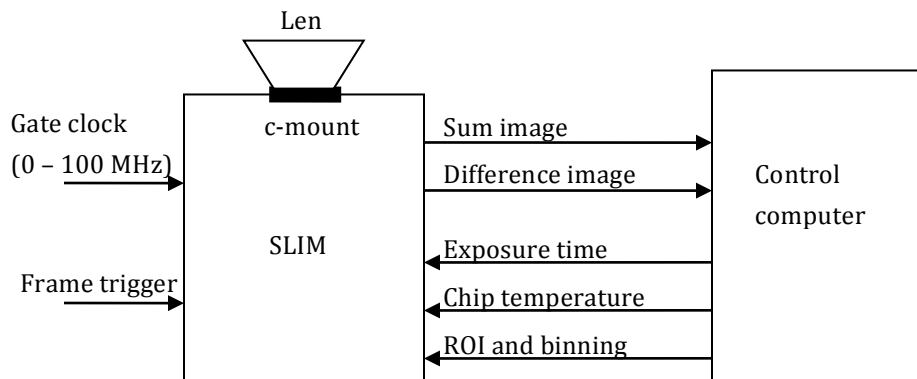


Figure 6.2 Structure of the scientific lock-in imaging module

Figure 6.2 shows the main features. The prototype was manufactured at MESA Imaging (<http://www.mesa-imaging.ch/>). The device may be operated in two modes:

the slave mode, where a light source alternates between on and off at certain frequency and the SLIM simply follows the modulation; and the master mode, where the internal digital lock in SLIM drives both the camera and a light source. For the prototype we have in the lab, both slave and master modes may operate from 100 Hz to 30 MHz. Note that the SLIM camera is still limited by a slow readout rate (which is about 250 Hz). Strength of the device is to sample tiny signal under modulation in the tens of thousands of pixels out of a big background noise. A list of useful operating frequencies may be found in table 6.1

<b>Application</b>	<b>Lock-in frequency</b>
Faraday rotation imaging	1 kHz
Polarimetry with a photoelastic modulator	50 kHz, 20 kHz
Imaging O <sub>2</sub> with a phosphorescent indicator	400 kHz
Photothermal and photoacoustic imaging	1 – 10 MHz
Nonlinear imaging with a Ti:Sapphire laser	88 MHz

Table 6.1 List of modulation frequencies that are useful in various systems

Here I am to list a few possible applications of the imaging module. We expect a wide adoption of the technology once some proof-of-principle measurements are successfully performed.

## Polarimetry

Polarization properties of materials (birefringence, Faraday rotation, and optical rotatory dispersion) often relate to fundamentally important features of the molecular and electronic compositions. For instance birefringence indicates the orientation of cytoskeletal elements in a cell, and Faraday rotation indicates regions of enhanced magnetic susceptibility. Yet these imaging modalities have remained largely inaccessible to microscopic imaging because the signals are proportional to path length in the sample; in small samples the signals are very small. Lock-in imaging techniques may allow scientists to overcome technical noise and to achieve shot noise-limited measurements by mapping the signal to a high-frequency band. Typically single-point polarimetry measurements are performed with a photoelastic modulator and lock-in detection at 50 kHz. A SLIM would enable similar measurements in a wide-field format.

We devised an apparatus using the SLIM to map the distribution of linear birefringence within a thin piece of plastic sheet. To create strain and thus crumple the molecular alignment inside the material, we stretched the piece till it broke in the center (Figure 6.3 Left). The light source was a tungsten lamp, coupled through a homemade monochromator, and only 630 nm was allowed to pass through. Subsequently, the light beam propagated through a linear polarizer at  $45^\circ$ , a PEM (PEM 100 HINDS) mounted at  $0^\circ$ , the sample, another linear polarizer at  $-45^\circ$ , and a tube lens before reaching the SLIM. The PEM operated at a retardance of  $0.383 \lambda$ , so as to eliminate any time-dependence of DC component.

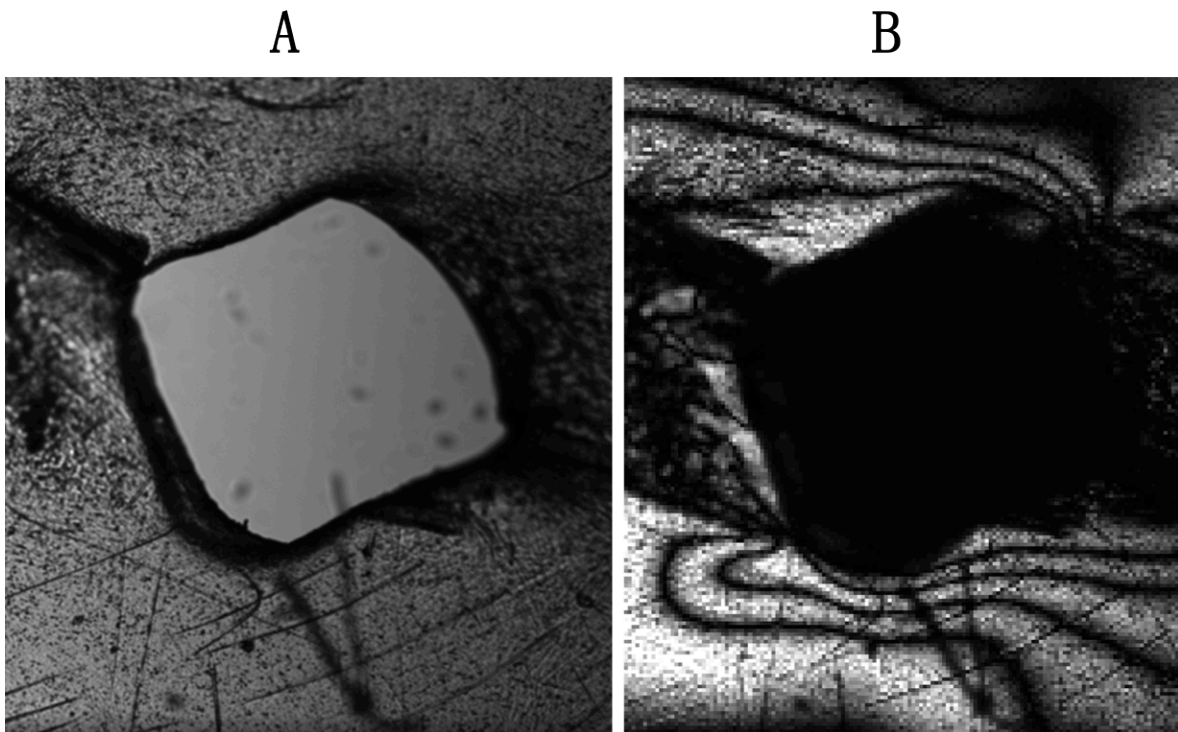


Figure 6.3 Lock-in imaging on a thin plastic sheet. (A) A sum image by SLIM after 500 frames average. The image records transmitted intensity through the sample. The square in the middle is a hole on the sample. (B) A differential image by SLIM after 500 frames average. It reports the distribution of linear birefringence within the sample.

As shown in Figure 6.3 (A), the raw image that records transmitted intensity of incident light reveals the structural information of the sample, including a hole in the center. Figure 6.3(B) is the differential image of the two read-out channels, so that only the signal modulated at the PEM frequency, 50 KHz, was recorded. Therefore, the contrast is mostly from heterogeneities in linear birefringence within the sample. The curved dark bands in the differential map, absent in raw image, are clear evidence of such heterogeneity. Next, we plan to use the SLIM to exam muscular contractions in model organisms, such as heartbeat in zebrafish.

### **Transient absorption imaging**

An intense laser pulse can briefly alter the absorption spectrum of a sample, thereby modulating the transmission of a second laser beam. Typical time scales of the modulation are 1 - 100 ns, so one would like to perform lock-in detection on the second beam in the frequency range of 10 – 100 MHz. Transient absorption imaging may enable optical imaging of absorbing samples with sensitivity comparable to that of fluorescence; yet without the challenges of photobleaching and shot noise inherent to fluorescence imaging.

### **Photothermal and photoacoustic imaging**

In these imaging techniques, a pulsed laser generates either thermal or acoustical shocks in a sample, which modulate the surrounding optical properties.<sup>165, 166</sup> These techniques allow microscopic characterization of the mechanical, thermal and optical properties of a sample, but they have only been implemented in a slow, point-scanning format. With a SLIM, one could perform wide field lock-in imaging for both of these modalities, thereby dramatically increasing the speed and decreasing the cost of such a system.

### **Time-resolved spectroscopy**

By coupling a SLIM to a spectrometer, one could convert one of the spatial axes of the imager into a spectral axis. Then one could probe time-resolved spectra in photochemical systems such as the photosynthetic reaction center,<sup>167</sup> the rhodopsin proteins responsible for vision,<sup>168</sup> and many other biological chromophores. The SLIM could become a key

component in ultrafast spectroscopy systems.

### **6.3 The CLIC geometry: beyond chirality**

As we suggested in chapter 5, the CLIC geometry is advantageous in primarily three aspects: First, it is easy to devise. Only a plano-convex lens and a flat optical surface are required to generate the tightly confined shallow wedge in between, where interesting phenomena may take place. Second, it enables a continuous sampling with incremental confinement in one dimension, at the same time allows observing a large area of interest in the other two dimensions in space. Third, the CLIC is adaptive to examine a wide variety of physical systems, owing to its structural flexibility.

Following the experiment on the “twisted H” configuration of gold nanowire arrays, it may be interesting to put chiral fluorophores in the chiral nano-junctions. We expect a large chiroptical response of the molecules in the highly contorted EM fields of subwavelength gaps. Further, we’d like to discuss some other experiments that are entailed by the unique CLIC design.

#### **Metal-insulator-metal**

A nanoscale gap between two metal surfaces may confine propagating surface plasmon polaritons (SPPs) to very small dimensions.<sup>169</sup> The so-called metal-insulator-metal (MIM) is a plasmonic slot waveguide, “squeezing” the SPPs field into the dielectric core. As a result, the wavelength along the direction of propagation is shortened. MIM-SPPs can therefore be guided in waveguides with very small transverse dimensions and allow the realization of nanocavities with extremely small mode volumes.

The CLIC device provides a convenient scheme for devising such a structure: one may deposit a thin metal film on the surface of a plano-convex lens and of an optical flat, and finely engage the two pieces until they make contact at a single point. A wide-field or confocal microscope may be deployed to watching the excitation and propagation of surface plasmons over the varying gap height. In addition, functional diversity may be achieved by preparing sophisticated patterns on the respective surface, and/or fill the gap with materials of interest (such as molecules embedded in polymer scaffold).

### **Plasmonic sensing**

Surface plasmons resonance (SPR) has long been used to enhance the sensitivity of several spectroscopic measurements including fluorescence, Raman scattering, and second harmonic generation.<sup>170</sup> A simple example, as shown in Figure 6.4, measures molecular absorption on a metal film through total internal reflection. The metal surface is coated with conjugated antigens, which covalently bind to antibodies. The adsorbing molecules modify the local index of refraction, which results in a change of the resonance conditions of the surface plasmon waves. On the detection side, either the angle or spectrum of reflected beam is analyzed.

The CLIC geometry may help further improve the detection sensitivity for at least two reasons: (1) Rather than a single metallic layer, two metal films are used in the CLIC. With the aid of EM field simulation, the system with an additional metallic structure atop may be more effective at perturbing plasmon resonance condition upon molecular absorption; (2) the physical confinement may elongate the residence time of molecules in

the system, which will likely result in an enhanced binding efficiency.

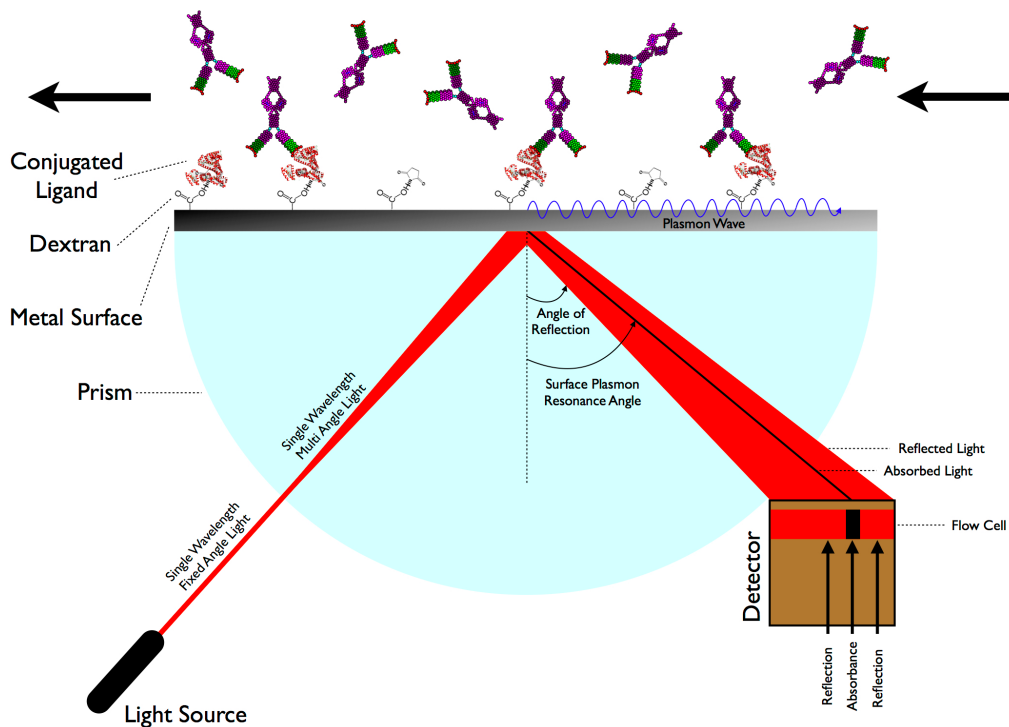


Figure 6.4 Surface plasmon resonance in the application of biosensing. The figure is adapted from wikipedia at [http://en.wikipedia.org/wiki/Surface\\_plasmon\\_resonance](http://en.wikipedia.org/wiki/Surface_plasmon_resonance)

### Assessing motion of molecules

In 2010, the CLIC device was originally devised for imaging freely diffusing molecules under confinement.<sup>12</sup> A successful deployment of CLIC achieved long observation time of molecular diffusion, improved SNR (signal-to-noise) ratio, and molecular sizing. Active research with the device has been pursued in understanding biomolecular interaction, diffusion and relaxation properties of different species.

On another front, low-field NMR is routinely used for assessing molecular diffusion and relaxation.<sup>171</sup> The conventional approach in encoding diffusion information during

NMR measurement is the so-called “pulsed field gradient” (PFG) technique. In the PFG-NMR measurement, in addition to a permanent magnet to generate  $\mathbf{B}_0$  field and a RF coil to generate  $\mathbf{B}_1$ , magnetic field gradient coils are employed to generate pulsed  $\mathbf{B}_0$  gradient in between of the RF pulse sequences. The setup is well suited to assess fluid properties, including relaxation time  $T_1$ ,  $T_2$ , diffusion coefficient ( $D$ ) and two-dimensional mapping (such as  $D$ - $T_2$  and  $T_1$ - $T_2$ ). Besides, a variety of NMR probes are under development, with a promise to go “on-chip” of the same functionality.<sup>172, 173</sup>

An interesting question is: with the physical confinement in the CLIC geometry, can one detect molecules’ structural changes (aggregation, conformational change, binding events) by NMR relaxometry and/or diffusometry that are inaccessible in bulk measurement. For example, in such a confined space, aggregation of molecules may significantly alter diffusion/relaxation properties of solvent nuclei. Such setup may be useful for biomolecular screening and medical diagnose.

### **Cavity quantum electrodynamics (QED)**

The well-defined nanoscale gap in the CLIC may be a test ground for studying QED of quantum absorbers and emitters. Indeed, previous studies exhibited both experimental and theoretical results on the change of fluorescence emission spectrum of a single molecule by squeezing it in the gap.<sup>13</sup> More work remains to be seen as how the CLIC concept may apply to build optical cavities, and what functionalities it may fulfill.<sup>174, 175</sup>

## References

1. Barron, L. D. in *Molecular light scattering and optical activity* (Cambridge University Press, 2004).
2. Jackson, J. D. in *Classical Electrodynamics* (John Wiley & Sons, Inc., 2001).
3. Berova, N., Nakanishi, K. & Woody, R. in *Circular dichroism: principles and applications* (Wiley-VCH, 2000).
4. Tang, Y. & Cohen, A. E. Optical chirality and its interaction with matter. *Phys. Rev. Lett.* **104**, 163901 (2010).
5. Tang, Y. & Cohen, A. E. Enhanced enantioselectivity in excitation of chiral molecules by superchiral light. *Science* **332**, 333-336 (2011).
6. Soukoulis, C. M. & Wegener, M. Past achievements and future challenges in the development of three-dimensional photonic metamaterials. *Nature Photonics* **5**, 523-530 (2011).
7. Yang, N. & Cohen, A. E. Local geometry of electromagnetic fields and its role in molecular multipole transitions. *The Journal of Physical Chemistry B* **115**, 5304 (2011).
8. Chandrasekhar, S., Kitzerow, H. & Bahr, C. in *Chirality in liquid crystals* (Springer, 2000).
9. Byers, J., Yee, H., Petralli-Mallow, T. & Hicks, J. Second-harmonic generation circular-dichroism spectroscopy from chiral monolayers. *Physical Review B* **49**, 14643 (1994).
10. Shapiro, M. & Brumer, P. in *Principles of the Quantum Control of Molecular Processes* (Wiley-VCH, 2003).
11. Ozbay, E. Plasmonics: merging photonics and electronics at nanoscale dimensions. *Science* **311**, 189 (2006).
12. Leslie, S. R., Fields, A. P. & Cohen, A. E. Convex lens-induced confinement for imaging single molecules. *Anal. Chem.* **82**, 6224-6229 (2010).
13. Chizhik, A. *et al.* Tuning the fluorescence emission spectra of a single molecule with a variable optical subwavelength metal microcavity. *Phys. Rev. Lett.* **102**, 73002 (2009).
14. Keller, D. & Bustamante, C. Theory of the interaction of light with large inhomogeneous molecular aggregates. II. Psi-type circular dichroism. *J. Chem. Phys.* **84**, 2972 (1986).
15. Aeschlimann, M. *et al.* Adaptive subwavelength control of nano-optical fields. *Nature* **446**, 301-304 (2007).

16. Brixner, T., García de Abajo, F., Schneider, J. & Pfeiffer, W. Nanoscopic ultrafast space-time-resolved spectroscopy. *Phys. Rev. Lett.* **95**, 93901 (2005).
17. Mukamel, S. in *Principles of nonlinear optical spectroscopy* (Oxford University Press, New York, 1995).
18. Pasteur, L. Recherches sur le dimorphisme. *Comptes Rend.Hebd.Séances Acad.Sci* **26**, 535 (1848).
19. Nelson, D. L. & Cox, M. M. in *Lehninger principles of biochemistry* (Wh Freeman, 2008).
20. Hutt, A. & Tan, S. Drug chirality and its clinical significance. *Drugs* **52**, 1 (1996).
21. Barron, L. True and false chirality and absolute asymmetric synthesis. *J. Am. Chem. Soc.* **108**, 5539-5542 (1986).
22. Avalos, M., Babiano, R., Cintas, P., Jiménez, J. L. & Palacios, J. C. Chiral autocatalysis: where stereochemistry meets the origin of life. *Chemical Communications*, 887-892 (2000).
23. MacDermott, A. *et al.* Homochirality as the signature of life: the SETH Cigar. *Planet. Space Sci.* **44**, 1441-1446 (1996).
24. Cline, D. B. in *Physical origin of homochirality in life* (Cambridge Univ Press, 1996).
25. Rikken, G. & Raupach, E. Enantioselective magneto-chiral photochemistry. *Nature* **405**, 932-935 (2000).
26. Quack, M. How important is parity violation for molecular and biomolecular chirality? *Angewandte Chemie International Edition* **41**, 4618-4630 (2002).
27. Avalos, M., Babiano, R., Cintas, P., Jiménez, J. L. & Palacios, J. C. From parity to chirality: chemical implications revisited. *Tetrahedron: Asymmetry* **11**, 2845-2874 (2000).
28. Barron, L. True and false chirality and parity violation. *Chemical physics letters* **123**, 423-427 (1986).
29. Barron, L. D. Fundamental symmetry aspects of chirality. *BioSystems* **20**, 7-14 (1987).
30. Barron, L. D. & Buckingham, A. D. Time reversal and molecular properties. *Acc. Chem. Res.* **34**, 781-789 (2001).
31. Goldstein, H., Poole, C. P. & Safko, J. in *Classical mechanics* (Addison-Wesley, 2001).

32. Whitmore, L. & Wallace, B. A. Protein secondary structure analyses from circular dichroism spectroscopy: methods and reference databases. *Biopolymers* **89**, 392-400 (2007).
33. Goto, Y., Calciano, L. J. & Fink, A. L. Acid-induced folding of proteins. *Proceedings of the National Academy of Sciences* **87**, 573-577 (1990).
34. Carvlin, M. J., Datta-Gupta, N. & Fiel, R. J. Circular dichroism spectroscopy of a cationic porphyrin bound to DNA. *Biochem. Biophys. Res. Commun.* **108**, 66-73 (1982).
35. Barron, L. D. & Buckingham, A. D. Vibrational optical activity. *Chemical Physics Letters* **492**, 199-213 (2010).
36. Barron, L. & Buckingham, A. Rayleigh and Raman optical activity. *Annu. Rev. Phys. Chem.* **26**, 381-396 (1975).
37. Rhee, H. *et al.* Femtosecond characterization of vibrational optical activity of chiral molecules. *Nature* **458**, 310-313 (2009).
38. Kuhn, W. & Braun, E. Photochemische erzeugung optisch aktiver stoffe. *Naturwissenschaften* **17**, 227-228 (1929).
39. Jorissen, A. & Cerf, C. Asymmetric photoreactions as the origin of biomolecular homochirality: a critical review. *Origins of Life and Evolution of Biospheres* **32**, 129-142 (2002).
40. Ma, Y. & Salam, A. Controlling state populations of enantiomers of real chiral molecules by using a circularly polarized pulsed laser. *Chemical physics letters* **431**, 247-252 (2006).
41. Brixner, T. *et al.* Quantum control by ultrafast polarization shaping. *Phys. Rev. Lett.* **92**, 208301 (2004).
42. Moskovits, M. Surface-enhanced spectroscopy. *Reviews of Modern Physics* **57**, 783 (1985).
43. Nitzan, A. & Brus, L. Can photochemistry be enhanced on rough surfaces? *J. Chem. Phys.* **74**, 5321-5322 (1981).
44. Liebermann, T. & Knoll, W. Surface-plasmon field-enhanced fluorescence spectroscopy. *Colloids Surf. Physicochem. Eng. Aspects* **171**, 115-130 (2000).
45. Haynes, C. L. & Van Duyne, R. P. Plasmon-sampled surface-enhanced Raman excitation spectroscopy. *The Journal of Physical Chemistry B* **107**, 7426-7433 (2003).
46. Lesage, A. *et al.* Surface enhanced NMR spectroscopy by dynamic nuclear polarization. *J. Am. Chem. Soc.* **132**, 15459 (2010).

47. Sundaramurthy, A. *et al.* Toward nanometer-scale optical photolithography: utilizing the near-field of bowtie optical nanoantennas. *Nano letters* **6**, 355-360 (2006).
48. Sánchez, E. J., Novotny, L. & Xie, X. S. Near-field fluorescence microscopy based on two-photon excitation with metal tips. *Phys. Rev. Lett.* **82**, 4014-4017 (1999).
49. Shemer, G. *et al.* Chirality of silver nanoparticles synthesized on DNA. *J. Am. Chem. Soc.* **128**, 11006-11007 (2006).
50. Shemer, G. & Markovich, G. Enhancement of magneto-optical effects in magnetite nanocrystals near gold surfaces. *The Journal of Physical Chemistry B* **106**, 9195-9197 (2002).
51. Hui, P. & Stroud, D. Theory of Faraday rotation by dilute suspensions of small particles. *Appl. Phys. Lett.* **50**, 950-952 (1987).
52. Jain, P. K., Xiao, Y., Walsworth, R. & Cohen, A. E. Surface plasmon resonance enhanced magneto-optics (SuPREMO): Faraday rotation enhancement in gold-coated iron oxide nanocrystals. *Nano letters* **9**, 1644-1650 (2009).
53. Ctistis, G. *et al.* Optical and magnetic properties of hexagonal arrays of subwavelength holes in optically thin cobalt films. *Nano Letters* **9**, 1-6 (2008).
54. Stiles, P. L., Dieringer, J. A., Shah, N. C. & Van Duyne, R. P. Surface-enhanced Raman spectroscopy. *Annu.Rev.Anal.Chem.* **1**, 601-626 (2008).
55. Nie, S. & Emory, S. R. Probing single molecules and single nanoparticles by surface-enhanced Raman scattering. *Science* **275**, 1102-1106 (1997).
56. Schatz, G. C. Theoretical studies of surface enhanced Raman scattering. *Acc. Chem. Res.* **17**, 370-376 (1984).
57. Sass, J., Neff, H., Moskovits, M. & Holloway, S. Electric field gradient effects on the spectroscopy of adsorbed molecules. *J. Phys. Chem.* **85**, 621-623 (1981).
58. Ayars, E., Hallen, H. & Jahncke, C. Electric field gradient effects in Raman spectroscopy. *Phys. Rev. Lett.* **85**, 4180-4183 (2000).
59. Efrima, S. The effect of large electric field gradients on the Raman optical activity of molecules adsorbed on metal surfaces. *Chemical physics letters* **102**, 79-82 (1983).
60. Janesko, B. G. & Scuseria, G. E. Surface enhanced Raman optical activity of molecules on orientationally averaged substrates: Theory of electromagnetic effects. *J. Chem. Phys.* **125**, 124704 (2006).

61. Abdali, S. & Blanch, E. W. Surface enhanced Raman optical activity (SEROA). *Chem. Soc. Rev.* **37**, 980-992 (2008).
62. Kunz, R. & Lukosz, W. Changes in fluorescence lifetimes induced by variable optical environments. *Physical Review B* **21**, 4814 (1980).
63. Steiner, M. *et al.* Microcavity-Controlled Single-Molecule Fluorescence. *ChemPhysChem* **6**, 2190-2196 (2005).
64. Gerton, J. M., Wade, L. A., Lessard, G. A., Ma, Z. & Quake, S. R. Tip-enhanced fluorescence microscopy at 10 nanometer resolution. *Phys. Rev. Lett.* **93**, 180801 (2004).
65. Kühn, S., Håkanson, U., Rogobete, L. & Sandoghdar, V. Enhancement of single-molecule fluorescence using a gold nanoparticle as an optical nanoantenna. *Phys. Rev. Lett.* **97**, 17402 (2006).
66. Taminiau, T., Stefani, F., Segerink, F. & Van Hulst, N. Optical antennas direct single-molecule emission. *Nature Photonics* **2**, 234-237 (2008).
67. Novotny, L. & Hecht, B. in *Principles of nano-optics* (Cambridge university press, 2006).
68. Barnes, W. L., Dereux, A. & Ebbesen, T. W. Surface plasmon subwavelength optics. *Nature* **424**, 824-830 (2003).
69. Kiraz, A., Kurt, A., Dundar, M. & Demirel, A. Simple largely tunable optical microcavity. *Appl. Phys. Lett.* **89**, 081118-081118-3 (2006).
70. Sanders, J. Microstructure and crystallinity of gem opals. *Am. Mineral.* **60**, 749-757 (1975).
71. Gralak, B., Tayeb, G. & Enoch, S. Morpho butterflies wings color modeled with lamellar grating theory. *Optics express* **9**, 567-578 (2001).
72. Wilson, S. & Hutley, M. The optical properties of 'moth eye' antireflection surfaces. *Journal of Modern Optics* **29**, 993-1009 (1982).
73. Roberts, N., Chiou, T. H., Marshall, N. & Cronin, T. A biological quarter-wave retarder with excellent achromaticity in the visible wavelength region. *Nature Photonics* **3**, 641-644 (2009).
74. Sharma, V., Crne, M., Park, J. O. & Srinivasarao, M. Structural origin of circularly polarized iridescence in jeweled beetles. *Science* **325**, 449-451 (2009).
75. Barber, D. & Freestone, I. An investigation of the origin of the colour of the Lycurgus Cup by analytical transmission electron microscopy. *Archaeometry* **32**, 33-45 (1990).

76. Smith, D., Pendry, J. & Wiltshire, M. Metamaterials and negative refractive index. *Science* **305**, 788-792 (2004).
77. Pendry, J. B., Holden, A., Robbins, D. & Stewart, W. Magnetism from conductors and enhanced nonlinear phenomena. *Microwave Theory and Techniques, IEEE Transactions on* **47**, 2075-2084 (1999).
78. Veselago, V. Electrodynamics of materials both permittivity and permeability being negative. *Uspekhi Fizicheskikh Nauk (in Russian)* **92**, 517-526 (1967).
79. Smith, D. R., Padilla, W. J., Vier, D., Nemat-Nasser, S. C. & Schultz, S. Composite medium with simultaneously negative permeability and permittivity. *Phys. Rev. Lett.* **84**, 4184-4187 (2000).
80. Pendry, J. B. Negative refraction makes a perfect lens. *Phys. Rev. Lett.* **85**, 3966-3969 (2000).
81. Pendry, J. B., Schurig, D. & Smith, D. R. Controlling electromagnetic fields. *Science* **312**, 1780-1782 (2006).
82. Schurig, D. *et al.* Metamaterial electromagnetic cloak at microwave frequencies. *Science* **314**, 977-980 (2006).
83. Liu, N. *et al.* Three-dimensional photonic metamaterials at optical frequencies. *Nature materials* **7**, 31-37 (2007).
84. Liu, N., Fu, L., Kaiser, S., Schweizer, H. & Giessen, H. Plasmonic Building Blocks for Magnetic Molecules in Three-Dimensional Optical Metamaterials. *Adv Mater* **20**, 3859-3865 (2008).
85. Gansel, J. K. *et al.* Gold helix photonic metamaterial as broadband circular polarizer. *Science* **325**, 1513-1515 (2009).
86. Deubel, M. *et al.* Direct laser writing of three-dimensional photonic-crystal templates for telecommunications. *Nature materials* **3**, 444-447 (2004).
87. Pendry, J. B. A chiral route to negative refraction. *Science* **306**, 1353-1355 (2004).
88. Hendry, E. *et al.* Ultrasensitive detection and characterization of biomolecules using superchiral fields. *Nature nanotechnology* **5**, 783-787 (2010).
89. Decker, M. *et al.* Strong optical activity from twisted-cross photonic metamaterials. *Opt. Lett.* **34**, 2501-2503 (2009).
90. Decker, M., Zhao, R., Soukoulis, C., Linden, S. & Wegener, M. Twisted split-ring-resonator photonic metamaterial with huge optical activity. *Opt. Lett.* **35**, 1593-1595 (2010).

91. Zhou, J. *et al.* Chiral THz metamaterial with tunable optical activity (2010).
92. Zhang, S. *et al.* Negative refractive index in chiral metamaterials. *Phys. Rev. Lett.* **102**, 23901 (2009).
93. Woltjer, L. A theorem on force-free magnetic fields. *Proc. Natl. Acad. Sci. U. S. A.* **44**, 489 (1958).
94. Subramanian, K. & Brandenburg, A. Magnetic helicity density and its flux in weakly inhomogeneous turbulence. *The Astrophysical Journal Letters* **648**, L71 (2008).
95. Moffatt, H. K. The degree of knottedness of tangled vortex lines. *J. Fluid Mech.* **35**, 117-129 (1969).
96. Harris, A., Kamien, R. D. & Lubensky, T. Molecular chirality and chiral parameters. *Reviews of Modern Physics* **71**, 1745 (1999).
97. Zee, A. in *Quantum field theory in a nutshell* (Princeton University Press, 2010).
98. Lipkin, D. M. Existence of a new conservation law in electromagnetic theory. *Journal of Mathematical Physics* **5**, 696 (1964).
99. Kibble, T. Conservation laws for free fields. *Journal of Mathematical Physics* **6**, 1022 (1965).
100. Candlin, D. Analysis of the new conservation law in electromagnetic theory. *Il Nuovo Cimento (1955-1965)* **37**, 1390-1395 (1965).
101. Ranada, A. On the magnetic helicity. *European journal of physics* **13**, 70 (2000).
102. Trueba, J. L. & Ranada, A. F. The electromagnetic helicity. *European Journal of Physics* **17**, 141 (1999).
103. BARRON, L. Parity and Optical Activity. *Nature* **238**, 17 (1972).
104. Isborn, C., Claborn, K. & Kahr, B. The optical rotatory power of water. *The Journal of Physical Chemistry A* **111**, 7800-7804 (2007).
105. Buckingham, A., Raab, R., Buckingham, A. & Raab, R. Electric-field-induced differential scattering of right and left circularly polarized light. *Proceedings of the Royal Society of London. A. Mathematical and Physical Sciences* **345**, 365-377 (1975).
106. Craig, D. P. & Thirunamachandran, T. in *Molecular quantum electrodynamics* (Dover Publications, 1998).

107. Poynting, J. H. On the transfer of energy in the electromagnetic field. *Philosophical Transactions of the Royal Society of London* **175**, 343-361 (1884).
108. Noether, E. Invariante variationsprobleme. *Gött.Nachr* **235** (1918).
109. Przanowski, M., Rajca, B. & Tosiek, J. On Some Conservation Laws in the Maxwell Electrodynamics in Vacuum. *Acta Physica Polonica B* **25**, 1065 (1994).
110. Fushchich, W. I. & Nikitin, A. G. in *Symmetries of Maxwell's equations* (Springer, 1987).
111. Cohen-Tannoudji, C., Dupont-Roc, J. & Grynberg, G. in *Photons and Atoms-Introduction to Quantum Electrodynamics* (Wiley-VCH, 1997).
112. Berestetskii, V. B., Pitaevskii, L. & Lifshitz, E. M. in *Quantum electrodynamics* (Butterworth-Heinemann, 1982).
113. Harris, A., Kamien, R. D. & Lubensky, T. Microscopic origin of cholesteric pitch. *Phys. Rev. Lett.* **78**, 1476-1479 (1997).
114. Anco, S. C. & Pohjanpelto, J. Classification of local conservation laws of Maxwell's equations. *Acta Applicandae Mathematicae* **69**, 285-327 (2001).
115. Fischer, P. & Hache, F. Nonlinear optical spectroscopy of chiral molecules. *Chirality* **17**, 421-437 (2005).
116. Kuhn, W. Quantitative Verhältnisse und Beziehungen bei der natürlichen optischen Aktivität. *Z. Phys. Chem. B* **4**, 14-36 (1929).
117. Condon, E. Theories of optical rotatory power. *Rev. Mod. Phys.* **9**, 432-457 (1937).
118. Tinoco Jr, I., Mickols, W., Maestre, M. & Bustamante, C. Absorption, scattering, and imaging of biomolecular structures with polarized light. *Annu. Rev. Biophys. Biophys. Chem.* **16**, 319-349 (1987).
119. Tang, Y. & Cohen, A. E. Optical Chirality and Its Interaction with Matter. *Phys. Rev. Lett.* **104**, 163901 (2010).
120. Turner, D. H., Tinoco Jr, I. & Maestre, M. Fluorescence detected circular dichroism. *J. Am. Chem. Soc.* **96**, 4340-4342 (1974).
121. Hassey, R., Swain, E. J., Haer, N. I., Venkataraman, D. & Barnes, M. D. Probing the chiroptical response of a single molecule. *Science* **314**, 1437 (2006).

122. Tang, Y., Cook, T. A. & Cohen, A. E. Limits on fluorescence detected circular dichroism of single helicene molecules. *The Journal of Physical Chemistry A* **113**, 6213-6216 (2009).
123. Tanaka, K., Pescitelli, G., Nakanishi, K. & Berova, N. Fluorescence detected exciton coupled circular dichroism: development of new fluorescent reporter groups for structural studies. *Monatshefte für Chemie/Chemical Monthly* **136**, 367-395 (2005).
124. Montalbetti, C. A. G. N. & Falque, V. Amide bond formation and peptide coupling. *Tetrahedron* **61**, 10827-10852 (2005).
125. Field, J. E., Hill, T. J. & Venkataraman, D. Bridged triarylaminos: a new class of heterohelicenes. *J. Org. Chem.* **68**, 6071-6078 (2003).
126. Langhals, H. & Gold, J. Chiral Bifluorophoric Perylene Dyes with Unusually High CD Effects—a Simple Model for the Photosynthesis Reaction Center. *Liebigs Annalen* **1997**, 1151-1153 (1997).
127. Moerner, W. & Kador, L. Optical detection and spectroscopy of single molecules in a solid. *Phys. Rev. Lett.* **62**, 2535-2538 (1989).
128. Bauer, M. & Kador, L. Electric-field effects of two-level systems observed with single-molecule spectroscopy. *J. Chem. Phys.* **118**, 9069 (2003).
129. Dickson, R. M., Cubitt, A. B., Tsien, R. Y. & Moerner, W. On/off blinking and switching behaviour of single molecules of green fluorescent protein. *Nature* **388**, 355-358 (1997).
130. Le Floc'H, V., Brasselet, S., Roch, J. F. & Zyss, J. Monitoring of orientation in molecular ensembles by polarization sensitive nonlinear microscopy. *The Journal of Physical Chemistry B* **107**, 12403-12410 (2003).
131. Tinoco Jr, I., Ehrenberg, B. & Steinberg, I. Fluorescence detected circular dichroism and circular polarization of luminescence in rigid media: Direction dependent optical activity obtained by photoselection. *J. Chem. Phys.* **66**, 916 (1977).
132. Hassey, R. *et al.* Single-molecule chiroptical spectroscopy: Fluorescence excitation of individual helicene molecules in polymer-supported thin-films. *Chirality* **20**, 1039-1046 (2008).
133. Lakowicz, J. R. & Masters, B. R. Principles of fluorescence spectroscopy. *J. Biomed. Opt.* **13**, 029901 (2008).
134. Claborn, K., Puklin-Faucher, E., Kurimoto, M., Kaminsky, W. & Kahr, B. Circular dichroism imaging microscopy: application to enantiomorphous twinning in biaxial crystals of 1, 8-dihydroxyanthraquinone. *J. Am. Chem. Soc.* **125**, 14825-14831 (2003).

135. Schellman, J. & Jensen, H. P. Optical spectroscopy of oriented molecules. *Chem. Rev.* **87**, 1359-1399 (1987).
136. Lambacher, A. & Fromherz, P. Fluorescence interference-contrast microscopy on oxidized silicon using a monomolecular dye layer. *Appl. Phys. A* **63**, 207-216 (1996).
137. Lambacher, A. & Fromherz, P. Luminescence of dye molecules on oxidized silicon and fluorescence interference contrast microscopy of biomembranes. *JOSA B* **19**, 1435-1453 (2002).
138. Ajo-Franklin, C. M., Yoshina-Ishii, C. & Boxer, S. G. Probing the structure of supported membranes and tethered oligonucleotides by fluorescence interference contrast microscopy. *Langmuir* **21**, 4976-4983 (2005).
139. Bernard, A., Renault, J. P., Michel, B., Bosshard, H. R. & Delamarche, E. Microcontact printing of proteins. *Adv Mater* **12**, 1067-1070 (2000).
140. Maoz, B. M. *et al.* Plasmonic chiroptical response of silver nanoparticles interacting with chiral supra-molecular assemblies. *J. Am. Chem. Soc.* (2012).
141. Slocik, J. M., Govorov, A. O. & Naik, R. R. Plasmonic circular dichroism of peptide-functionalized gold nanoparticles. *Nano letters* **11**, 701-705 (2011).
142. Hentschel, M. *et al.* *Three-Dimensional Chiral Plasmonic Oligomers* (Quantum Electronics and Laser Science Conference, Optical Society of America, 2012).
143. Abdulrahman, N. A. *et al.* Induced Chirality through Electromagnetic Coupling between Chiral Molecular Layers and Plasmonic Nanostructures. *Nano letters* **12**, 977-983 (2012).
144. Papakostas, A. *et al.* Optical manifestations of planar chirality. *Phys. Rev. Lett.* **90**, 107404 (2003).
145. Schwanecke, A. *et al.* Broken time reversal of light interaction with planar chiral nanostructures. *Phys. Rev. Lett.* **91**, 247404 (2003).
146. Hosten, O. & Kwiat, P. Observation of the spin Hall effect of light via weak measurements. *Science* **319**, 787-790 (2008).
147. Onoda, M., Murakami, S. & Nagaosa, N. Hall effect of light. *Phys. Rev. Lett.* **93**, 83901 (2004).
148. Shi, J., Zhang, P., Xiao, D. & Niu, Q. Proper definition of spin current in spin-orbit coupled systems. *Phys. Rev. Lett.* **96**, 76604 (2006).
149. Vernes, A., Gyorffy, B. & Weinberger, P. Relativistic treatment of spin-currents and spin-transfer torque. *arXiv preprint cond-mat/0609376* (2006).

150. Allen, L., Beijersbergen, M., Spreeuw, R. & Woerdman, J. Orbital angular momentum of light and the transformation of Laguerre-Gaussian laser modes. *Physical Review A* **45**, 8185-8189 (1992).
151. Simmons, J. W. & Guttman, M. J. in *States, waves, and photons: A modern introduction to light* (Addison-Wesley, 1970).
152. Van Enk, S. & Nienhuis, G. Spin and orbital angular momentum of photons. *Europhysics Letters* **25**, 497 (2007).
153. Lenstra, D. & Mandel, L. Angular momentum of the quantized electromagnetic field with periodic boundary conditions. *Physical Review A* **26**, 3428 (1982).
154. Haefner, D., Sukhov, S. & Dogariu, A. Spin hall effect of light in spherical geometry. *Phys. Rev. Lett.* **102**, 123903 (2009).
155. Albaladejo, S., Marqués, M. I., Laroche, M. & Sáenz, J. J. Scattering forces from the curl of the spin angular momentum of a light field. *Phys. Rev. Lett.* **102**, 113602 (2009).
156. Van Enk, S. & Nienhuis, G. Commutation rules and eigenvalues of spin and orbital angular momentum of radiation fields. *Journal of Modern Optics* **41**, 963-977 (1994).
157. Cameron, R. P., Barnett, S. M. & Yao, A. M. Optical helicity, optical spin and related quantities in electromagnetic theory. *New Journal of Physics* **14**, 053050 (2012).
158. Koralek, J. D. *et al.* Emergence of the persistent spin helix in semiconductor quantum wells. *Nature* **458**, 610-613 (2009).
159. Rose, T. S., Wilson, W. L., Wäckerle, G. & Fayer, M. Gas phase dynamics and spectroscopy probed with picosecond transient grating experiments. *J. Chem. Phys.* **86**, 5370-5391 (1987).
160. Dalibard, J. & Cohen-Tannoudji, C. Laser cooling below the Doppler limit by polarization gradients: simple theoretical models. *Journal of the Optical Society of America B* **6**, 2023-2045 (1989).
161. Cameron, A., Riblet, P. & Miller, A. Spin gratings and the measurement of electron drift mobility in multiple quantum well semiconductors. *Phys. Rev. Lett.* **76**, 4793-4796 (1996).
162. Beth, R. A. Mechanical detection and measurement of the angular momentum of light. *Physical Review* **50**, 115 (1936).
163. Friese, M., Enger, J., Rubinsztein-Dunlop, H. & Heckenberg, N. R. Optical angular-momentum transfer to trapped absorbing particles. *Physical Review A* **54**, 1593 (1996).

164. Saar, B. G. *et al.* Video-rate molecular imaging in vivo with stimulated Raman scattering. *Science* **330**, 1368-1370 (2010).
165. Hoelen, C., De Mul, F., Pongers, R. & Dekker, A. Three-dimensional photoacoustic imaging of blood vessels in tissue. *Opt. Lett.* **23**, 648-650 (1998).
166. Gaiduk, A., Yorulmaz, M., Ruijgrok, P. & Orrit, M. Room-temperature detection of a single molecule's absorption by photothermal contrast. *Science* **330**, 353-356 (2010).
167. Lee, H., Cheng, Y. C. & Fleming, G. R. Coherence dynamics in photosynthesis: protein protection of excitonic coherence. *Science* **316**, 1462-1465 (2007).
168. Kralj, J. M., Douglass, A. D., Hochbaum, D. R., Maclaurin, D. & Cohen, A. E. Optical recording of action potentials in mammalian neurons using a microbial rhodopsin. *Nature Methods* (2011).
169. Verhagen, E., Dionne, J. A., Kuipers, L., Atwater, H. A. & Polman, A. Near-Field Visualization of Strongly Confined Surface Plasmon Polaritons in Metal– Insulator– Metal Waveguides. *Nano letters* **8**, 2925-2929 (2008).
170. Fagerstam, L. G., Frostell-Karlsson, A., Karlsson, R., Persson, B. & Ronnberg, I. Biospecific interaction analysis using surface plasmon resonance detection applied to kinetic, binding site and concentration analysis. *J. Chromatogr.* **597**, 397-410 (1992).
171. Price, W. S. Pulsed-field gradient nuclear magnetic resonance as a tool for studying translational diffusion: Part 1. Basic theory. *Concepts Magn. Reson.* **9**, 299-336 (1997).
172. Canet, D. *et al.* Self-diffusion measurements using a radiofrequency field gradient. *Journal of Magnetic Resonance (1969)* **81**, 1-12 (1989).
173. Woelk, K., Gerald, R., Klingler, R. J. & Rathke, J. W. Imaging diffusion in toroid cavity probes. *J. Magn. Resonance* **121** (1996).
174. Vahala, K. J. Optical microcavities. *Nature* **424**, 839-846 (2003).
175. Mabuchi, H. & Doherty, A. Cavity quantum electrodynamics: Coherence in context. *Science* **298**, 1372-1377 (2002)